TRANSITION STATE WAVE PACKET STUDY OF QUANTUM MOLECULAR DYNAMICS IN COMPLEX SYSTEMS

ZHANG LILING

(B.Sc.)

A THESIS SUBMITTED

FOR THE DEGREE OF DOCTOR OF PHILOSOPHY

DEPARTMENT OF CHEMISTRY

NATIONAL UNIVERSITY OF SINGAPORE

2007

Acknowledgements

My foremost and sincerest thanks goes to my supervisors Dr. Zhang Donghui and Prof. Lee Soo Ying. Without them, this dissertation would not have been possible. I thank them for their guidance, assistance and encouragement throughout this entire work.

I also thank our group members: Yang Minghui, Lu Yunpeng, Sun Zhigang, and Lin Xin, who helped me in various aspects of my research and life. I enjoyed all the vivid discussions we had and had lots of fun being a member of this group.

I thank all the friends in our computational science department: Yang Li, Yanzhi, Fooying, Luo Jie, Zeng Lan, Baosheng, Sun Jie, Li Hu, Jiang Li, Honghuang, and others. I have ever enjoyed a happy and harmonic life with them. Now everyone is starting his own new trip and I wish them all doing well in the future.

Last but not least, I thank my family for always being there when I needed them most, and for supporting me through all these years.

Contents

Summary

In this work, the transition state time-dependent wave packet (TSWP) calculations have been carried out to study two prototype reactions with some degrees of freedom reduced. The first one is the unimolecular dissociation of formaldehyde (H_2CO) on a global fitted potential energy surface for S_0 ground state and with the nonreacting CO bond fixed at its value for global minimum. The total cumulative reaction probabilities $N(E)$s ($J = 0$) were calculated on two dividing surfaces (S_2 and S_3) respectively located at the asymptotic regions to molecular and radical products, and the product state distributions for v_{H_2}, j_{H_2}, j_{CO}, and translation energy, were obtained for several total energies. This calculation shows that as total energy much lower than 4.56eV, formaldehyde dissociates only through the molecular channel to produce modest vibrational H_2 and hot rotational CO, while as total energy increases to 4.56eV, an energy just near to the threshold to radical channel of 4.57eV, an intramolcular hydrogen abstraction pathway opens up to produce highly vibrational H_2 and cold rotational CO. These results show good agreement with quasiclassical trajectory calculations and experiments.

The second reaction studied is the H+CH_4 to H_2+CH_3 reaction on the JG-PES with seven and eight degrees of freedom included by restricting the CH_3 group under C_{3V} symmetry. In the seven dimensional calculations, the CH bond length in the CH_3 group is fixed at its equilibrium value of 2.067a.u. The cumulative reaction probabilities $N(E)$ (J=0) were calculated for the ground state and some vibrationally excited transition states on the first dividing surface across the saddle point and then the rate constants were calculated for temperature values between 200 and 500 K employing the J-shifting approximation. The 7D and 8D results agree perfect with each other, suggesting the additional mode for the symmetry stretching in CH_3 group does not

cause some dynamics change within the temperature range considered here. The results show quite good agreement with the previous 7D initial state selected wave packet (ISSWP) rates and the 5D semirigid vibrating rotor target (SVRT) rates, but much smaller than the full-dimensional multi-configuration time-dependent Hartree (MCTDH) results by one to two orders of magnitude.

The second part of this work is test calculations with continuous-configuration time-dependent self-consistent field (CC-TDSCF) approach to study the flux-flux autocorrelation functions or thermal rate constants of three complex systems: $H+CH_4$, hydrogen diffusion on Cu(100) surface, and the double well coupled to a dissipative bath. The exact quantum dynamics calculations with TSWP approach were also included for comparison. All these calculations revealed that the CC-TDSCF method is a very powerful approximation quantum dynamics method. It allows us to partition a big problem into several smaller ones. Since the correlations between bath modes in different clusters are neglected, one can systematically improve accuracy of the result by grouping modes with strong correlations together as a cluster. And due to the reduced size of basis functions in CC-TDSCF, one can always keep the number of dimensions within the computational power one has available if choosing the system and bath clusters carefully.

List of Tables

List of Figures

Chapter 1

General Introduction

The past several decades have witnessed an explosion in the development of theoretical schemes for simulating the dynamics of complex molecular systems. Motivated by major advances in time-resolved spectroscopic techniques and catalyzed by the availability of powerful computational resources, numerical simulations allowed a glimpse into the course of fundamental chemical processes and the microscopic changes that accompany the transformation of reactants to products[3].

The most useful and widespread of these schemes is the molecular dynamics (MD) method, which integrates the classical equations of motion. Because of its simplicity, MD is routinely applicable to systems of thousands of atoms. In addition, interpretation of the MD output is straightforward and allows direct visualization of a process. The major shortcoming of the MD approach is its complete neglect of quantum mechanical effects, which are ubiquitous in chemistry: The majority of chemical or biological processes of interest involve the transfer of at least one proton, which exhibits large tunneling or nonadiabatic effects; zero-point motion constrains the energy available in a chemical bond to be smaller than that predicted by the potential depth, and thus, MD calculations often result in spurious dissociation events.

Semiclassical (SC) dynamics method is thus developed to use SC theory to add quantum effects to classical MD simulations. From the early SC work in the 1960s and 1970s it seems clear that the SC approximation would provide a usefully accurate description of quantum effects in molecular dynamics. However, its practical applicability was ever limited to small molecules or models in reduced dimensionality. Recently, the initial value representation (IVR) of SC theory has reemerged in this regard as the most promising way to accomplish this; it reduces the SC

calculation to a phase space average over the initial conditions of classical trajectories, as is also required in a purely classical MD simulation. Numerous applications in recent years have established that the SC-IVR approach does indeed provide a very useful description of quantum effects in molecular systems with many degrees of freedom. However, these calculations are more difficult to carry out than ordinary classical MD simulations, so that work is continuing to find more efficient ways to implement the SC-IVR[4].

Since molecules and atoms are quantum mechanical systems, the most accurate technique to approach molecular dynamics is undoubtedly to solve the equations of motion from the first principle directly. The traditional development of quantum dynamics adopted a time-independent (TI) framework. The TI approach is usually formulated as a coupled-channel (CC) scheme in which the scattering matrix $\mathbf{S}$ is obtained at a single energy but for all energetically open transitions. An alternative way is to directly solve time-dependent (TD) Schrödinger equation by propagating a wave packet in the time domain.

There are various advantages and disadvantages associated with the TD and TI methods. The TI method is much more efficient in the dynamics involving long-lived resonances, and has no more difficulty in calculations at very low collision energies. However, the computational time of the standard TI CC approach scales as N^3 with the number of basis functions N. Although it is possible in many cases to employ iterative methods in the TI approach that could lower the scaling to N^2 provided that one can obtain converged results with a relatively small number of iteration steps. But the convergence property of iterative methods is highly dependent on the specific problem on hand. Meanwhile, many of the complex problems are not easily susceptible to standard TI treatments. For example, some processes involve very complicated boundary conditions and/or involve time-dependent (TD) Hamiltonians such as those in molecule-surface reaction, breakup process, molecular in pulsed laser fields, etc. These processes either do not have well-defined boundary conditions in the traditional sense or are inherently time-dependent and thus could not be easily treated by standard TI methods. On the other hand, TD methods provide a wonderful alternative to treat these complex processes and provide clear and direct physical insights into the dynamics in much the same way as classical mechanics[5].

The successful development and application of various computational schemes in the past two decades, coupled with the development of fast digital computers, has significantly improved the numerical efficiency for practical applications of the TD methods to chemical dynamics problems. In particular, the relatively lower computational scaling of the TD approach with the number of the basis functions (cpu time $\propto N^{\alpha}$ with $1 < \alpha < 2$) makes it computationally attractive for

large scale computations. Starting from the full-dimensional wave packet calculations of the total reaction probabilities for the benchmark reaction H_2 + OH with total angular momentum $J = 0$, TD approach is now capable of providing fully converged integral cross-section for diatom-diatom reactions, total reaction probabilities for the abstraction process in atom-triatom reactions for $J = 0$, state-to-state reaction probabilities for total angular momentum $J = 0$ and state-to-state integral cross-sections, as well as accurate cumulative reaction probabilities and thermal rate constants.

As known, the calculation of thermal rate constants of chemical reactions is an important goal in dynamics studies. Generally reaction rate constants can be calculated exactly with these two above quantum methods: TI and TD approaches. One can calculate rate constants from thermal averages of exact quantum state-to-state reaction probabilities, i.e. from the **S**-matrices obtained from full solutions to the Schrödinger equation at each energy. For reactions with barriers and with relatively sparse reactant and product quantum states, the full **S**-matrix can be calculated. Alternatively the TD Schrödinger equation can be solved for each initial state to obtain the reaction probability as a function of energy from that state. However, for reactions with a relatively dense distribution of reactant and product states at the energies of interest, the number of energetically open states contributing to the rate constant will be very large. In these cases, the full **S**-matrices or even the initial state selected reaction probabilities may be very difficult to calculate. In addition, the full **S**-matrices contain much information on state-to-state probabilities that is averaged to obtain the rate constant and thus this is in a sense wasteful if one seeks only the rate constants itself.

Some time ago Miller and co-workers[6, 7] gave direct quantum mechanical operator representations of quantities related to reactive scattering, such as the cumulative reaction probability, $N(E)$, flux-flux correlation function, C_{ff}, and the transition state reaction probability operator, which could give the thermal rate constant, $k(T)$. In these formulations dividing surface(s) between reactants and products can be defined as in transition state theory (TST). However, the rate constants and reaction probabilities *etc.* are given as traces of quantum mechanical (flux) operators. Since significant progress has been made in time-dependent wave packet (TDWP) techniques, and it is essentially not applicable to employ the initial state selected wave packet approach to calculate the cumulative reaction probability $N(E)$ due to huge number of wave packets for all the asymptotic open channels, a TDWP based approach, i.e., the transition state wave packet approach(TSWP), was explored to the determination of $N(E)$, or the reaction probabilities from (or to) specific reactant (or product) internal states, or rate constants. Noted that

in the formulation of a variety of reaction operators the two flux operators may be placed at arbitrary and different surfaces dividing reactants and products. In TSWP, wave packets starting at one surface are propagated in time until the flux across both the surfaces disappears. The coordinate range is limited by absorbing potentials placed beyond the flux surfaces toward reactants and products. The energy dependence of the desired quantities is obtained by Fourier transform of the time evolution of the flux.

The TSWP approach is very flexible and offers several advantages. First the starting flux surface may be located to minimize the number of wave packet propagations required to converge the results in a desired energy range. This will often be the TS surface for reactions with a barrier, but may be toward the reactant channel for exothermic reactions with loose transition states, etc. Second, the location of the second flux surface will depend on the information desired. If only $N(E)$ is required, the two surfaces will normally be chosen to be the same. If a 'state' cumulative reaction probability is required, for reaction from a given state or for reaction to a give state, then one flux surface must be located toward the appropriate asymptotic region where a projection of the flux on to the internal states is possible. In all cases only one propagation per initial wave packet is required for information at all energies. This TSWP approach has been successfully applied to calculate $N(E)$ for the prototype triatom H+H_2 reaction, four atom reaction H_2+OH→H_2O+H, etc[8, 9, 10].

In this project, we applied the TSWP approach to study two reaction systems. The first chemical reaction is the photodissociation of formaldehyde (H_2CO). It is large enough to have interestingly complex photochemistry; a detailed understanding of this molecule could prove useful as a prototype for the photochemistry of small polyatomics. It is small enough for *ab initio* calculations and can serve as a testing ground for theoretical investigations. Therefore it could present a meeting point for theory and experiment. However there are four different dissociation pathways on the ground state (S_0), which make the dissociation mechanism complicate. A significant experiment by Moore and coworkers[11] reported that there are two different kinds of product state distributions on the channel to H_2+CO when the excitation energy of H_2CO is just near and above the threshold to the radical products (H+HCO): one kind is with modest vibrational H_2 and hot rotational CO; the other kind with highly vibrational H_2 and cold rotational CO. Recently, a fitted global PES for the ground state (S_0) based on *ab initio* calculations was constructed by Bowman and coworkers[2] and quasiclassical trajectory calculations (QCT) were also done on this PES[12]. Their results show good agreement with experiments and suggest the second kind of products is through a intramolecular hydrogen abstraction pathway, namely, the

roaming atom mechanism. Due to the limitation of QCT calculations about the zero point energy and tunneling effects, understanding this mechanism with quantum dynamical approaches is of great importance.

The second reaction modelled in this project is, $H+CH_4$, the reaction of hydrogen and methane. This reaction is important in combustion chemistry. Understanding of its dynamics is the basis for the design of new clean combustible materials. And the reaction is a prototype of polyatomic reaction and is of significant interest both experimentally and theoretically. The study of this reaction can have the insight into other polyatomic system which has more than four atoms. Due to the number of atoms in this reaction and the permutation symmetry of five H atoms, the construction of accurate global potential energy surface is very difficult, and the full dimensional dynamics is also very challenging. Based on an eight-dimensional model proposed by Palma and Clary[13] under the assumption that the CH_3 group keeps a C_{3V} symmetry in the reaction, we performed seven and eight dimensional dynamics calculations on the JG-PES, respectively, without or with the motion of non-reactive CH_3 symmetric stretching mode considered.

Although TD approach has a lower scaling factor with the computation basis, the TD calculation for polyatomic system with more than four atoms is a big challenge for theoretical chemists. The exponential increase in the size of the basis set for quantum dynamics calculations with the number of atoms makes it forbidden today to perform a full-dimensional study from first principle beyond four-atom reactions. Hence, to study quantum dynamical problems involving many atoms or many dimensions, one has to resort to the reduced dimensionality approach to cut down the number of degrees of freedom included in dynamical studies, like $H+CH_4$ reaction, or some computational approximate methods to overcome the scaling of effort with dimensionality. A promising approach is the time-dependent self-consistent field (TDSCF) method, such as the multi-configuration time-dependent Hartree (MCTDH) method[14], which has successfully been applied to study various realistic and complex quantum dynamical problems.

Recently, a new and efficient scheme for MC-TDSCF, namely, continuous-configuration time-dependent self-consistent field (CC-TDSCF) method is proposed[13]. The basic idea is to use discrete variable representation (DVR) for the system and then to each DVR point of the system a configuration of wavefunction in terms of direct product wavefunctions is associated for different clusters of the bath modes. In this way, the correlations between the system and bath modes, as well as the correlations between bath modes in each individual cluster can be described properly, while the correlations between bath modes in different clusters are neglected. Hence this approach

can present accurate results for those cases where the correlations between some bath modes are very small, and it is clear to see its efficient applications to large systems due to its simple size of basis functions which is determined by the product of the basis functions for the system and the sum of basis functions for each individual bath cluster.

In this project, we have tested the applications of this approach to three large or complex systems: H+CH_4, hydrogen diffusion on Cu(100) surface, and the double well coupled to a dissipative bath. The importance of studying H+CH_4 is mentioned before and recently a high quality full-dimensional PES[15] for this reaction was constructed in the vicinity of the saddle point for efficient calculations of the flux-flux correlation function and thermal rate constants. Then it is employed in this work to test the accuracy of the CC-TDSCF method for the H+CH_4 reaction. Hydrogen diffusion on Cu(100) surface has already been studied with the exact TSWP approach[16], which suggested that the motions of the surface are important to damp the recrossing of the transition state surface in order to converge the correlation function and determine the hopping rate. However, the applications of exact TSWP approach is limited if more surface modes considered, even though the eight important surface modes are sufficient to damp the recrossing. So in this work, a comparison calculation was performed with both exact TSWP approach and CC-TDSCF one to test the applications of CC-TDSCF to dynamical reactions on surfaces. The last complex system model studied, a double well coupled to a dissipative bath, is generally used to study the dynamics of a particle in condensed phase environments. Topaler and Makri[17] had used the quasiadiabtic path integral method to compute the numerically exact quantum rate for this system and then their computations served as benchmarks for many other approximate quantum theories. In this work, we performed both exact TSWP and CC-TDSCF calculations to study the transmission coefficients for different coupling parameters on the same model used by Topaler and Makri[17].

This thesis is organized as follows. Chapter 2 briefly reviews the theories: quantum reaction dynamics in time-dependent framework, the transition state wave packet (TSWP) approach and the quantum reaction rate calculations. Chapter 3 presents the transition state quantum dynamical studies of dissociation of formaldehyde on the ground state surface and the numerical details and results are discussed as well. In Chapter 4 the dynamics studies of H + CH_4 with the TSWP approach are presented and then the ($J = 0$) cumulative reaction probability and the thermal rate constant are described and discussed. Chapter 5 presents the theory about an approximation TDSCF method, continuous-configuration time-dependent self-consistent field (CC-TDSCF) approach, and the test calculations of this approach on three complex systems:

$H+CH_4$, hydrogen diffusion on Cu(100) surface, and the double well coupled to a dissipative bath. Finally, the summary part highlights the central results.

Chapter 2

Time-Dependent Quantum Dynamics

In the past three decades, time-dependent (TD) quantum dynamics method has evolved to be a very powerful theoretical tool in the simulation of reaction dynamics. In this chapter, we give a brief review of some basic concepts in molecular reaction dynamics[18]. We first introduce the approximation ways to separate the electronic and nuclear motions. Then two major parts of time-dependent quantum dynamics are presented: the Born-Oppenheimer potential energy surface construction and the following time-dependent wavepacket calculations. Finally one kind of time-dependent wavepacket approach, transition state wavepacket method (TSWP) is discussed in detail. Here some important numerical methods in computer simulation, such as, the split-operator method of time propagation, discrete variable representations, and collocation quadrature scheme, are also included.

2.1 Separation of Electronic and Nuclear Motions

The full molecular Hamiltonian may be written as,

$$H = \sum_i \frac{\hat{p}_i^2}{2m} + \sum_{j>i} \frac{e^2}{|r_i - r_j|} + \sum_i \frac{\hat{P}_i^2}{2M_i} + \sum_{j>i} \frac{Z_i Z_j e^2}{|R_i - R_j|} - \sum_{ij} \frac{Z_N e^2}{|r_i - R_j|} \quad (2.1)$$

$$= T_e + V_e + T_N + V_N + V_{eN} \quad (2.2)$$

where $\{r, \hat{p}\}$ is used to refer to the electron coordinates and momenta and $\{R, \hat{P}\}$ to refer to the nuclear coordinates and momenta. Z_i refers to the nuclear charge on nucleus i. Eq.(2.2) defines a shorthand notation for each of the five terms in Eq.(2.1), namely electron kinetic energy, electron-electron potential energy, nuclear kinetic energy, nuclear-nuclear potential energy, and

electron-nuclear potential energy. The time-independent Schrödinger equation (TISE) in the full space of electronic and nuclear coordinates is:

$$H(r,R)\Psi(r,R) = E\Psi(r,R) \tag{2.3}$$

where $\Psi(r,R)$ is an energy eigenfunction in the full coordinate space. Generally, there are two approximations applied to solve Eq.(2.3): the adiabatic and the diabatic approximation.

2.1.1 The Adiabatic Representation and Born-Oppenheimer Approximation

To find an approximate solution of Eq.(2.3), one can consider the TISE for electrons only at a fixed internuclear geometry, R,

$$H_e\phi_n(r,R) = \epsilon_n(R)\phi_n(r,R) \tag{2.4}$$

where $H_e = T_e + V_e + V_N + V_{eN}$. $\phi_n(r,R)$ and $\epsilon_n(R)$ are called adiabatic eigenfunctions and eigenvalues of the electrons with the fixed nuclear coordinates R as parameters. Since the adiabatic eigenfunction $\phi_n(r,R)$ form a complete orthonormal set, the molecular wave function $\Psi(r,R)$ in Eq.(2.3) can be expanded in the adiabatic basis $\phi_n(r,R)$,

$$\Psi(r,R) = \sum_n \chi_n(R)\phi_n(r,R) \tag{2.5}$$

where $\chi_n(R)$ is the corresponding nuclear wave function in the adiabatic representation. Substituting the expression in Eq.(2.5) into Eq.(2.3), and integrating over the electron coordinates, we obtain the coupled matrix equations,

$$\left[T(R) + \epsilon_m(R)\right]\chi_m(R) + \sum_n \Lambda_{mn}(R)\chi_n(R) = E\chi_m(R) \tag{2.6}$$

Here $\Lambda_{mn}(R)$ is the nonadiabatic coupling matrix operator which arises from the action of the nuclear kinetic energy operator $T(R)$ on the electron wave function $\phi_n(r,R)$,

$$\Lambda_{mn}(R) = -\hbar^2 \sum_i \frac{1}{M_i}\left(A^i_{mn}\frac{\partial}{\partial R_i} + \frac{1}{2}B^i_{mn}\right) \tag{2.7}$$

where the matrices are defined as,

$$A^i_{mn} = \langle\phi_m|\frac{\partial}{\partial R_i}|\phi_n\rangle = \int \phi^*_m \frac{\partial}{\partial R_i}\phi_n dr \tag{2.8}$$

$$B^i_{mn} = \langle\phi_m|\frac{\partial^2}{\partial R_i^2}|\phi_n\rangle = \int \phi^*_m \frac{\partial^2}{\partial R_i^2}\phi_n dr \tag{2.9}$$

Eq.(2.6) can be written in matrix form,

$$(\mathbf{T} + \mathbf{V})\mathbf{X}(R) = E\mathbf{X}(R) \tag{2.10}$$

where the diagonal matrix

$$\mathbf{V}_{mn}(R) = \epsilon_m(R)\delta_{mn} \tag{2.11}$$

is called the adiabatic potential and the nondiagonal kinetic matrix is given by

$$\mathbf{T}_{mn}(R) = T(R)\delta_{mn} + \Lambda_{mn}(R) \tag{2.12}$$

Thus in the adiabatic representation, the nuclear potential operator in the Schrödinger equation is diagonal while the kinetic energy operator is not.

Eq.(2.6) rigorously solves the coupled channel Schrödinger equation for the nuclear wave function in the adiabatic representation. The nonadiabatic coupling between different adiabatic states is given by the nonadiabatic operator of Eq.(2.7) which is responsible for nonadiabatic transitions. The direct calculation of the nonadiabatic coupling matrix is usually a very difficult task in quantum chemistry. In addition, the coupled equation (2.6) is difficult to solve. However, the adiabatic representation is so powerful because of the use of the adiabatic approximation in which the nonadiabatic coupling Λ_{mn} is neglected. This approximation is based on the rationale that the nuclear mass is much larger than the electron mass, and therefore the nuclei move much slower than the electrons. Thus the nuclear kinetic energies are generally much smaller than those of electrons and consequently the nonadiabatic coupling matrices A^i_{mn} and B^i_{mn}, which result from nuclear motions, are generally small.

If we neglect the nonadiabatic coupling, which is equivalent to retaining just a single term in the adiabatic expansion of the wave function,

$$\Psi(r, R) = \chi_n(R)\phi_n(r, R) \tag{2.13}$$

we obtain the adiabatic approximation for the nuclear wave function,

$$H^{ad}_n \chi_n(R) = E\chi_n(R) \tag{2.14}$$

where the adiabatic Hamiltonian is defined as

$$H^{ad}_n = T_N + \epsilon_n(R) + \Lambda_{nn}(R) \tag{2.15}$$

Since the electronic eigenfunction $\phi_n(r, R)$ is indeterminate to a phase factor of R, $e^{if(R)}$, a common practice is to choose $\phi_n(r, R)$ to be real. In this case, the function $A^i_{nn}(R)$ in Eq.(2.8)

vanishes and therefore the diagonal operator $\Lambda_{nn}(R)$ does not include differential operators. In most situations, the dependence of $B_{nn}(R)$ on nuclear coordinates R is relatively weak compared to that of the adiabatic potential $\epsilon_n(R)$. Thus the term $\Lambda_{nn}(R)$ is often neglected in the adiabatic approximation and one obtains the familiar Born-Oppenheimer approximation

$$[T_N + \epsilon_n(R)]\,\chi_n(R) = E\chi_n(R) \tag{2.16}$$

Thus in the adiabatic or Born-Oppenheimer approximation, one achieves a complete separation of electronic motion from that of nuclei: one first solves for electronic eigenvalues $\epsilon(R)$ at given nuclear geometries and then solves the nuclear dynamics problem using $\epsilon(R)$ as the potential for the nuclei. The physical meaning of the adiabatic or Born-Oppenheimer approximation is clear: the slow nuclear motion only leads to the deformation of the electronic states but not to transitions between different electronic states. The electronic wave function deforms instantaneously to adjust to the slow motion of nuclei. The general criterion for the validity of this approximation is that the nuclear kinetic energy be small relative to the energy gaps between electronic states such that the nuclear motion does not cause transitions between electronic states, but only distortions of electronic states.

2.1.2 The Diabatic Representation

Although the nonadiabatic couplings are ordinarily small (the basis of the Born-Oppenheimer approximation), they can become quite significant in some region, where the electronic states may change their character dramatically, and hence the derivatives of the type in Eq.(2.8 and 2.9) can be quite large. Moreover, the nonadiabatic coupling matrix is quite inconvenient to directly calculate in the adiabatic representation. Thus in solving nonadiabatic problems, one often starts from the diabatic representation.

In the diabatic representation, one chooses the electronic wave function calculated for a fixed reference nuclear configuration R_0 by solving the Schrödinger equation,

$$[H(r) + V_{eN}(r, R_0)]\,\phi_n(r, R_0) = \epsilon_n(R_0)\phi_n(r, R_0) \tag{2.17}$$

where the nuclear configuration R_0 is chosen at a fixed reference value regardless of the actual spatial positions of the nuclei. By using $\phi_n(r, R_0)$ as basis set, the molecular wave function can be expanded as

$$\Psi(r, R) = \sum_n \chi_n^0(R)\phi_n(r, R_0) \tag{2.18}$$

Substituting the expansion of Eq.(2.18) into Eq.(2.3) and integrating over the electronic wave function, one obtains the coupled equation for the nuclear wave function in the diabatic representation,

$$T_N\chi_m^0(R) + \sum_n U_{mn}(R)\chi_n^0(R) = E\chi_m^0(R). \tag{2.19}$$

Here the nondiagonal coupling U_{mn} arises from the electron-nuclear interaction $V_{eN}(r, R)$ and is given by

$$\begin{aligned} U_{mn}(R) &= \langle\phi_m|H_e + V_{eN}(R)|\phi_n\rangle & (2.20)\\ &= \epsilon_m(R_0)\delta_{mn} + \langle\phi_m|V_{eN}(R) - V_{eN}(R_0)|\phi_n\rangle & (2.21)\end{aligned}$$

Eq.(2.19) can be written in matrix form as

$$(\mathbf{T} + \mathbf{U})\mathbf{X}^0(R) = E\mathbf{X}^0(R) \tag{2.22}$$

where the kinetic energy operator is diagonal

$$\mathbf{T}_{mn}(R) = T_N\delta_{mn} \tag{2.23}$$

but the potential energy operator is nondiagonal with its matrix element give by Eq.(2.21). If the nondiagonal coupling can be neglected, we arrive at the diabatic approximation

$$[T_N + V_m^d(R)]\chi_m^0(R) = E\chi_m^0(R) \tag{2.24}$$

where the diabatic potential is given by $V_m^d(R) = U_{mm}(R)$.

Although the diabatic approximation is mathematically simpler because one only needs to carry out a calculation for the electronic wave function at a single fixed nuclear coordinate, it is less useful than the adiabatic approximation in practical situations in chemistry. This can be explained by the conditions of validity of both approximations. In the adiabatic representation, the nonadiabatic coupling is caused by the nuclear kinetic energy operator or nuclear motion which acts like a small perturbation. Thus the condition for the validity of the adiabatic approximation is that the nuclear kinetic energy be relatively small compared to energy gaps between the adiabatic electronic states. This is not too difficult to achieve because of the large mass differential between the electrons and nuclei. A crude estimation gives a rough ratio of $M/m_e \geq 1800$ where m_e and M are, respectively, the electron and nuclear mass. Another way to understand this is from the time-dependent point of view in that the electrons can quickly adapt themselves to the new configuration of the nuclei if the latter move slowly enough. Thus if

the nuclei are not moving too fast (having too much kinetic energy in comparison to the energy gaps between the adiabatic states), the adiabatic approximation should be a reasonably good approximation. On the other hand, the validity condition of the diabatic approximation is quite the opposite. In the diabatic representation, the coupling of electronic diabatic states is caused by the electron-nuclear interaction potential $V_{eN}(r, R)$. Thus the validity of the diabatic approximation requires that this interaction be small compared to the nuclear kinetic energy as can be seen from Eq.(2.24). Again using the time-dependent point of view, this condition is satisfied if the nuclei move very fast because in this case the electrons do not have sufficient time to adjust to the nuclear motion and their wave function will remain the same as R_0. To summarize, we can think of the adiabatic approximation as the low kinetic energy limit of the nuclear motion, while the diabatic approximation as the high kinetic energy limit of the nuclear motion.

2.2 The Born-Oppenheimer Potential Energy Surface (PES)

As discussed in Eq.(2.6), solving the Schrödinger equation for a molecular system requires a potential energy surface within the adiabatic or Born-Oppenheimer approximation. The simplest potential energy surfaces, for example, the harmonic potential and the Morse potential, are commonly used as one-dimensional potential energy surface in quantum chemistry. For a molecule with N atoms, the corresponding PES is a function of $3N-6$ (nonlinear system) or $3N-7$ (linear system) coordinates.

Researches into PESs for reactive systems began by adopting some rather complicated functional form where the multitude of parameters are chosen to obtain agreement with *ab initio* energy calculations at selected reference configurations or with energies inferred from experimental data. That is to form analytical potential energy surfaces and a famous derived one is the LEPS (Lenard-Eyring-Polanyi) potential surface for $H+H_2$. However, the construction of such analytical function form is proved to be difficult as the number of atoms/coordinates increases. Therefore, some alternative methods are applied to construct a global PES, such as the fitting and Shepard interpolation method, based on a large number of *ab initio* molecular orbital calculations. Significant advances have been made over many years in the accurate *ab initio* evaluation of the molecular energy. Further information about the shape of the energy surface may be obtained from evaluating derivatives of the energy with respect to the nuclear coordinates; derivatives up to second order may be obtained at reasonable computational cost at various levels of *ab initio* theory. These kinds of *ab initio* calculations, as well as the fitting and interpolation methods,

had made an accurate and efficient PES construction become possible.

Recently a systemic interpolation method for PES construction has been proposed by Collins and coworkers[19, 20, 21, 22, 23, 24, 25, 26, 27, 28, 29], where the local PES is first determined as the second-order Taylor series in terms of *ab initio* energy and energy derivatives at selected reference points in configuration space, and then the global PES is generated by interpolating those local PESs using a weight function (the modified Shepard interpolation scheme). In this scheme, the reaction path PES is generated by setting reference points along the IRC, and the PES can be easily improved by adding reference points in the dynamically significant regions. The search for such significant regions can be done efficiently by an iterative procedure of classical trajectory simulations on the interpolated PES, or by the *ab initio* direct-trajectory simulations. As the number of reference points increases, the interpolated PES should converge to an accurate Born-Oppenheimer PES. This section will briefly discuss this interpolation method since it is widely used in our group for PES construction.

For a molecular system with N atoms, the PES can be constructed using all the interatomic distance, $\mathbf{R}$ as coordinates. In practice, it is the corresponding inverse distances, $\mathbf{Z}(\{Z_n = \frac{1}{R_n}\})$ to be used, because the potential energy diverges to infinity when any two atoms are at the same position and therefore it is not an analytical function of the atomic coordinates. Using the $\mathbf{Z}$ to describe the PES means that these singularities are banished to infinity, $Z_n \to \infty$, resulting in a much better behaved description of the PES. However, there are $N(N-1)/2$ Z_n and only $3N-6$ independent coordinates which define the shape of a molecule. When $N > 4$ there appear to be some redundant Z_n. So Collins *et al.* use a variant of the Wilson $\mathbf{B}$ matrix to locally define a set of $3N-6$ independent internal coordinates as linear combination of the $\{Z_n\}$. Thus at a certain configuration, $\mathbf{Z}$, let ξ denote the $3N-6$ local internal coordinates. The potential energy at a configuration, $\mathbf{Z}$, in the vicinity of a reference data point, $\mathbf{Z}(i)$, can be expanded as a Taylor series to second order, T_i,

$$T_i(\mathbf{Z}) = V[\mathbf{Z}(i)] + \sum_{n=1}^{3N-6} [\xi_n - \xi_n(i)] \frac{\partial V}{\partial \xi_n}\bigg|_{\xi(i)} + \frac{1}{2} \sum_{n=1}^{3N-6} \sum_{m=1}^{3N-6} [\xi_n - \xi_n(i)][\xi_m - \xi_m(i)] \frac{\partial^2 V}{\partial \xi_n \partial \xi_m}\bigg|_{\xi(i)} \quad (2.25)$$

where $V[\mathbf{Z}(i)]$ is the electronic energy at the configuration $\mathbf{Z}(i)$. The first and second potential energy derivatives with respect to the local internal coordinates are also evaluated at this configuration, $\mathbf{Z}(i)$.

In the modified Shepard interpolation method, the potential energy surface at any configuration $\mathbf{Z}$ is given as a weighted average of the Taylor series about all N_d data points and their symmetry equivalents: (Noted here although the $\mathbf{Z}$ coordinates may be locally redundant, they

can be used globally.)

$$V(\mathbf{Z}) = \sum_{g\in G}\sum_{i=1}^{N_d} w_{g\circ i}(\mathbf{Z}) T_{g\circ i}(\mathbf{Z}) \tag{2.26}$$

where the weight function $w_i(\mathbf{Z})$, which gives the contribution of the ith Taylor expansion to the potential energy at the configuration $\mathbf{Z}$, is set as,

$$w_i(\mathbf{Z}) = \frac{\upsilon_i(\mathbf{Z})}{\sum_{g\in G}\sum_{k=1}^{N_d} \upsilon_{g\circ k}(\mathbf{Z})} \tag{2.27}$$

The un-normalized weight function $\upsilon_i(\mathbf{Z})$ thus has the following properties,

$$\begin{aligned} &\upsilon_i(\mathbf{Z}) \to 0, \qquad as|\mathbf{Z}-\mathbf{Z}_i| \to \infty \\ &\upsilon_i(\mathbf{Z}) \to \infty, \qquad as|\mathbf{Z}-\mathbf{Z}_i| \to 0. \end{aligned} \tag{2.28}$$

Consistent with Eq.(2.28), the following form for $\upsilon_i(\mathbf{Z})$ has been adopted,

$$\upsilon_i = \left\{ \left[\sum_{n=1}^{N(N-1)/2} \left(\frac{Z_n - Z_n(i)}{d_n(i)}\right)^2 \right]^{\frac{q}{2}} + \left[\sum_{n=1}^{N(N-1)/2} \left(\frac{Z_n - Z_n(i)}{d_n(i)}\right)^2 \right]^{\frac{p}{2}} \right\}^{-1} \tag{2.29}$$

where $p > 3N-3$, and $q > 2$, but $q \ll p$. The quantities $\{d_n(i), i = 1, 2, \cdots, N(N-1)/2\}$ $rad(i)$ define a confidence volume about the ith data point. If $\sum_{n=1}^{N(N-1)/2}(Z_n - Z_n(i))^2/d_n(i)^2 \ll 1$, then the first term on the right-hand side of Eq.(2.29) dominates, and υ_i falls relatively slowly only with the low power q, while if $\sum_{n=1}^{N(N-1)/2}(Z_n - Z_n(i))^2/d_n(i)^2 \gg 1$, the second term dominates, and υ_i is rapidly damped by the high power, p. An important consequence of this two-part weight function is that the relative weights of two or more data point near $\mathbf{Z}$ vary only slowly with varying $\mathbf{Z}$. The confidence lengths, $\{d_n(i)\}$, are determined by a Bayesian analysis of the inaccuracy of the ith Taylor expansion at M configurations close to $\mathbf{Z}(i)$,

$$d_n(i)^{-6} = \frac{1}{M}\sum_{k=1}^{M} \frac{\{\left[\frac{\partial V[\mathbf{Z}(k)]}{\partial Z_n}|_{\mathbf{Z}(k)} - \frac{\partial T_i[\mathbf{Z}(k)]}{\partial Z_n}|_{\mathbf{Z}(k)}\right][Z_n(k) - Z_n(i)]\}^2}{E_{tol}^2 \|\mathbf{Z}(k) - \mathbf{Z}(i)\|^6} \tag{2.30}$$

Once there are sufficient data points available, the most accurate interpolation is given by Eq.(2.26) with the weight function defined by Eqs.(2.27), (2.29), and (2.30).

The accuracy of the PES improves with an increase in the number of data points, N_d. The optimum or most efficient improvement in the accuracy of the PES would require careful choice of the locations of any data points added to the set. The task of improving the PES therefore involves finding the locations of a finite sequence of data points which are to be added to the set in Eq.(2.26) until the measured dynamical average converge. A geometrical approach is adopted

by the iterative use of classical trajectories to locate those regions of configuration space which are important for the dynamical process. In brief, an initial set of data points is chosen in lie to or near the relevant reaction path. The potential of Eq.(2.26) is then defined, albeit as a poor approximation to the exact PES at the level of *ab initio* theory. Classical trajectories are evaluated on this PES, with initial conditions appropriate to the reaction of interest, in order to explore the relevant region of configuration space. Molecular configurations encountered during these trajectories are recorded. One or more of these configurations is then chosen to be a new data point; the *ab initio* energy, gradient, and second derivatives are evaluated at the point which is then added to the data set, generating a new version of the PES. This process of simulating the reaction, choosing a configuration, performing the *ab initio* calculation and adding a new data point to the set is repeated again and again until the PES is converged. Convergence is established by calculating the quantum reaction probability for a range of relative translational energies of the reactants, using the first N_d points in the interpolation data set. When the reaction probability does not change significantly with increasing N_d, the PES is taken to be converged.

2.3 Time-Dependent Quantum Dynamics

2.3.1 Time-Dependent Schrödinger Equation

In the time-dependent (TD) approach, the starting point is the TD Schrödinger equation:

$$i\frac{\partial}{\partial t}\Psi(t) = \hat{H}\Psi(t) \tag{2.31}$$

where $\hat{H}$ is the Hamiltonian operator, being time-dependent or time-independent, and $\Psi(t)$ is the TD wave function. Here, we assume the Hamiltonian $\hat{H}$ is time-independent. Let $\Psi(0)$ be a scattering solution of the time-dependent Schrödinger equation at $t = 0$; the wave function $\Psi(t)$ satisfying Eq.(2.31) is in the Schrödinger representation (SR), and has the formal solution

$$\Psi(t) \quad = \quad e^{-i\hat{H}t}\Psi(0). \tag{2.32}$$

Therefore, solving Eq.(2.31) constitutes an initial value problem in which one propagates the wave function $\Psi(t)$ in time after an initial wave function $\Psi(t_0)$ is specified. The initial time t_0 is usually set to be zero for convenience.

2.3.2 Wave Function Propagation

For a given initial wave function $\Psi(0)$, a propagation of the wave function is carried out by integrating methods to solve Eq.(2.32). The most straightforward approach is based on finite difference schemes include Runga-Kutta method, second-order difference (SOD), or higher-order difference methods. At present, however, more sophisticated methods, such as the split operator (SP) method[30, 31], Chebychev polynomial method[32], short iterative Lanczos method[33, 34, 35, 36] as well as other methods, are often used in practical applications. In this project, we use split-operator method to propagate wave function. Here, we briefly describe the method.

The split operator method is extremely popular and has been widely used in many practical applications. It approximates the short time propagator by the equation,

$$e^{-i\hat{H}\Delta} = e^{-i\hat{K}\Delta/2}e^{-i\hat{V}\Delta}e^{-i\hat{K}\Delta/2} + O(\Delta^3) \tag{2.33}$$

where the Hamiltonian $\hat{H}$ is split into two parts as $\hat{H} = \hat{K} + \hat{V}$ and thus the wavefunction is propagated by the formula

$$\Psi(t+\Delta) = e^{-i\hat{K}\Delta/2}e^{-i\hat{V}\Delta}e^{-i\hat{K}\Delta/2}\Psi(t) \tag{2.34}$$

The error introduced in Eq.(2.33) is of third order ($O(\Delta^3)$) and is related to the commutator $[\hat{K}, \hat{V}]$, which can be easily verified by expanding the propagators on the left side and right side in Eq.(2.33) as Taylor series.

The split-operator propagator is a short-time propagator and its application is thus very flexible. For example, it can be applied to complex or time-dependent Hamiltonian without any modification. In addition, the split-operator propagation of $\Psi(t)$ is explicitly unitary, which is a main factor contributing to the numerical stability of the solution with respect to time step of the propagation. Also, besides the step size Δ, there is no other numerical parameters to vary in computation. Thus, it is a quite robust propagator for general time-dependent applications.

In numerical calculation, the wavefunction is expressed in a basis representation, and the operator is thus in matrix form. The propagator in Eq.(2.33) thus requires one to handle the exponential operator or matrix in numerical calculation. The standard method to handle the matrix in exponential form $e^{\alpha\mathbf{A}}$, where $\mathbf{A}$ is hermitian or orthogonal, is to diagonalize the matrix $\mathbf{A}$

$$\mathbf{A} = \mathbf{U}^\dagger\mathbf{A}_D\mathbf{U} \tag{2.35}$$

to make

$$e^{\alpha\mathbf{A}} = \mathbf{U}^\dagger e^{\alpha\mathbf{A}_D}\mathbf{U} \tag{2.36}$$

where $\mathbf{A}_D$ is the diagonal matrix. This procedure guarantees the unitarity of the propagation. The diagonalization step is equivalent to changing the wavefunction representation to the one that diagonalizes the operator. Since the operators $\hat{K}$ and $\hat{V}$ in Eq.(2.33) do not commute, there is a need to carry out transformations from diagonal representation of one operator to that of another. For example in a one dimensional problem, if the $\hat{K}$ is the kinetic energy operator and $\hat{V}$ is a local potential operator, one needs to transform from a local representation in coordinate space to a local one in momentum space, and then transform back to the coordinate representation, in completing a propagation step in Eq.(2.33).

2.3.3 Reactive Flux and Reaction Probability

The conservation relation corresponding to the TD Schrödinger equation $i\hbar\frac{\partial}{\partial t}\Psi = \hat{H}\Psi$ can be written as a continuity equation

$$\frac{\partial \rho}{\partial t} + \nabla \cdot J = 0 \tag{2.37}$$

where the divergence operator is defined in the $N-1$-dimensional hypersurface. Here the density is given by $\rho = |\Psi(t)|^2$ and the flux is defined by the equation

$$\nabla \cdot J = \frac{i}{\hbar}[\Psi^* \hat{H}\Psi - (\hat{H}\Psi)^*\Psi] \tag{2.38}$$

For any stationary wavefunction Ψ, ρ is independent of time, so $\nabla \cdot J = 0$. This means that the flux is constant across any fixed hypersurface. If the Hamiltonian $\hat{H}$ can be expressed as the sum of a kinetic energy operator for the coordinate s and a reduced Hamiltonian for the remaining N-1 degrees of freedom

$$\hat{H} = \frac{\hat{p}_s^2}{2m_s} + \hat{H}_s \tag{2.39}$$

where $\hat{H}_s$ is the reduced Hamiltonian, then we can evaluate the flux at a fixed surface at $s = s_0$ by integrating over the remaining $N-1$ coordinates in Eq.(2.38)

$$J_s = \langle\psi|\hat{F}|\psi\rangle \tag{2.40}$$

where the flux operator $\hat{F}$ is defined as

$$\begin{aligned} \hat{F} &= \frac{1}{2}[\delta(s-s_0)\frac{\hat{p}_s}{m_s} + \frac{\hat{p}_s}{m_s}\delta(s-s_0)] \\ &= \mathrm{Im}[\frac{\hbar}{m_s}\delta(s-s_0)\frac{\partial}{\partial s}] \end{aligned} \tag{2.41}$$

Since the flux J_s is a constant and therefore independent of the position of the surface to calculate, we can of course evaluate the reactive flux at a fixed surface in the asymptotic region of the product. By using the **S** matrix asymptotic boundary condition for the reactive scattering wavefunction, for $\alpha \neq \beta$, we can calculate the flux at a surface with a fixed value of $s = R_\beta$ to obtain

$$J_s = \sum_n |\mathbf{S}_{\beta n,\alpha i}|^2 \tag{2.42}$$

Thus the reactive flux gives the total reaction probability

$$P_{\alpha i} = J_s = \langle \psi_{\alpha i} | \hat{F} | \psi_{\alpha i} \rangle \tag{2.43}$$

where $P_{\alpha i}$ is the total $\alpha(i) \rightarrow \beta(all)$ reaction probability. In TD calculations, however, it is preferable to evaluate the reactive flux at a location near the transition state because this will generally shorten the propagation time needed to converge the flux.

2.4 Transition State Time-Dependent Quantum Dynamics

2.4.1 Thermal Rate Constant and Cumulative Reaction Probability

One of the most fundamental and important tasks in chemical reaction dynamics is the accurate evaluation of thermal rate constants. As is known, the exact thermal rate constant for an elementary bimolecular reaction ($A + B \rightarrow P$) can be rigorously calculated by Boltzmann averaging the reactive flux over the initial states and the collision energy

$$k(T) = \frac{4\pi}{Q_{int}} \sum_{fi} e^{-\epsilon_i/kT} \int_0^\infty (\frac{\mu}{2\pi kT})^{3/2} \upsilon_i^3 exp(-\frac{\mu \upsilon_i^2}{2kT}) \sigma_{fi}(\upsilon_i) d\upsilon_i \tag{2.44}$$

where μ is the translational mass, ϵ_i is the eigenenergy of the internal state of the colliding partners, and υ_i is the relative speed of the collision. The quantum partition function Q_{int} is defined as

$$Q_{int} = \sum_i e^{-\epsilon_i/kT} \tag{2.45}$$

where the summation is over all energetically accessible internal states of the reagents. The reaction cross section σ_{fi} in Eq.(2.44) is given by the formula

$$\sigma_{fi} = \frac{\pi \hbar^2}{\mu^2 \upsilon_i^2} \sum_J (2J+1) |S_{fi}^J|^2 \tag{2.46}$$

where S_{fi}^{J} is the state-to-state reactive **S** matrix element.

Using the definition in Eqs.(2.45 and 2.46), the rate Eq.(2.44) can be rearranged to give rise to the following result

$$k(T) = \frac{1}{2\pi\hbar}\frac{1}{Q_r}\int_0^\infty N(E)e^{-E/kT}dE \tag{2.47}$$

where Q_r is the total partition function for the reactants $A + B$ and $N(E)$ is the cumulative reaction probability defined as the sum over both initial and final states of reaction probability

$$N(E) = \sum_J (2J+1)\sum_{fi}|S_{fi}^{J}|^2 \tag{2.48}$$

Therefore, one rigorous way to determine the rate constant is to solve the complete state-to-state reactive scattering Schrödinger equation to obtain the S-matrix as a function of total energy E and total angular momentum J, from which all the state-to-state scattering cross sections can be obtained. Boltzmann averaging these cross sections over initial quantum states, and summing over all final quantum state produces the rate constant, but this is in a sense wasteful if one seeks only the rate constants itself.

Since the thermal rate constant is determined by the cumulative reaction probability $N(E)$ without any explicit reference to state-to-state quantities, it is desirable to directly calculate $N(E)$ without having to solve the complete state-to-state reactive scattering problem. Physically, the reaction rate is determined by the dynamics in a relatively small region near the transition state, so direct calculation of $N(E)$ should be computationally advantageous since it involves only short time dynamics in a small spatial region. Such approach is formally possible and there is an elegant formula for direct calculations of $N(E)$ by Milller[7, 6],

$$N(E) = \frac{(2\pi\hbar)^2}{2}tr[\delta(E-\hat{H})\hat{F}\delta(E-\hat{H})\hat{F}], \tag{2.49}$$

where $\hat{H}$ is the total Hamiltonian of the molecular system, and $\hat{F}$ is the quantum flux operator defined as,

$$\hat{F} = \frac{1}{2\mu}[\delta(q-q_0)\hat{p}_q + \hat{p}_q\delta(q-q_0)], \tag{2.50}$$

where μ is the reduced mass of the system, q is the coordinate perpendicular to a dividing surface located at $q = q_0$ which separates products from reactants, and $\hat{p}_q$ is the momentum operator conjugate to the coordinate q. Because the flux through any dividing surface which separates products from reactants is equal, the dividing surfaces for the two $\hat{F}$ operators in Eq.(2.49) can be chosen at different positions.

Another famous form of the thermal rate constant expression can be obtained from the flux-flux autocorrelation function C_{ff} as,

$$k(T) = \frac{1}{Q_r}\int_0^\infty C_{ff}(T,t)dt \tag{2.51}$$

where

$$C_{ff}(T,t) = Tr[e^{-\beta\hat{H}/2}e^{i\hat{H}t}\hat{F}e^{-i\hat{H}t}e^{-\beta\hat{H}/2}\hat{F}] \tag{2.52}$$

and $\beta = 1/k_bT$. Eqs.(2.49 and 2.52) have been widely applied to calculate cumulative reaction probabilities, flux-flux autocorrelation functions and rate constants.

If we perform a partial integration in Eq.(2.47), the rate constant can be rewritten in a more suggestive form

$$r = \frac{kT}{2\pi\hbar}\frac{1}{Q_AQ_B}\int_0^\infty \rho(E)e^{-E/kT}dE \tag{2.53}$$

where $\rho(E) = \frac{dN(E)}{dE}$. The quantity $\rho(E)$ might be considered as a density of states from which we can define a partition function

$$Q_{ex}^{\ddagger} = \int_0^\infty e^{-E/kT}\rho(E)dE \tag{2.54}$$

$$= \frac{1}{kT}\int_0^\infty e^{-E/kT}N(E)dE \tag{2.55}$$

Thus the rate equation can be put in the form

$$r = \frac{kT}{2\pi\hbar}\frac{Q_{ex}^{\ddagger}}{Q_AQ_B} \tag{2.56}$$

Eq.(2.56) is in exactly the same form as the classical transition state theory (TST) expression for the rate constant

$$r_{tst} = \frac{kT}{h}\frac{Q_c^{\ddagger}}{Q_AQ_B} \tag{2.57}$$

where $Q_c^{\ddagger}$ is the true partition function at the transition state. However, it it important to point out that the rate Eq.(2.56) is the exact quantum mechanical result while the TST rate Eq.(2.57) is the classical transition state approximation. Comparing the exact quantum rate expression Eq.(2.56) with the transition state expression Eq.(2.57), we can try to associate the quantum mechanical quantity $Q_{ex}^{\ddagger}$ with the quantum partition function at the transition state. Thus the analogy to TST gives a physically intuitive meaning to the exact quantum cumulative reaction probability $N(E)$: it represents the total number of open channels (states) at total energy E at the transition state. However, this is not a transition state theory, since calculation of $N(E)$ is equivalent to solving the Schrödinger equation; i.e., it generates the complete quantum dynamics.

2.4.2 Transition State Wave Packet Method

The quantum transition state wavepacket method [8, 9, 10, 16] was developed mainly to calculate the cumulative reaction probability, the flux-flux autocorrelation function, and the thermal rate constants based on the famous formulation given by Miller and coworker, i.e., Eqs.(2.49 and 2.52), as well as the significant progress in time-dependent wave packet techniques. As shown in Eq.(2.49), the cumulative reaction probability can be expressed [in atomic units ($\hbar = 1$)]as

$$N(E) = \frac{(2\pi\hbar)^2}{2} tr[\delta(E - \hat{H})\hat{F}\delta(E - \hat{H})\hat{F}], \tag{2.58}$$

where $\hat{H}$ is the total Hamiltonian of the molecular system, and $\hat{F}$ is quantum flux operator defined as in Eq.(2.50). It is well known that in one dimension there only exist two nonzero eigenvalues for any finite real basis for a flux operator, with all other eigenvalues being degenerate with value zero. The two nonzero eigenvalues are a $\pm$ pair and the corresponding eigenstates are also complex conjugates because a matrix representation of $\hat{F}$ is imaginary antisymmetric, i.e., Hermitian. If the eigenvectors corresponding to the nonzero eigenvalues $\pm\lambda$ are $|+\rangle$ and $|-\rangle$, i.e., $\hat{F}|\pm\rangle = \pm\lambda|\pm\rangle$, and ϕ_i $(i = 1, n)$ forms a complete basis set for the coordinates other than the coordinate q, i.e., on a dividing surface S_1 $H_{S_1}|\phi_i\rangle = \epsilon_i|\phi_i\rangle$, the trace in Eq.(2.58) can be simplified as

$$N(E) = \frac{(2\pi)^2}{2}\lambda \sum_i [\langle\phi_i^+|\delta(E - \hat{H})\hat{F}\delta(E - \hat{H})|\phi_i^+\rangle - \langle\phi_i^-|\delta(E - \hat{H})\hat{F}\delta(E - \hat{H})|\phi_i^-\rangle] \tag{2.59}$$

where the initial transition state wave packet $\phi_i^{\pm}$ denotes the direct product of ϕ_i with $|+\rangle$ or $|-\rangle$, respectively. Because $\delta(E - \hat{H})\hat{F}\delta(E - \hat{H})$ is a Hermitian operator, each term on the right-hand side of Eq.(2.59) is real. Utilizing the equalities, $\hat{F}^* = -\hat{F}$ and $|-\rangle = |+\rangle^*$, we easily find

$$\begin{aligned} &\langle\phi_i^-|\delta(E - \hat{H})\hat{F}\delta(E - \hat{H})|\phi_i^-\rangle \\ &= \langle\phi_i^-|\delta(E - \hat{H})\hat{F}\delta(E - \hat{H})|\phi_i^-\rangle^* \\ &= -\langle\phi_i^+|\delta(E - \hat{H})\hat{F}\delta(E - \hat{H})|\phi_i^+\rangle \end{aligned} \tag{2.60}$$

Thus $N(E)$ in Eq.(2.59) can be written

$$N(E) = (2\pi)^2\lambda \sum_i \langle\phi_i^+|\delta(E - \hat{H})\hat{F}\delta(E - \hat{H})|\phi_i^+\rangle \tag{2.61}$$

Writing $\delta(E - \hat{H})$ in the widely used fourier transform fashion and splitting λ equally, we define

$$\psi_i(E) = \sqrt{\lambda}2\pi\delta(E - \hat{H})|\phi_i^+\rangle = \sqrt{\lambda}\int_{-\infty}^{+\infty} e^{i(E-\hat{H})t}dt|\phi_i^+\rangle \tag{2.62}$$

where the energy-dependent wave functions $|\psi_i(E)\rangle$ are calculated on the second dividing surface. The cumulative reaction probability $N(E)$ then can be written as,

$$N(E) = \sum_i \langle\psi_i|\hat{F}|\psi_i\rangle = \sum_i N_i(E) \tag{2.63}$$

where $N_i(E) = \langle\psi_i|\hat{F}|\psi_i\rangle$ is the contribution to $N(E)$ from the ith transition state wave packet. Therefore, $N(E)$ can be calculated as follows: (1) prepare initial wave packets on any dividing surface S_1 by taking the direct product of the one dimensional eigenstate of the flux operator $|+\rangle$ and basis functions for the other coordinates; (2) propagate each of these wave packets once to generate wave function ψ_i at all energies desired; (3) calculate the flux for each ψ_i on any dividing surface S_2 and add them together to obtain $N(E)$. Here some details are to be discussed for this approach.

The first is about the flux operator. Because the flux operator $\hat{F}$ is singular operator, i.e., its nonzero eigenvalues and the corresponding eigenstates depend on the basis set. As the representation becomes exact, the largest eigenvalue will go to infinity. Hence the $N_i(E)$ will depend somewhat on the basis set for coordinate q in Eq.(2.50). However the sum converges to $N(E)$. The traditional transition state can be regarded as the limit when the basis set for coordinate q is exact; then the largest eigenvalue of F goes to infinity, and the corresponding eigenstate localizes to a point at $q = q_0$.

Secondly, how to choose the two dividing surfaces? Since the flux through any dividing surface which separates products from reactants is equal, the dividing surfaces for the two $\hat{F}$ operators in Eq.(2.58) can be chosen at different positions. If S_1 is chosen at the translational coordinate S in the asymptotic region. Then the total Hamiltonian H reduce to

$$\hat{H} = \hat{H}_0 = \hat{T}_S + \hat{H}_{\overline{S}} \tag{2.64}$$

where $\overline{S}$ represents the coordinates other than S, and $\hat{H}_{\overline{S}}$ is the Hamiltonian for these coordinates. Because the kinetic energy for S is positive in the asymptotic region, the energy in S should be smaller than total scattering energy E. Thus if we choose the asymptotic internal channel basis of the system, i.e., $\hat{H}_{\overline{S}}\phi_i = E_i\phi_i$, as the basis functions for the other internal coordinates, the sum in Eq.(2.63) only needs to include all the open channels for a scattering energy. In this case, Eq.(2.63) can be written as

$$N(E) = \sum_i P_i(E) \tag{2.65}$$

where P_i defined as $P_i(E) = \langle\Psi_i|F|\Psi_i\rangle$ is just the cumulative reaction probability for an initial state i. The sum of P_i gives the cumulative reaction probability $N(E)$ which of course can also be

achieved by calculating the initial state selected cumulative reaction probability using the regular wave packet approach.

If S_1 is chosen at the coordinate of S equal to a large value, the only difference between Eq.(2.63) and the initial state selected wave packet approach (ISSWP) is that in Eq.(2.63) one propagates a wave packet which is the eigenstate of flux operator for S, while one usually propagates a Gaussian wave packet in the initial state selected wave packet approach. However, the importance difference between these two approaches actually is that one can only propagate Gaussian wave packets for initial state at large S in the initial state selected wave packet approach, but one can choose any dividing surface as S_1 and thus propagate wave packets from any dividing surface with Eq.(2.62). This means we can choose a S_1 on which the density-of-states for other coordinates is minimized. This will reduce the number of wave packets we need to propagate, since the density-of-states for other coordinates on a dividing surface usually strongly dependent on the location of the surface. In particular, for a reaction involving multiple rotational degrees of freedom with a barrier on the PES, the density-of-states on a dividing surface passing through the saddle point of the potential surface is usually significantly lower than that in the asymptotic region. In this case even though some close transition states with energy higher than the total energy can also contribute to the $N(E)$ due to the quantum tunneling effects, the number of wave packets we need to propagate will be significantly smaller than that required in the regular wave packet approach in which the initial wave packet can only be located in asymptotic region.

The second dividing surface S_2 is chosen to evaluate the flux in Eq.(2.63) at $x = x_0$, here x can be any coordinate as long as the surface $x = x_0$ divides the product from the reactant. The final equation to calculate the cumulative reaction probability,

$$N(E) = \sum_i \left\{ \frac{1}{\mu} \sum_n Im \left[(C_n^i)^* \frac{\partial C_n^i}{\partial x} \right] \Big|_{x=x_0} \right\} \tag{2.66}$$

where C_n^i is the expansion coefficient for ψ_i on φ_n, which is the basis set for y (the coordinates other than x), i.e.,

$$\psi_i(x, y) = \sum_n C_n^i(x) \varphi_n(y). \tag{2.67}$$

If S_2 is chosen at a large value of x, and φ_n is the internal basis with n representing the collection of rovibrational quantum numbers for the system in the asymptotic region, then Eq.(2.66) can be written as

$$N_i(E) = \sum_n P_n^i \tag{2.68}$$

where P_n^i is just the cumulative reaction probability to produce the final state n from the ith transition state wave packet. P_n^i is given from Eq.(2.66) as,

$$P_n^i = \frac{1}{\mu} Im \left[(C_n^i)^* \frac{\partial C_n^i}{\partial x} \right] \Bigg|_{x=x_0} \tag{2.69}$$

While Eqs.(2.65) and (2.69) both give the cumulative reaction probability for an initial state, they are totally different in their origins. For Eq.(2.65), S_1 is located at a large value of S where the initial wave packets are constructed. These are propagated and measurements of the flux on surface S_2 give the initial state selected cumulative reaction probability as in the regular wave packet approach. For Eq.(2.69), the surface S_1 can be located at any position which means the initial flux wave packets can be started from any position, but the projection of the flux into internal states at a larger value of S will also give the initial state selected cumulative reaction probability.

Eq.(2.69) not only provides an alternative to the time-dependent wave packet approach to the initial state selected total reaction probability, but it can be more efficient. It should be used for systems with several rotation degrees of freedom when one is interested in total reaction probabilities from a substantial number of initial rotation excited states. Of course Eq.(2.69) is not a good choice if only the reaction probabilities from a few initial states are desired because one needs to propagate a number of transition state wave packets which all will contribute to P_n^i in Eq.(2.69).

As can be seen from Eq.(2.62), the present method has one very attractive feature: one is only required to propagate these transition state wave packets once to obtain the $N(E)$ at all energies. When the energy dependence of $N(E)$ is known, the thermal rate constant is a matter of Boltzmann averaging,

$$k(T) = \frac{1}{2\pi Q_r(T)} \int_0^\infty dE e^{-\beta E} N(E), \tag{2.70}$$

where $Q_r(T)$ is the reactant partition function per unit volume and $\beta = \frac{1}{k_b T}$. Thus the present method is a direct way to calculate thermal rate constants. One should note that the transition state wave packet idea can also apply directly to the flux-flux correlation function calculation to the thermal rate constant by propagating the flux operator eigenstates. The thermal rate constant can be expressed in terms of flux-flux autocorrelation function as,

$$k(T) = \frac{1}{Q_r} \int_0^\infty C_{ff}(T,t) dt, \tag{2.71}$$

where the flux-flux autocorrelation function $C_{ff}(T,t)$ is given by

$$C_{ff}(T,t) = tr(e^{i\hat{H}t_c^*} \hat{F} e^{-i\hat{H}t_c^*} \hat{F}), \tag{2.72}$$

where $t_c = t - i\beta/2$. Evaluating the trace in Eq.(2.72) as in Eq.(2.59), we can obtain,

$$\begin{aligned} C_{fs}(T) &= \lambda \sum_i \int_0^\infty [\langle \phi_i^+ | e^{i\hat{H}t_c^*} \hat{F} e^{-i\hat{H}t_c} | \phi_i^+ \rangle - \langle \phi_i^- | e^{i\hat{H}t_c^*} \hat{F} e^{-i\hat{H}t_c} | \phi_i^- \rangle] dt \\ &= \lambda \sum_i \int_{-\infty}^\infty \langle \phi_i^+ | e^{i\hat{H}t_c^*} \hat{F} e^{-i\hat{H}t_c} | \phi_i^+ \rangle dt \\ &= \lambda \sum_i \int_{-\infty}^\infty \langle \psi_i^+(t) | \hat{F} | \psi_i^+(t) \rangle dt \end{aligned} \tag{2.73}$$

where

$$|\psi_i^+(t)\rangle = e^{-i\hat{H}t} e^{-\beta\hat{H}/2} |\phi_i^+\rangle \tag{2.74}$$

From Eq.(2.74), one can see that we first propagate each transition state wave packet in imaginary time to $\beta/2$, then propagate it in real time. The total flux can be measured on the transition state dividing surface to achieve rapid convergence.

It is important to restate that the TSWP approach is similar to the regular time-dependent initial selected state wave packet (ISSWP) approach to reactive scattering except for the initial wavepacket construction. In the ISSWP approach, the initial wavepacket is usually a direct product of a gaussian wavepacket for the translational motion located in the reactant asymptotic region and a specific ($N-1$ dimensional) internal state for reactants. In the TSWP approach, the initial TSWPs are constructed as the direct products of the ($N-1$ dimensional) Hamiltonian eigenstates on the first dividing surface and the flux operator eigenstate with positive eigenvalue. Just because of the flexible choice of the dividing surfaces, the TSWP approach offers several advantages. First the starting flux surface may be located to minimize the number of wave packet propagations required to converge the results in a desired energy range. This will often be the TS surface for reactions with a barrier, but may be toward the reactant channel for exothermic reactions with loose transition states, etc. Second, the location of the second flux surface will depend on the information desired. If only the thermal rate constant is required, the two surface will normally be chosen to be the same. If a state cumulative reaction probability is required, for reaction from a given state or for reaction to a give state, then one flux surface must be located toward the appropriate asymptotic region where a projection of the flux on to the internal states is possible to obtain the reaction probability from each initial state, i.e., the information obtained from the ISSWP approach. Therefore, the cumulative reaction probabilities for all the open transition states are required to give the information from one initial state. So for a single initial state, the ISSWP is to be preferred since only one propagation is required. However, when information for many initial states is desired, and there is a barrier to reaction,

then the TSWP approach will converge with many few wavepacket propagations.

One feature of the TSWP approach which is less than ideal concerns the contributions of individual wave packets to the positive definite quantities desired, $N(E)$ or $N_i(E)$. The contribution of a given wave packet may be negative or slightly larger than 1 at some energies, leading to some uncertainty about convergence. Although negative contributions are observed, they are usually quite small and cause no real problem. This does mean, however, that one cannot speak of probabilities of reaction from a given TS within this formulation. However, convergence to zero contribution from very high energy transition states is observed. Finally, since the TSWPs are determined by the position of the dividing surface S_1, the convergence and behavior of $N_i(E)$ vary with the surface. Placement of S_1 in the traditional transition state region seems to yield the most rapid convergence with respect to the number of wavepackets required and also seems to produce N_i values that are "almost" probabilities.

2.5 Numerical Implementations

2.5.1 Discrete Variable Representation (DVR)

The Discrete Variable Representation(DVR) is a very general and powerful method which is widely used in quantum mechanics calculations[37]. It is applied to one-dimensional problems or direct product basis functions in multidimensional problems. To state it simply, DVR is a localized (in coordinate space) but discrete representation. For any given finite basis set $\phi_n(x)(n = 1, 2, 3, \cdots, N)$, one can define a unique DVR by diagonalizing the matrix

$$x_{mn} = \langle \phi_m | \hat{x} | \phi_n \rangle \tag{2.75}$$

which generates N eigenvalues x_n and eigenfunctions

$$|X_n\rangle = \sum_m |\phi_m\rangle C_{mn} \tag{2.76}$$

such that

$$\hat{x}|X_n\rangle = x_n|X_n\rangle \tag{2.77}$$

Eq.(2.77) implies that in this N-dimensional vector space, the coordinate operator $\hat{x}$ is approximated by

$$\hat{x} \quad = \quad \sum_{m=1}^{N} \sum_{n=1}^{N} |\phi_m\rangle x_{mn} \langle \phi_n|$$

$$= \sum_{n=1}^{N} |X_n\rangle x_n \langle X_n| \tag{2.78}$$

With this prescription for the operator $\hat{x}$, $|X_n\rangle$ is also an eigenstate of any operator function $F(\hat{x})$, i.e.,

$$F(\hat{x})|X_n\rangle = F(x_n)|X_n\rangle \tag{2.79}$$

Since the DVR basis set $|X_n\rangle$ is related to the finite basis set $\phi_n(x)$ through a unitary or orthogonal transformation of Eq.(2.76), it is an equivalent basis set to $\phi_n(x)$ in this N-dimensional vector space. The DVR basis function are highly localized in coordinate space, i.e., $\langle x|X_n\rangle$ is highly peaked near $x = x_n$. Due to this particular local property of the DVR basis, the matrix element of any local operator in the DVR basis is approximately diagonal. For example, the matrix element of the potential energy operator in the DVR basis is approximated by

$$\langle X_m|V(\hat{x})|X_n\rangle = \delta_{mn} V(x_n). \tag{2.80}$$

This result applies to any local operator which is a function of coordinates only, and should be understood in the sense that the coordinate operator is approximated by Eq.(2.78) in the N-dimensional vector space. As the dimension of the vector space increases, the approximation in Eq.(2.80) becomes better and better. Since most potential energy operators are local functions of coordinates, they are diagonal in the DVR representation, and the integration over the coordinates to construct the potential matrix can be eliminated.

In order to obtain localized functions that have some information about the potential energy surface, Clary [38] proposed a potential-optimized discrete variable representation (PODVR) using primitive basis sets of eigenfunctions of convenient one-dimensional reference Hamiltonians, i.e., $H_{ref}\phi_m^{PO} = \epsilon_m \phi_m^{PO}$ and $|X_n^{PO}\rangle = \sum_m |\phi_m^{PO}\rangle D_{mn}^{PO}$. In PODVR, the points are optimized for the potential energy surface, therefore the PODVR could reduce the number of basis function to describe the dynamics system.

2.5.2 Collocation Quadrature Scheme

In order to carry out the TD propagation, we may need to re-express the wavefunction in terms of a different basis set. This involves a coordinate transformation between two different arrangements:

$$\xi_{a,n} = \langle \phi_n | \xi_a \rangle \tag{2.81}$$

where ξ_a and ϕ_n are defined with respect to basis functions of different arrangements(a and b). In the collocation quadrature scheme, we can calculate the integral in Eq.(2.81)

$$\xi_n = \sum_i W_{ni}\xi(q_i) \tag{2.82}$$

where q_i are N prefixed multidimensional points of the Jacobi coordinates defined in the b arrangement and W_{ni} is undetermined weighting matrix. For an atom-diatom system, ϕ_n is the product of translation, vibration and rotation functions and q_i denotes (R_i, r_i, θ_i). The matrix W_{ni} can be obtained by a simple matrix inversion

$$W = \Phi^{-1} \tag{2.83}$$

where the matrix element Φ_{ni} is just the value of ϕ_n at the quadrature point (q_i). This collocation choice of the weighting matrix guarantees that the orthogonality of the overlap integral is strictly preserved

$$\langle\phi_n|\phi_m\rangle = \sum_i W_{ni}\Phi_{im} = \delta_{nm} \tag{2.84}$$

and the summation in Eq.(2.82) will be exact if the functions ξ span the N-dimensional vector space of ϕ_n. If the basis functions are not orthogonal, Eq.(2.83) is easily generalized to

$$W = O\Phi^{-1} \tag{2.85}$$

where O is the basis overlap matrix $O_{nm} = \langle\phi_n\phi_m\rangle$. Although the choice of N points can be rather arbitrary as long as the inverse Φ^{-1} exists, it is best to use good quadrature points to minimize the numerical error. For direct products basis functions, a natural choice is DVR points.

Chapter 3

Photodissociation of Formaldehyde

3.1 Introduction

Formaldehyde has been widely studied as the subject of many spectroscopic, photophysical, photochemical, and theoretical investigations.[39, 40, 41, 42, 43, 1, 44, 45, 46, 47, 48, 49, 11, 50, 12, 2, 51, 52, 53, 54, 55, 56, 57, 58, 59, 60, 61, 62, 63, 64, 65, 66, 67, 68, 69, 70, 71, 72, 73, 74, 75] Its small size and well-resolved energy levels make it possible for a complete study of the reaction dynamics via quantum-state specific experimental techniques and advanced theoretical methods and therefore it could present a meeting point for theory and experiment.

The overall formaldehyde photodissociation of interest is characterized by laser excitation of ground state H_2CO (S_0) into a specific rovibrational state on the first electronically excited single surface (S_1), followed by unimolecular dissociation to molecular products H_2+CO or radical products H+HCO. But this simple process belies the complexity of the dynamics. The energy level diagram in Fig.(3.1) shows the three lowest potential energy surfaces. S_1 state does not correlate with the ground state products of either channel, so dissociation at the energies of interest can only occur via a radiationless transition to S_0 or T_1. Therefore, upon excitation to S_1 state, formaldehyde rapidly undergoes internal conversion (IC) to high rovibrational levels on the ground state S_0, or takes intersystem crossing to the triple electronic state T_1. On S_0 state, *ab initio* calculations [74] and experiments [45] indicate that there is a high narrow barrier of around 27720cm^{-1} on the molecular channel and a radical channel threshold inferred from experiments as $30325.8cm^{-1} \pm 0.5cm^{-1}$ [57], which are both within a few kcal/mol of the S_1 state origin. On T_1 state, formaldehyde can dissociate to ground state radicals but over a barrier, which

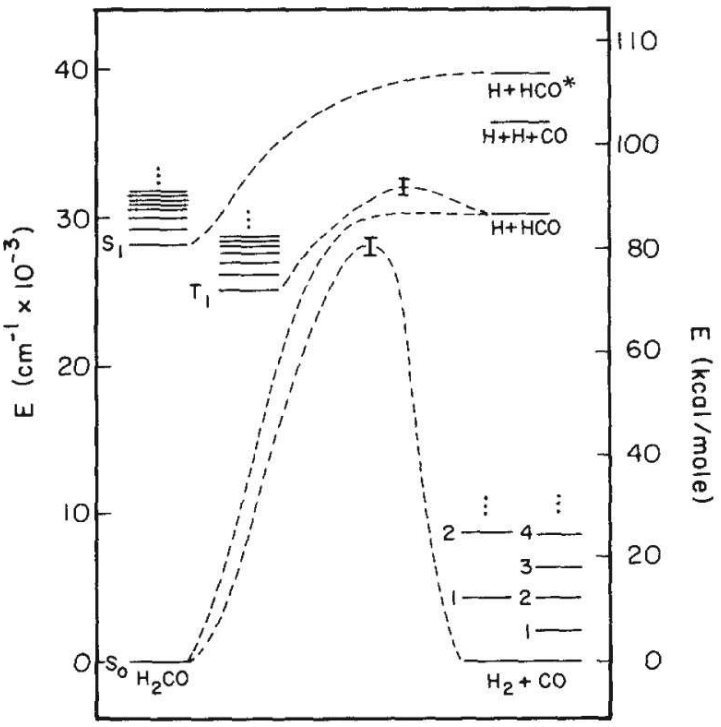

Figure 3.1: Energy level diagram for formaldehyde. The dashed lines show the correlations between bound states and continua. [1]

is 1700∼2700cm^{-1} higher than the radical channel threshold (inferred from experiments) [1]. Therefore, the S_1 state origin, the threshold for radical formation, the barrier for dissociation to molecules on the S_0 surface and possibly that for dissociation to radicals on the T_1 surface are all close in energy, as shown in Fig.(3.1). Thus, the number of available pathways can complicate the photodissociation mechanism [39].

Previous studies [39, 40, 41, 42, 43, 1, 44, 45, 46, 47, 48, 49, 11, 50, 12, 57, 58, 59, 60, 61, 62, 76] have showed that there are at least eight different photophysical and photochemical pathways that could occur after adsorption of a near-UV photon excites H_2CO to S_1 state: fluorescent from S_1 state to S_0 state (Reaction3.2); internal conversion to S_0 (Reaction3.3), and fragmentation on the ground state potential energy surface to products by molecular channel (Reaction3.4), intramolecular hydrogen abstraction channel or roaming atom channel (Reaction3.5), or radical channel (Reaction3.6); isomerization on S_0 state; intersystem crossing to T_1 (Reaction3.8), and

fragmentation on T_1 state to radical products H + HCO (Reaction3.9). Extensive experimental and theoretical studies have been done to study the reaction mechanism and state-to-state dynamics of all these pathways. In the next section we briefly review previous experimental and theoretical results from the two important reaction channels related to our work: molecular channel, and roaming atom channel.

$$H_2CO(S_0, v_0, j_0) + hv \rightarrow H_2CO(S_1, v_1, j_1) \tag{3.1}$$

$$H_2CO(S_1, v_1, j_1) \rightarrow H_2CO(S_0, v_2, j_2) + hv' \tag{3.2}$$

$$H_2CO(S_1, v_1, j_1) \rightarrow H_2CO(S_0, v_3, j_1) \tag{3.3}$$

$$H_2CO(S_0, v_3, j_1) \rightarrow H_2 + CO \tag{3.4}$$

$$H_2CO(S_0, v_3, j_1) \rightarrow H - HCO \rightarrow H_2 + CO \tag{3.5}$$

$$H_2CO(S_0, v_3, j_1) \rightarrow H + HCO \tag{3.6}$$

$$H_2CO(S_0, v_3, j_1) \rightarrow HCOH \tag{3.7}$$

$$H_2CO(S_1, v_1, j_1) \rightarrow H_2CO(T_1, v_4, j_1) \tag{3.8}$$

$$H_2CO(T_1, v_4, j_1) \rightarrow H + HCO \tag{3.9}$$

3.1.1 Molecular Channel

The most extensive experimental and theoretical work has focused on the reaction dynamics for the molecular channel (Reaction3.3 and 3.4) [39, 40, 41, 42, 43, 44, 45, 46, 47, 48, 49, 11, 67, 68, 69, 70, 71, 76, 74]. The transition state for this channel has been very well characterized by high-level *ab initio* calculations to be a skewed structure with both hydrogen atoms on the same side of the CO axis. Moore and co-workers [39, 41, 42, 11, 49] have done pioneering experiments of the molecular products, and found that when formaldehyde was excited to the $2^1 4^1$ transition (one quantum in mode 2, C-O stretch, and one in mode 4, out-of-plane bend) in S_1 state, 1) the CO product is formed rotationally hot, peaking at j_{CO}=42, but vibrationally cold, with around 88% population located at v_{CO}=0 and the rest at v_{CO}=1; 2) the H_2 product distribution peaks at v=1 and j_{H_2}=3-5; 3) most of the available energy($\sim$ 65%) is released in translation part; 4) isotopic substitution from H_2CO to HDCO to D_2CO exhibits an increase in the rotational excitation of the CO fragment (peaks at j_{CO}=42, 49, and 53, respectively); 5) increased angular momentum in the parent molecule widens the CO rotational distributions without significantly shifting the peak maximum.

The reaction dynamics, especially the product state distribution, for the molecular channel

has been studied by trajectory calculations [70, 71, 51]. The first full-dimensional study of this dissociation dynamics was reported by Miller and co-workers [70]. They constructed two PESs based on the extended valence bond approach (EVB) that describe the H_2CO minimum, the molecular TS, and the separated diatomics using limited ab initio data from MP2/DZP and CCSD/TZ2P. Classical trajectory calculations performed on the two PESs (starting at the TS) showed good agreement with experiment for the product vibration/rotation distributions of H_2CO, D_2CO and HDCO. Subsequently Hase and Schlegel and co-workers [71, 72] performed *ab initio* direct dynamics of the photodissociation with the trajectories starting at Hartree-Fock level of theory for the energies and gradients. This pioneering approach, however, was limited by the low level of *ab initio* theory used, which gave a barrier that is roughly 26kcal/mol too high. Even though the results for the H_2 and CO internal state distributions were quite reasonable, the relative translational energy distribution was not in good agreement with experiment, due to the inaccurate barrier. Therefore, based on current dynamical methods, a complete theoretical study of the reaction which allows full comparisons with the experimental results, especially the product state distributions, still demands an accurate global potential energy surface (PES). Recently, a full-dimensional global H_2CO potential energy surface [2] was constructed from thousands of high-level *ab initio* (CCSD(T) and MR-CI with aug-cc-pVTZ basis) energies, which involves the molecular and radical dissociation channels, as well as the cis- and trans-HCOH isomers. Quasiclassical trajectory calculations were performed on this surface with initiating trajectories at the saddle point. The results showed that the CO rotations distribution was Gaussian-like with a peak at j_{CO} around 40-45, which is in agreement with experiment.

3.1.2 Roaming Atom Channel

An alternative route to molecular products on S_0 state is via intramolecular hydrogen abstraction channel, which was firstly reported in 1993 [11]. In this prescient paper, van Zee *et al.* reported rational distribution of CO for a series of states in S_1. They found that CO formed from the dissociation is rotationally hot but, at energies near and above the radical channel threshold, the CO rotational distributions exhibited a small shoulder toward lower rotational levels. They proposed two possible explanations for the appearance of low rotational levels of CO. One explanation was that anharmonic motions in the transition state at higher energies may lead to dissociation from distinct geometries that could reduce exit impact parameters, and hence lower CO rotational excitation. The second possibility was that the low CO rotational shoulder was related to the opening of the radical dissociation channel and thus an alternative pathway to

formation of molecular products via intramolecular hydrogen abstraction.

Very recently, a combined experimental and theoretical investigation of H_2CO dissociation to H_2 and CO at an energy just above the threshold for H+HCO channel (30340.1cm^{-1}) confirmed that the second pathway[50, 55], called the roaming atom channel, is open to yield rotationally cold CO in conjunction with highly vibrationally excited H_2. In this work, high-resolution state-resolved dc slice imaging was used to measure the CO velocity distributions at various rotational states of CO (j=5-45). The results revealed two molecular dissociation pathways with energies near and above the radical channel threshold. The first proceeds through a well-established skewed transition state to produce rotationally excited CO (j_{CO}=40) and vibrationally cold H_2 (v=0-3). The second dissociation pathway yields rotationally cold CO (j=5-15) in conjunction with highly vibrationally excited H2 (v=5-7). Quasiclassical trajectory calculations [51, 52, 53, 55] performed on a global potential energy surface for H_2CO [2] suggested that this second channel represents an intramolecular hydrogen abstraction mechanism: one hydrogen atom explores large regions of the potential energy surface before bonding with the second H atom, avoids the region of the transition state to molecular elimination entirely. QCT calculations also showed that the roaming atom channel increases in relative importance for the molecular products, as the total excess energy increases. However, in QCT calculations there were some high vibrational H_2 distributions produced with excess energies much lower than the threshold for the H+HCO dissociation. One reason is the limitation of the QCT method that the product molecules can be formed with less than zero-point energy. Another possible reason, as Bowman et al. indicated [51], is that a significant number of trajectories became very long-lived and had to be terminated before dissociation occurred.

Previous experimental studies have reported the product state distributions for these two reaction channels on the S_0 state, showing that each channel has its own especial dynamics signature. Quasiclassical trajectory calculations based on the full-dimensional potential energy surface also showed good agreement with experiments. However, there is still much quantum information, such as tunneling, accurate product state distributions, state-to-state dynamics, especially the issue about the total energy for the opening of the roaming atom channel, cannot be obtained from trajectory calculations. In addition, till now there are few quantum dynamics calculations to study this reaction. So there is an urgent need to study formaldehyde photodissociation with accurate quantum dynamics calculations for comparison in order to elucidate the underlying dynamics.

In the last two decades, significant progress has been achieved on the accurate quantum

dynamics study of four-atom reactions [25, 77, 78, 79, 80, 81], arising from the development of the time-dependent wave packet (TDWP) method, advances in constructing potential energy surfaces [24], and the exploitation of increasingly fast computers. Accurate quantum scatting studies have been carried out for a number of important four atom reactions, such as the H_2+OH to H_2O+H, [78, 82] and its isotopically substituted reactions, the HO+CO reaction[83], and the H_2+CN reaction [84]. Total reaction probabilities, cross sections, rate constants, and even final state resolved reaction probabilities have been reported for these reactions for a few initial states. The cumulative reaction probabilities (CRP) $N(E)$ for J=0 have also been calculated for the H_2+OH and $H_2(D_2)$+CN reactions. These studies provide unprecedented quantitative descriptions of these four-atom reactions.

The transition state wave packet method(TSWP) [16, 84] has been developed to efficiently calculate the cumulative reaction probabilities $N(E)$ at all energies desired from a single propagation of each transition state wave packet forward and backward in time. The $N(E)$'s so obtained can then be thermally averaged to produce the thermal rate constant at all desired temperatures.

To study the reaction dynamics for formaldehyde dissociation, we chose transition state wave packet method, but not the initial state selected wave packet method. This is because there is a deep well ($\sim$ 3.8eV) in the region of global minimum and it is very difficult to solve the initial state wave packet with energy as high as the barrier. Moreover, during the dissociation process, H_2CO is first excited to the S_1 state and then takes radiationless conversion to S_0 state, and from this process, it is difficult to determine the initial states but only the energy is easily determined. These initial states should be kinds of vibrational states with energy determined by the excited state on S_1. Thus, transition state wave packet can better simulate this process than the initial state wave packet.

In this work, we applied transition state time-dependent wave packet method to study the reaction dynamics of formaldehyde dissociation based on the full-dimensional global potential energy surface constructed by Zhang and Bowman *et al.*[2]. In chapter two, we have detailed the basis theory about the transition state wave packet method to calculate $N(E)$ and in the following sections, we presented the implementation of this method for the formaldehyde dissociation study and then discussed the results in comparison with experimental and previous QCT ones.

3.2 Theory

3.2.1 Hamiltonian in Jacobi Coordinates

Fig.(3.2) shows the six Jacobi coordinates used for the diatom-diatom system in this study.

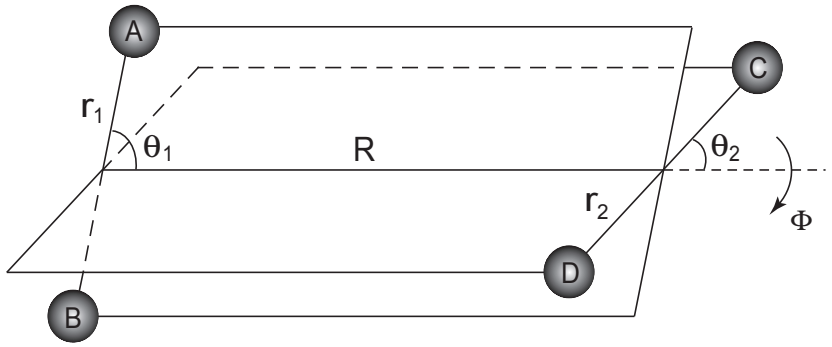

Figure 3.2: The six Jacobi coordinates for diatom-diatom system in the product channel. Here AB refers to H_2 and CD refers to CO.

The Hamiltonian for the diatom-diatom system expressed in these six Jacobi coordinates can be written as,

$$H = -\frac{1}{2\mu_3}\frac{\partial^2}{\partial R^2} + \frac{(\hat{J}-\hat{j}_{12})^2}{2\mu_3 R^2} + \hat{h}_1(r_1) + \hat{h}_2(r_2) + \frac{\hat{j}_1^2}{2\mu_1 r_1^2} + \frac{\hat{j}_2^2}{2\mu_2 r_2^2} + \hat{V}(\mathbf{R}, \mathbf{r}_1, \mathbf{r}_2, \theta_1, \theta_2, \phi) \quad (3.10)$$

where $\mu_i (i = 1-3)$ is the reduced mass for H_2, CO and the system, $\hat{J}$ the total angular momentum operator, and $\hat{j}_1$ and $\hat{j}_2$ the rotational angular momentum operators of H_2 and CO, which are coupled to form $\hat{j}_{12}$. The reference diatomic vibrational Hamiltonian $\hat{h}_i(r_i)(i = 1, 2)$ is defined as

$$\hat{h}_i(r_i) = -\frac{1}{2\mu_i}\frac{\partial^2}{\partial r_i^2} + \hat{V}_i(r_i), \quad (3.11)$$

whose eigenfunctions and eigenenergies are ϕ_{v_i} and ε_{v_i}, respectively and $\hat{V}_i(r_i)$ is a reference diatomic vibrational potential.

3.2.2 Basis Functions and L-shape Grid Scheme

The TD wavefunction is expanded in terms of the body-fixed(BF) rovibrational eigenfunctions defined in terms of the Jacobi coordinates as:

$$\Psi^{JM\epsilon}(\mathbf{R}, \mathbf{r}_1, \mathbf{r}_2, t) = \sum_{n,v,j,K} F_{nvjK}^{JM\epsilon}(t) u_n^{v_2}(R) \phi_{v_1}(r_1) \phi_{v_2}(r_2) Y_{jK}^{JM\epsilon}(\hat{R}, \hat{r_1}, \hat{r_2}), \quad (3.12)$$

where n is the translational basis label, v denotes (v_1, v_2), j denotes (j_1, j_2, j_{12}), and ϵ is the parity of the system defined as $\epsilon = (-1)^{j_1+j_2+L}$ with L being the orbital angular momentum. The determination of the TD coefficient $F_{nvjK}^{JM\epsilon}(t)$ gives the solution of the TD Schrödinger equation.

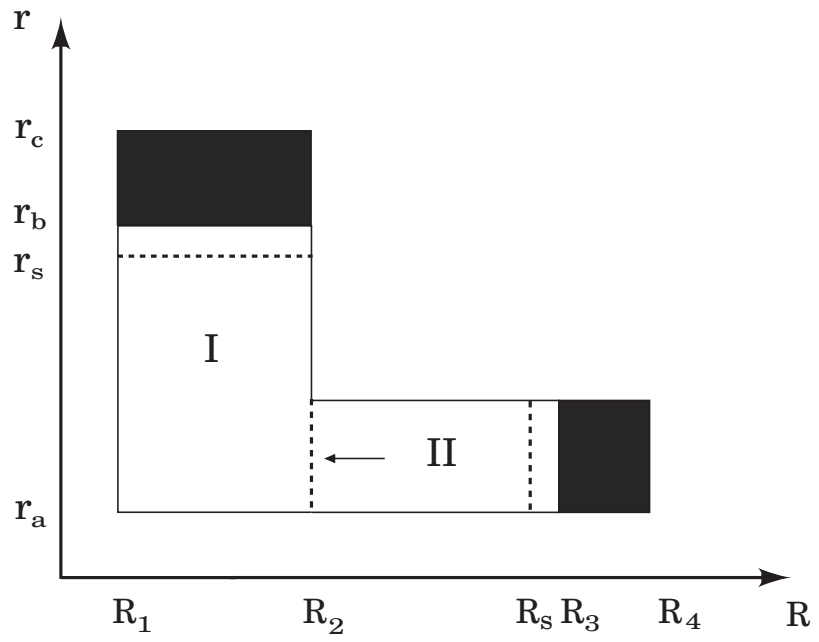

Figure 3.3: A schematic figure of the configuration space for diatom-diatom reactive scattering. R is the radical coordinate between the center of mass of H_2 and CO, and r is the vibrational coordinate of the diatom H_2. Region I refers to the interaction region and II refers to the asymptotic region. Shaded regions represent absorbing potentials. The two reation fluxs are evaluated at the surface defined by $R = R_s$ and $r = r_s$.

Since in the interaction region, the H_2 diatom is highly excited to break the H-H bond and form two C-H bonds, much more vibrational states are needed to describe the reaction dynamics than that in asymptotic region, i.e., the minimum number of vibrational states in the asymptotic region can be smaller than that in the interaction region. Therefore, in order to save computational cost, we can separate the interaction region from the asymptotic region. A simple way to implement this is to use nondirect product basis functions and define normalized translational basis functions as,

$$u_n^{v_1}(R) = \begin{cases} \sqrt{\frac{2}{R_4-R_1}} \sin \frac{n\pi(R-R_1)}{R_4-R_1}, & v_1 \leq v_{asy}, \\ \sqrt{\frac{2}{R_2-R_1}} \sin \frac{n\pi(R-R_1)}{R_2-R_1}, & v_1 > v_{asy}, \end{cases} \tag{3.13}$$

where R_2 and R_4 respectively define the interaction and asymptotic grid(shown in Fig.3.3), and v_{asy} is chosen to be the number of energetically open vibrational channels plus a few closed vibrational channels of the reactive H_2 diatom. The use of a nondirect product basis makes it simple to separate the asymptotic region from the interaction region, and thus a substantial amount of computational savings can be realized.

The $Y_{jK}^{JM\epsilon}$ in Eq.(3.12) is the coupled BF total angular momentum eigenfunctns, which are the eigenfunction for J, j_1, j_2, j_{12}, and the parity operator. They are defined as

$$Y_{jK}^{JM\epsilon} = (1+\delta_{K0})^{-1/2}\sqrt{\frac{2J+1}{8\pi}}\left[D_{K,M}^{J}Y_{j_1j_2}^{j_{12}K} + \epsilon(-1)^{j_1+j_2+j_{12}+J}D_{-K,M}^{J}Y_{j_1j_2}^{j_{12}-K}\right], \quad (3.14)$$

where $D_{K,M}^{J}$ is the Wigner rotation matrix, ϵ is the parity of the system, K is the projection of total angular momentum on the body-fixed axis, and $Y_{j_1j_2}^{j_{12}K}$ is the angular momentum eigenfunction of j_{12} defined as

$$Y_{j_1j_2}^{j_{12}K} = \sum_{m_1}\langle j_1 m_1 j_2 K - m_1 | j_{12} K\rangle \times y_{j_1 m_1}(\theta_1, 0) y_{j_2 K-m_1}(\theta_2, \phi) \quad (3.15)$$

and y_{jm} are spherical harmonics. Note Eq.(3.14) the restriction $\epsilon(-1)^{j_1+j_2+j_{12}+J} = 1$ for $K = 0$.

The interaction potential matrix in the angular momentum basis $Y_{jK}^{JM\epsilon}$ is diagonal in K block and for any fixed (R, r_1, r_2) it can be calculated by,

$$\begin{aligned}
&\langle Y_{jK}^{JM\epsilon}|V(R,r_1,r_2,\theta_1,\theta_2,\phi)|Y_{j'K'}^{JM\epsilon}\rangle \quad (3.16)\\
&= 2\pi\delta_{KK'}\langle Y_{j_1j_2}^{j_{12}K}|V|Y_{j_1'j_2'}^{j_{12}'K}\rangle\\
&= \delta_{KK'}\sum_{m_1,m_1'}\langle j_1 m_1 j_2 K - m_1|j_{12}K\rangle\langle j_1' m_1' j_2' K - m_1'|j_{12}' K\rangle\\
&\times\int_0^\pi \sin\theta_1 d\theta_1\int_0^\pi \sin\theta_2 d\theta_2 P_{j_1m_1}(\theta_1)P_{j_2K-m_1}(\theta_2)\\
&\times V^{m_1,m_1'}(R,r_1,r_2,\theta_1,\theta_2)P_{j_1'm_1'}(\theta_1)P_{j_2'K-m_1'}(\theta_2)
\end{aligned}$$

where

$$V^{m_1,m_1'}(R,r_1,r_2,\theta_1,\theta_2) = \frac{1}{\pi}\int_0^\pi d\phi\cos[(m_1-m_1')\phi]V(R,r_1,r_2,\theta_1,\theta_2,\phi), \quad (3.17)$$

and $P_{jm}(\theta) = \sqrt{2\pi}y_{jm}(\theta,0)$. The centrifugal potential, i.e., the $(J-j_{12})^2$ term in the Hamiltonian shown in Eq.(3.10), which is not diagonalized in the BF representation, is given by

$$\begin{aligned}
&\frac{1}{2\mu R^2}\langle Y_{jK}^{JM\epsilon}|(\hat{J}-\hat{j}_{12})|Y_{j'K'}^{JM\epsilon}\rangle \quad (3.18)\\
&= \frac{1}{2\mu R^2}\delta_{j,j'}\{[J(J+1)+j_{12}(j_{12}+1)-2K^2]\delta_{KK'}\\
&-\lambda_{JK}^{+}\lambda_{j_{12}K}^{+}(1+\delta_{K0})^{1/2}\delta_{K+1,K'} - \lambda_{JK}^{-}\lambda_{j_{12}K}^{-}(1+\delta_{K1})^{1/2}\delta_{K-1,K'}\},
\end{aligned}$$

and the quantity λ is defined as

$$\lambda_{AB}^{\pm} = [A(A+1) - B(B \pm 1)]^{1/2}. \tag{3.19}$$

3.2.3 Propagation of the Wavepacket

The split-operator method is employed to carry out the wave-packet propagation,

$$\Psi^{JM\epsilon}(\mathbf{R}, \mathbf{r}_1, \mathbf{r}_2, t+\Delta) = e^{-\mathrm{i}\hat{H}_0\Delta/2} e^{-\mathrm{i}\hat{U}\Delta} e^{-\mathrm{i}\hat{H}_0\Delta/2} \Psi^{JM\epsilon}(\mathbf{R}, \mathbf{r}_1, \mathbf{r}_2, t), \tag{3.20}$$

where the reference Hamiltonian $\hat{H}_0$ is defined as

$$\hat{H}_0 = -\frac{1}{2\mu_3}\frac{\partial^2}{\partial R^2} + h_1(r_1) + h_2(r_2) \tag{3.21}$$

and the effective potential operator $\hat{U}$ is defined as

$$\hat{U} \quad = \quad \frac{(\hat{J} - \hat{j}_{12})^2}{2\mu_3 R^2} + \frac{\hat{j}_1^2}{2\mu_1 r_1^2} + \frac{\hat{j}_2^2}{2\mu_2 r_2^2} + \hat{V}(\mathbf{r}_1, \mathbf{r}_2, \mathbf{R}). \tag{3.22}$$

The matrix version of Eq.(3.20) for the expansion coefficient vector $\mathbf{F}$ is given by

$$\mathbf{F}(t+\Delta) = e^{-\mathrm{i}\mathbf{H}_0\Delta/2}\mathbf{T}^{\dagger} e^{-\mathrm{i}\mathbf{U}\Delta}\mathbf{T} e^{-\mathrm{i}\mathbf{H}_0\Delta/2}\mathbf{F}(t), \tag{3.23}$$

where $\mathbf{T}$ is the DVR-FBR transformation matrix, and $\mathbf{H}_0$ is the diagonal matrix defined as

$$[\mathbf{H}_0]_{nvjK,n'v'j'K'} = \delta_{nvjK,n'v'j'K'}(\epsilon_n + \epsilon_{v_1} + \epsilon_{v_2}), \tag{3.24}$$

where ϵ_v is defined in Eq.(3.24) and ϵ_n is given by

$$\epsilon_n = \begin{cases} \frac{1}{2\mu_3}(\frac{n\pi}{R_4 - R_1})^2, & v_1 \le v_{asy}, \\ \frac{1}{2\mu_3}(\frac{n\pi}{R_2 - R_1})^2, & v_1 > v_{asy}. \end{cases} \tag{3.25}$$

The effective potential matrix $\mathbf{U}$ is therefore given by

$$\begin{aligned}[U]_{lmnjK,l'm'n'j'K'} &= \delta_{lmn,l'm'n'}\{V_{jK,j'K'}(R_l, r_{1m}, r_{2n}) + \frac{1}{2\mu_3 R_l^2} \\ &\times \langle Y_{jK}^{JM\epsilon}|(\mathbf{J} - \mathbf{j}_{12})^2|Y_{j'K'}^{JM\epsilon}\rangle + [\frac{j_1(j_1+1)}{2\mu_1 r_{1m}^2} + \frac{j_2(j_2+1)}{2\mu_2 r_{2n}^2}]\delta_{jK,j'K'}\},\end{aligned} \tag{3.26}$$

where (R_l, r_{1m}, r_{2n}) is any given DVR points defined with respect to the translational and vibrational basis functions of Eqs.(3.25 and 3.11). To simplify notations, we dropped labels $JM\epsilon$ with the understanding that all equations hold for a given set of these labels.

The exponential operator $e^{-i\hat{U}\Delta}$ is further split into three parts:

$$e^{-\mathrm{i}\hat{U}\Delta} = e^{-\mathrm{i}\hat{K}_{rot}\Delta/2} e^{-\mathrm{i}\hat{V}\Delta} e^{-\mathrm{i}\hat{K}_{rot}\Delta/2} \tag{3.27}$$

as the operator $\hat{K}_{rot}$ is

$$\hat{K}_{rot} = \frac{(\hat{J} - \hat{j}_{12})^2}{2\mu_3 R^2} + \frac{\hat{j}_1^2}{2\mu_1 r_1^2} + \frac{\hat{j}_2^2}{2\mu_2 r_2^2} \tag{3.28}$$

The operation of the matrix **T** on the vector **F** in Eq.(3.23) is defined as follows:

$$[TF]_{lmnjK} = \sum_v C_{n,v_2} B_{m,v_1} \sum_i A_{l,i} F_{ivj} \tag{3.29}$$

where **A**, **B**, and **C** are orthogonal matrices that carry out the transformation between basis and DVR representations, i.e.,

$$\begin{aligned} A_{l,i}^{v_2} &= \langle R_l | u_i^{v_2} \rangle, \\ B_{m,v_1} &= \langle r_{1m} | \phi_{v_1} \rangle, \\ C_{n,v_2} &= \langle r_{2n} | \phi_{v_2} \rangle. \end{aligned} \tag{3.30}$$

3.2.4 Initial Transition State Wavepacket

The initial transition state wavefunction is chosen as the product of the flux operator eigenstate $|+\rangle$ and the eigenstates of the 5D Hamiltonian obtained on the first dividing surface(S_1). In this study, we set the first dividing surface in the transition state region. In order to make S_1 to better separate the product and reactant channel, we firstly transfer the coordinates to the mass-scaled Jacobi coordinates, which are defined as

$$s_{r_i} = \sqrt{\frac{\mu_i}{\mu}} r_i \quad (i = 1, 2) \tag{3.31}$$

$$s_R = \sqrt{\frac{\mu_3}{\mu}} R \tag{3.32}$$

where μ is the mass of the system, $\mu = (\mu_1 \mu_2 \mu_3)^{1/3}$, with μ_i defined in Eq.(3.10). Then we define two new reaction coordinate variables q_1 and q_3 by translating and rotating the s_{r_1} and s_R axes,

$$\begin{pmatrix} q_1 \\ q_3 \end{pmatrix} = \begin{pmatrix} \cos\chi & -\sin\chi \\ \sin\chi & \cos\chi \end{pmatrix} \begin{pmatrix} s_{r_1} - s_{r_1}^0 \\ s_R - s_R^0 \end{pmatrix} \tag{3.33}$$

It can be seen from this equation that we first move the origins of the (s_{r_1}, s_R) coordinates to $(s_{r_1}^0, s_R^0)$, then we rotate these two axes by the angle χ.

The Hamiltonian in Eq.(3.10) can be written in term of q_1, s_{r_2}, and q_3 as

$$H = \frac{1}{2\mu} \left(-\frac{\partial^2}{\partial q_3^2} - \frac{\partial^2}{\partial q_1^2} + \frac{(\hat{J} - \hat{j}_{12})^2}{s_R(q_1, q_3, s_{r_1}^0, s_R^0)^2} + \frac{\hat{j}_1^2}{s_{r_1}(q_1, q_3, s_{r_1}^0, s_R^0)^2} + \frac{\hat{j}_2^2}{s_{r_2}^2} \right) + \hat{V} + \hat{h}_2(s_{r_2}) \tag{3.34}$$

We can choose the dividing surface S_1 at $q_1 = 0$ and calculate the internal transition states for the other five degrees of freedom by solving the eigenstates of the 5D Hamiltonian obtained by setting $q_1 = 0$ in Eq.(3.34), i.e.,

$$H = \frac{1}{2\mu}\left(-\frac{\partial^2}{\partial q_3^2} + \frac{(\hat{J}-\hat{j}_{12})^2}{s_R(q_1=0,q_3,s^0_{r_1},s^0_R)^2} + \frac{\hat{j}_1^2}{s_{r_1}(q_1=0,q_3,s^0_{r_1},s^0_R)^2} + \frac{\hat{j}_2^2}{s^2_{r_2}}\right) + \hat{h}_2(s_{r_2}) + \hat{V} \quad (3.35)$$

The bound states in 5D are calculated using Lancoz method based on the same basis as in the wave packet propagation. After constructing the initial wave packets in $(q_1, s_{r_2}, q_3, \theta_1, \theta_2, \phi)$ coordinates, we transfer them to the $(R, r_1, r_2, \theta_1, \theta_2, \phi)$ coordinates using the collocation quadradure scheme, and propagate them as in the regular wave packet approach.

3.2.5 Absorption Potential

The time-dependent wave function is absorbed at the edges of the grid to avoid boundary reflections. The introduction of an optical potential near the end of the grid is equivalent to simply multiplying the wave function by a decaying function of coordinate near the boundary at the end of each propagation step. Therefore in actual implementation of the absorbing boundary conditions, the wave function is still propagated in the original real potential field, but it is multiplied by a decaying function F_{abs} after each propagation step, that is,

$$\Psi(t+\Delta) \rightarrow F_{abs}\Psi(t+\Delta). \quad (3.36)$$

In the our calculation, we choose F_{abs} as

$$F_{abs} = \begin{cases} exp[-C_{abs}(\frac{x-x_0}{x_{max}-x_0})^{P_{abs}}\Delta], & x_0 < x < x_{max}, \\ 1, & x < x_0 \end{cases} \quad (3.37)$$

where x_0 and x_{max} refer to r_b and r_c for the product arrangement, and R_3 and R_4 for the reactant arrangement.

3.3 Results and Discussions

3.3.1 Numerical Details

As shown in experiments[41], the CO photofragment is formed predominantly in the ground vibrational state $v_{CO} = 0$, thus we could fix R_{CO} to reduce the six dimensions to five dimensions due to the computational cost. The R_{CO} is fixed at 2.154a$_0$ in our study. To determine the transition surface, the values of s_1^0, s_2^0, and χ in Eq.(3.33) are carefully chosen to be $3.26a_0$, $1.35a_0$,

and 60° to minimize the density of states on the dividing surface. The parameters in Fig.3.3 are R_1=0.1 a_0, R_2=8.7 a_0, R_3=10.6 a_0, R_4=14.6 a_0, R_s=9.7a_0, r_a=0.58 a_0, r_b=8.5 a_0, r_c=12.5 a_0, r_s=7.7a_0. A total of 161 sine basis functions spanning $[R_1, R_4]$ are used in the wave-function expansion. In the asymptotic region II, 12 asymptotic H_2 vibrational basis functions are used to expand the wave function while in the interaction region I, 59 pseudo-H_2 vibrational functions are used spanning $[r_a, r_c]$. For the rotational basis, we use j_{1max}=40 for H_2, j_{2max}=70 for CO. For $K = 0$ and $J = 0$, a total of 25361 rotational channels are found to give converged results in the energy range considered. There are even and odd parities for the H_2+CO reaction for total angular momentum $J = 0$ related to the wave function symmetry with respect to torsion angle $\phi = 0$. In this study, we only calculated $K = 0$ and $J = 0$ for a test study and propagated the wave packet for 12000 a.u. with a time increment of Δ=10 a.u. to give a converged $N(\epsilon, J, K, E)$.

3.3.2 Potential Energy Surface

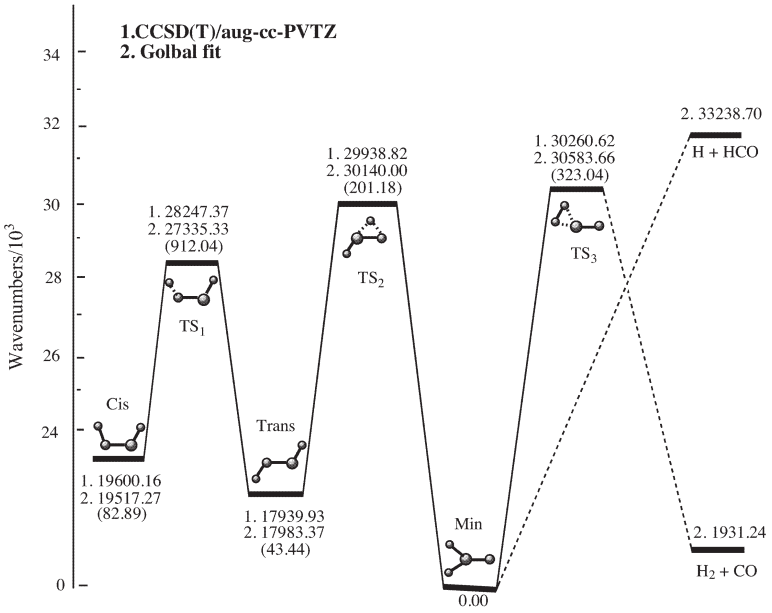

Figure 3.4: The *ab initio* (upper) and fitted (lower) relative energies from the PES constructed by Bowman *et al.*[2] for minima and saddle points in wavenumber. The values in parentheses are the differences.

In this study we used the PES constructed by Bowman *et al.*[2]. Fig.3.4 shows a comparison of the energies of the C_{2v} global minimum, the two isomers(*trans*-HCOH, and *cis*-HCOH), and

the saddle points denoted TS_1 (separating *trans*-HCOH and *cis*-HCOH), TS_2(separating *trans*-HCOH and the global minimum), and TS_3 (separating the global minimum and the molecular products H_2+CO) on this fitted PES and directly from the *ab initio* CCSD(T) calculations. The energies are relative to the global minimum. In order to see the potential energy surface information with R_{CO} fixed, we calculated the bound states in the region of global minimum well and of the asymptotic radical channel with $R_{CO} = 2.154a_0$. We also carried out a normal-mode analysis at the saddle point (TS_3) to approximate its zero point energy. Thus a new set of potential energies and the corresponding ground states could be obtained. The barrier height relative to the global minimum is 4.32eV and the threshold for the radical channel is at 4.57eV.

3.3.3 Dividing Surface S_1

The initial transition state wave packets were calculated on the first dividing surface (S_1). Firstly we show in Fig.3.5 the number of open states for even parity and odd parity as a function of energy (with respect to the global minimum) on the dividing surface S_1. The number of open states increases drastically from the total energy of around 4.3eV. At the total energy of 4.60eV, there are around 270 open states for even parity and around 190 open states for odd parity. These dense open states in this region are due to the low bending frequency of the two heavy atoms C and O and the opening of several pathways on this dividing surface S_1 (molecular channel, roaming atom channel, and radical channel). Also noted that at the total energy of 4.32eV, there are still around 60 open states for even parity and around 30 open states for odd parity on the dividing surface. This is because our dividing surface was taken as perpendicular to the $R - r_1$ plane by a line going through the saddle point of (R_{sad}, r_{1sad}), and due to the dissociation of H_2CO involving the breaking of two bonds(C-H), this dividing surface is not directly perpendicular to the direction of the IRC, but contains two small wells corresponding to the two channels. Fig.3.6 shows the contour plot for the minimum potential energy surface on this dividing surface projected on the two important coordinates, one is q_3 along the dividing line on $R - r_1$ plane and the other one is θ_2 shown in Fig.3.2. The well below is at $\theta_2 \sim 0^\circ$ being on the exit valley to the global minimum(H_2CO), and the well upper is at $\theta_2 \sim 60^\circ$ being on the exit valley to the molecular product channel (H_2+CO). The two wells located along θ_2 indicates that θ_2 is involved in the intrinsic reaction path as well as the other two coordinates R and r_1, which therefore make it difficult to select a dividing surface with less open state number.

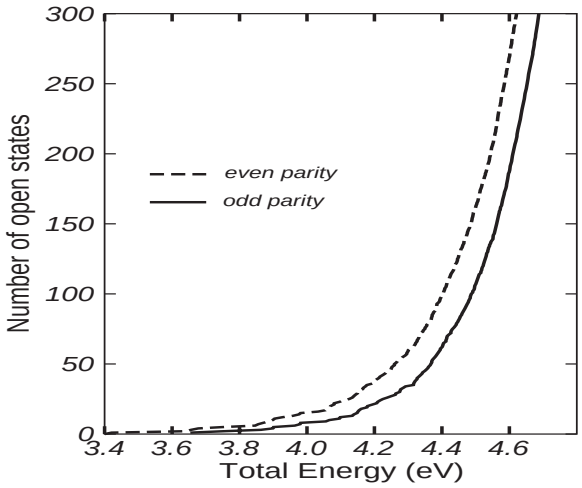

Figure 3.5: Number of open states as a function of total energy on transition state dividing surface in even parity (dashed line) and odd parity (solid line).

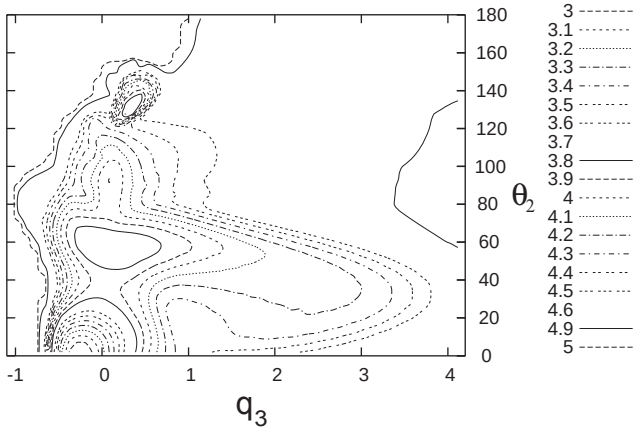

Figure 3.6: The minimum potential energy surface on the dividing surface projected on two coordinates: the coordinate along the dividing line and the θ_2 Jacobi coordinate.

3.3.4 Cumulative Reaction Probability $N(E)$

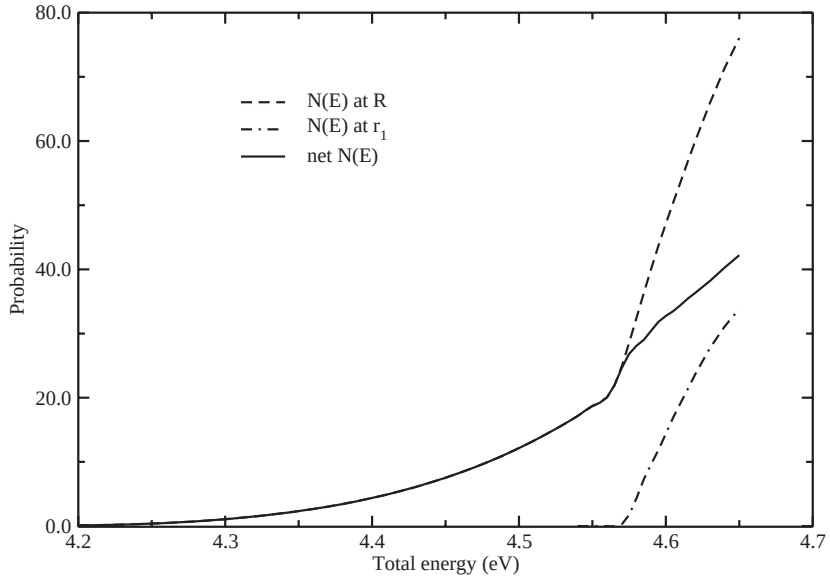

Figure 3.7: The $N(E)$ calculated on the dividing surface S_2 at $R = 10.5a_0$, and on S_3 at $r_1 = 9.0a_0$. The former $N(E)$ refers to the reaction probability to H_2+CO and the later one refers to the reaction probability to radical products H+HCO. The net $N(E)$ refers to the low limitation for the reaction probability from H_2CO to H_2+CO.

The cumulative reaction probabilities $N(J = 0, K = 0, E)$s were calculated on two dividing surfaces $S_2(R = 9.7a_0)$ and $S_3(r_1 = 7.7a_0)$. The former one is located in the asymptotic molecular product region, giving the flux probability to the molecular products H_2+CO on S_2, and the later one is located in the asymptotic radical product region, giving the flux probability to the radical products H+HCO on S_3. Fig.3.7 shows the converged $N(J = 0, K = 0, E)$s on the two dividing surfaces summed over the even and odd parities and all the open transition states with total energy lower than 4.60eV. The total energy is taken respect to the potential energy of the global minimum.

As discussed in the section of PES, the barrier height for molecular channel is 4.32eV and the threshold for radical products is at 4.57eV with respect to the global minimum. The $N(E)$ at S_2 gives a threshold at around 4.25eV and a significant value of 1.44 at the barrier height of 4.32eV,

which indicates tunneling happening for the dissociation from H_2CO to H_2+CO. The $N(E)$ at S_2 first increases slowly and smoothly and when the total energy reaches 4.56eV, $N(E)$ begins to increase remarkably. The $N(E)$ at S_3 gives an expected threshold at around 4.57eV and then increases fast with energy increasing, which indicate the opening of radical channel to H+HCO at 4.57eV. Therefore the sudden increase of $N(E)$ on S_2 from 4.56eV infers the opening of one possible channel: the roaming atom channel to molecular products H_2+CO. In order to clearly see the difference between the two reaction probabilities, we subtract the $N(E)$ at r_1 from the $N(E)$ at R (shown in Fig.3.7). The net $N(E)$ shows two steps as the total energy increases. At first only the molecular channel is open and the probability smoothly increases with total energy increasing. When the energy increases to 4.56eV, the roaming atom channel is open and the probability increases faster due to contribution from this open channel. When the energy increases to 4.57eV, the radical channel is also open. Since H+HCO could react to H_2CO or H_2+CO, it is hard to specific the probability directly from H_2CO to H_2+CO, however, the value should be between the $N(E)$ on S_2 surface and the net $N(E)$. So this probability would increase a bit slower compared to the region of [4.56, 4.57eV]. This is due to the open of the radical channel, which competes with the roaming atom channel and therefore makes the contribution from the roaming atom channel less.

3.3.5 Product State Distribution

Much dynamics information such as the product state distribution has already been widely studied in experiments and qusiclassical trajectory studies. In order to study the quantum dynamics of this reaction and better compare with other experimental and QCT studies, we choose the typical 2+2 Jacobi coordinate to easily obtain the rovibrational states of products and the corresponding translational energies.

Fig.(3.8, 3.9, 3.10) respectively shows H_2 vibrational state v_{HH}, rotational state j_{HH}, and CO rotational state distribution at six total energies of 4.340, 4.440, 4.560, 4.565, 4.570, 4.575eV, summed over parities and all the open initial transition states with total energy lower than 4.60eV at the S_1 dividing surface. From these three figures, we could see that at a total energy much lower than the threshold, such as 4.340eV, the H_2 vibrational state distribution gives a peak at $v_{HH} = 1$ and a range of $[0, 5]$; the H_2 rotational state distribution peaks at $j_{HH} = 2$ and ranges between $[0, 10]$; the CO rotational state distribution peaks at $j_{CO} = 43$ and ranges between $[20, 60]$. With the total energy increases, much more energy is released to the H_2 rotational energy to give a peak at $j_{HH} = 4$ and a broader j_{HH} range of $[0, 15]$, while less energy is released

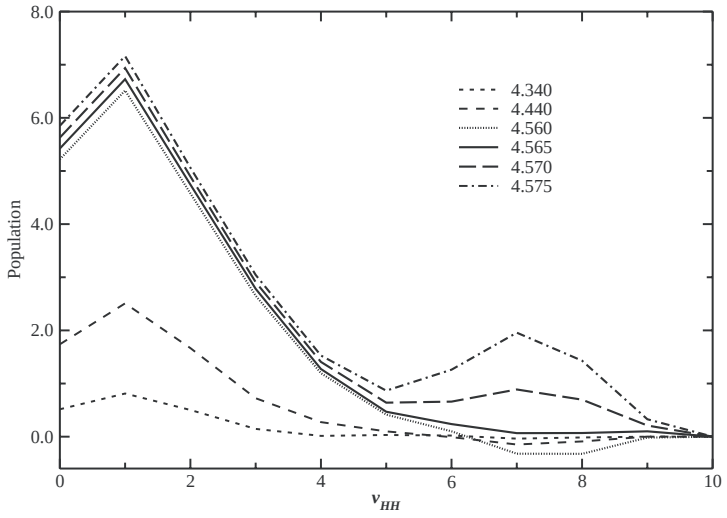

Figure 3.8: H_2 vibrational state distribution at six total energies, summed over H_2 rotational states, CO rotational states, parities for all the open initial transition state with energy lower than 4.60eV.

to the CO rotational energy to give a peak at $j_{CO} = 40$ and much population at low j_{CO} between $[20, 40]$.

It is interesting to see that when the total energy is just near or above the calculated threshold (at 4.565, 4.570, 4.575eV), there is a small population located at higher H_2 vibrational states of $v_{HH} = 5 \sim 9$ peaking at $v_{HH} = 7$ and at lower CO rotational states of $j_{CO} = [0, 20]$. In order to see the correlation among these product states, a contour figure is plotted for the state correlation for j_{CO} and v_{HH} at the total energy of 4.57eV shown in Fig.3.11. It obviously shows the bimodal character for products obtained at the threshold energy: one kind of products with hot CO rotation peaking at $j_{CO} = 43$ and modest H_2 vibration peaking at $v_{HH} = 1$; the other kind of products with rotationally cold CO ranging at $j_{CO} = 0 \sim 15$ and highly vibrationally excited H_2 peaking at $v_{HH} = 7$. These two kinds of product state distributions have already been studied in experiments and quasiclassical trajectory calculations. Our results show good agreement with them, especially with the experiments.

According to previous studies, the two kinds of products are through two different mechanisms: the first mechanism is the molecular channel, *i.e.*, through the well-established transition state and the second one is through an intramolecular hydrogen abstraction, *i.e.*, the roaming atom

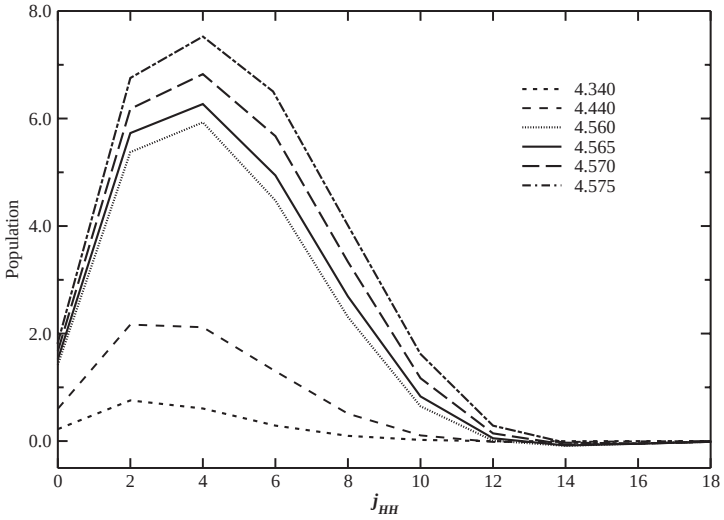

Figure 3.9: H_2 rotational state distribution at six total energies, summed over CO rotational states, H_2 vibrational states, and parities for all the open initial transition state with energy lower than 4.60eV.

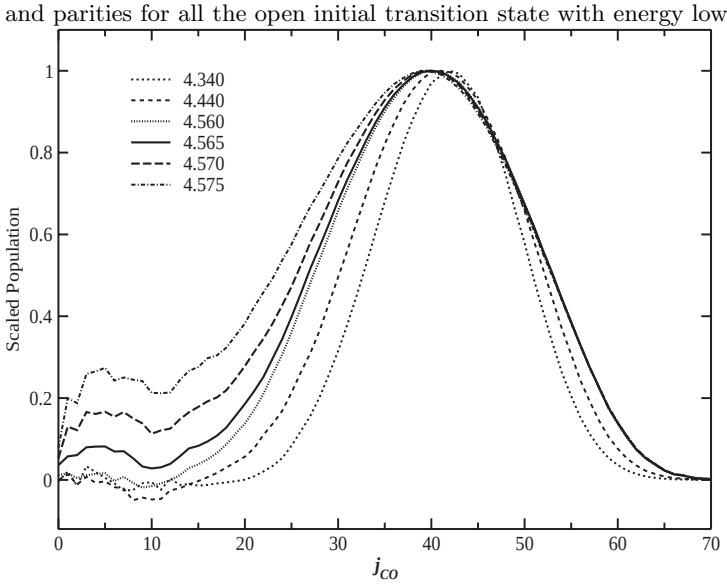

Figure 3.10: CO rotational state distribution at six total energies, summed and normalized over H_2 rovibrational states, and parities for all the open initial transition state with energy lower than 4.60eV.

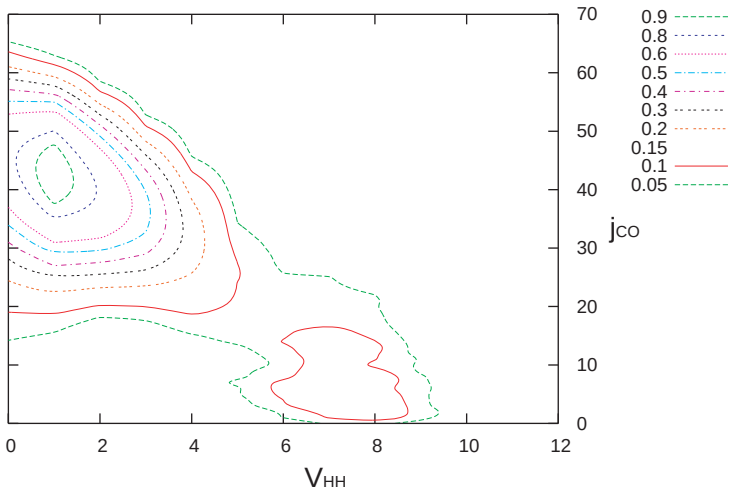

Figure 3.11: State correlations for j_{CO} and v_{HH} summed over H_2 rotational states and parities at the total energy of 4.570eV.

mechanism. Although these mechanisms have already been proved by QCT, in our studies we would choose some special initial transition states on the S_1 dividing surface to see the relation between the product state distribution and the corresponding reaction mechanism. Fig.(3.12, 3.13, 3.14) shown the distribution for v_{H_2}, j_{H_2} and j_{CO} at six total energies of 4.34, 4.44, 4.54, 4.56, 4.57, 4.58eV for a selected initial transition state on S_1 surface. As discussed for Fig.3.6, there are two wells on the dividing surface and this initial state is located in the molecular channel from the global minimum to the well-known transition state. So the product state distribution from this initial state should be produced only by passing the transition state, *i.e.*, the molecular channel mechanism. The obtained results do confirm this assumption: the resulting H_2 vibrational distribution peaks at $v_{HH} = 0 \sim 1$ and ranges between $v_{HH} = [0, 5]$; the CO rotational state distribution is simply Gaussian-shaped, peaking near $j_{CO} = 42 \sim 45$. Even for the total energy higher than the threshold energy(4.57eV), the distribution of v_{HH} and j_{CO} do not show a shoulder distribution at high H_2 vibrational state at $v_{HH} = 5 \sim 9$ and cold CO rotation at $[0, 15]$, which infers that if the reaction takes place through the molecular channel and through the established transition state, the product state distribution is similar to the first kind, even though the total energy is much higher than the threshold energy. This clearly indicates that the first kind of product state distribution is a significant character for the molecular channel.

The second kind of product state distribution was firstly observed following the photolysis on the band of $2^1 6^1$ (30252cm^{-1}), $2^1 4^3$ (30340cm^{-1}), $2^3 4^1$ (31803cm^{-1}) and some other bands with

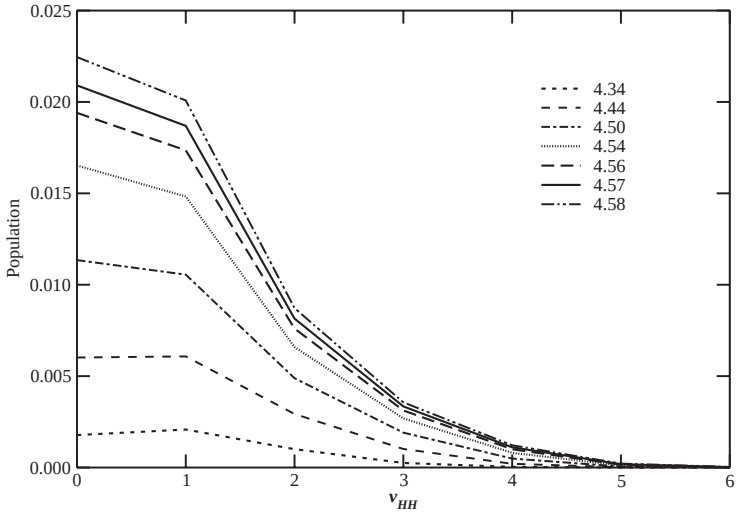

Figure 3.12: H_2 vibrational state distribution for the 19th initial transition state wavepacket at seven total energies.

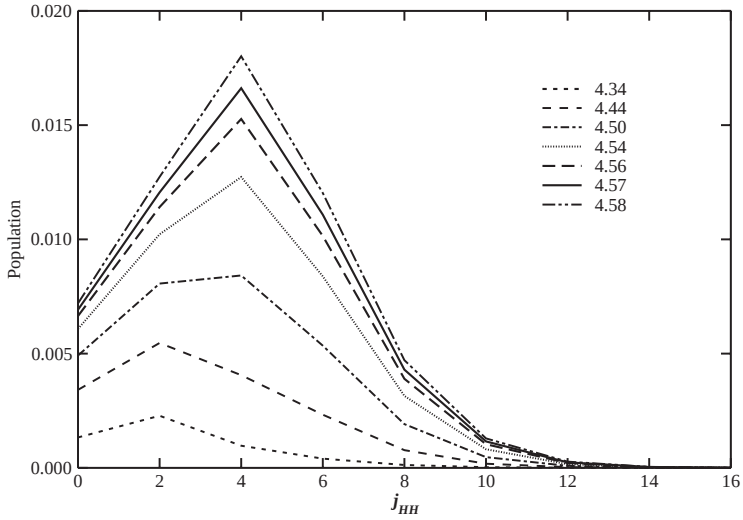

Figure 3.13: H_2 rotational state distribution for the 19th initial transition state wavepacket.

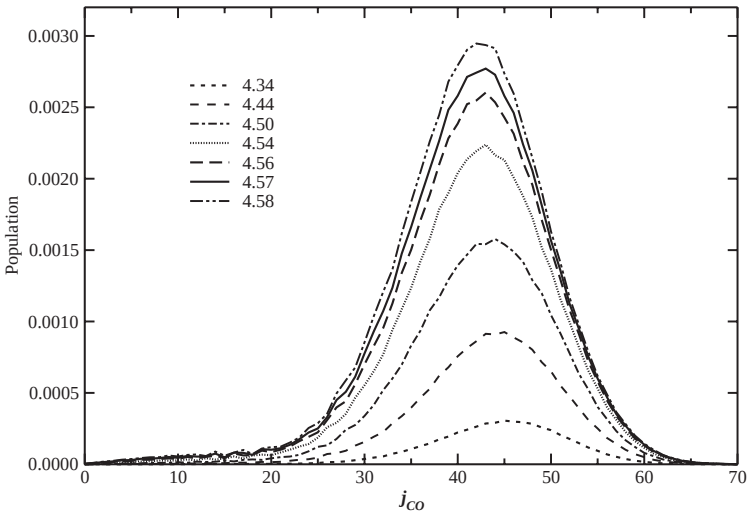

Figure 3.14: CO rotational state distribution for the 19th initial transition state wavepacket.

higher energy. And the threshold to the radical channel is determined to be 30328.5±0.5cm^{-1} from experiments. So this kind of products are produced just near and above the threshold. In our studies, they appears to begin from the total energy of 4.560eV, just near the threshold of 4.57eV, showing good agreement with experimental results. The reaction mechanism was presented by Bowman as an intramolecular hydrogen abstraction mechanism. Examination of the wave packet propagation with time also showed that the wave packet propagated far away from the transition state and by a channel with larger (R, r_1) value. This will be discussed in detail later. Firstly the translational energy distribution is discussed at the total energy just near and above the threshold of radical products.

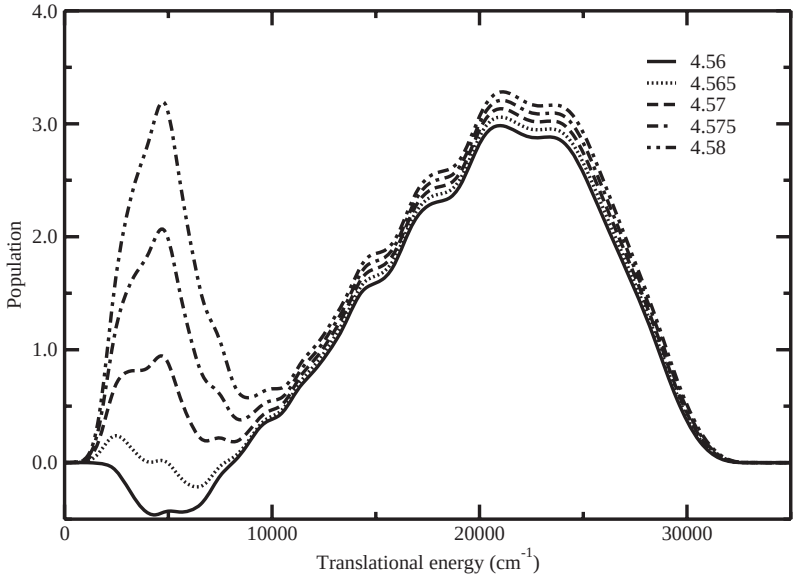

Figure 3.15: Translational energy distribution for the H_2+CO product at the energies indicated (in eV).

Fig.3.15 shows the relative translational energy distribution at six total energies just near and above the threshold energy. As seen these distributions display a bimodal character with the major peak at around 21000cm^{-1} and a minor peak around 4600cm^{-1}. These two peaks are correlated with the bimodal characteristics of the CO rotational distribution shown in Fig.3.10 and the H_2 vibrational distribution shown in Fig.3.8. The high translational energy peak corresponds to hot j_{CO} and low v_{HH}, while the low translational energy distribution corresponds to the the low-j_{CO} shoulder in CO rotational distribution and highly vibrationally excited H_2.

Next we only consider results at the total energy around the threshold of 4.57eV. Fig.(3.16, 3.17, 3.18) show the relative translational energies distributions for the given j_{CO} of 44, 28, and

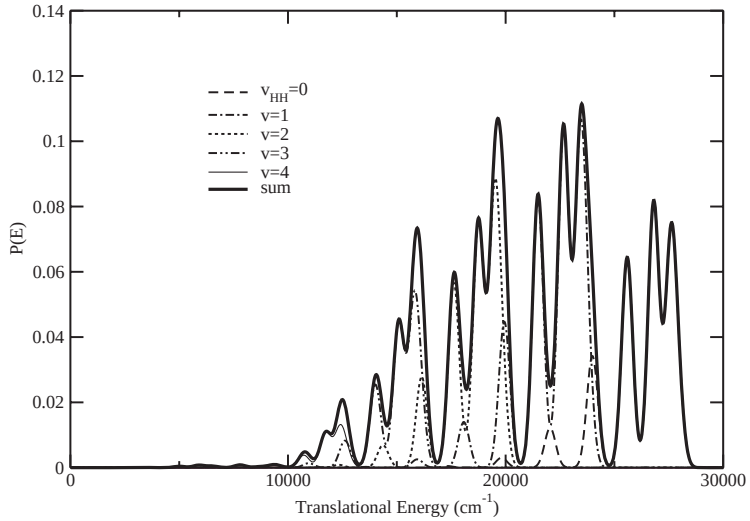

Figure 3.16: Product translational energy distribution at $j_{CO} = 44$ with the total energy of 4.57eV.

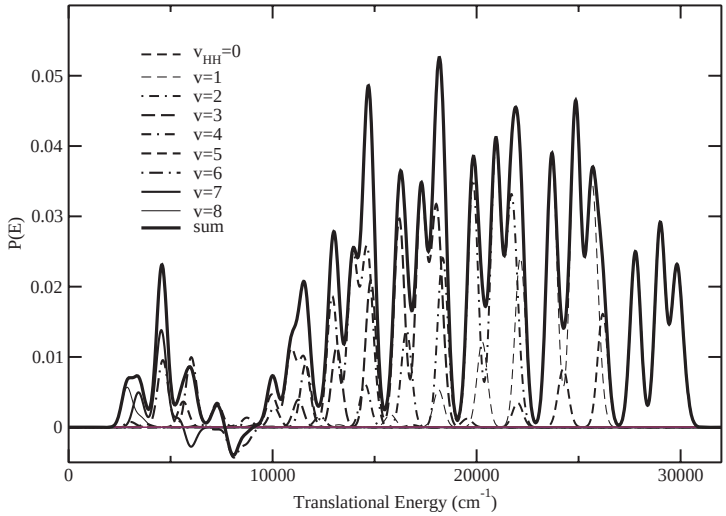

Figure 3.17: Product translational energy distribution at $j_{CO} = 28$ with the total energy of 4.57eV.

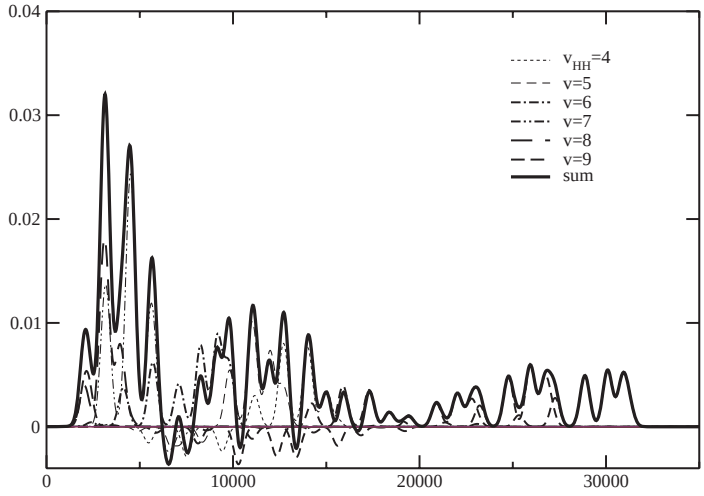

Figure 3.18: Product translational energy distribution at $j_{CO} = 15$ with the total energy of 4.57eV.

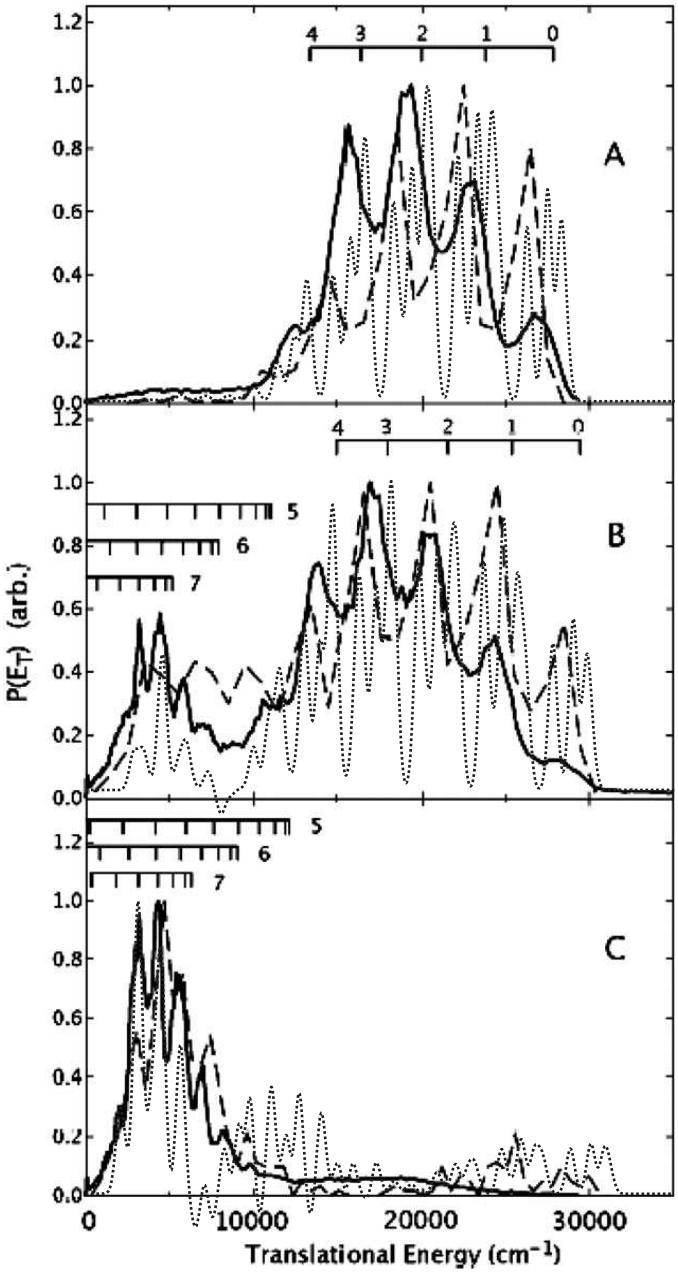

Figure 3.19: Comparison of experimental (solid lines), quasiclassical trajectory (dashed lines), and quantum dynamics (light dotted lines) relative translational energy distributions of the H_2-CO products. Panels A, B, and C correspond to fixed values of j_{CO} of 40, 28, and 15, respectively.

15. It is clear to see that at $j_{CO} = 44$ the distribution yields H_2 fragments with vibrational excitation mainly ranging from $v_{HH} = 0$ to $v_{HH} = 4$. At $j_{CO} = 28$ the bimodal nature of the distribution is evident and at $j_{CO} = 15$ the population is located at highly vibrational levels of H_2. These distributions further provide the correlation between the j_{CO} and v_{HH} and confirm the products from two distinct mechanisms. A detailed comparison with the experimental translational energies distributions for the given j_{CO} is shown in Fig.3.19. As seen, there is very good agreement with experiment and QCT results.

However in our results there are some small negative distributions, which should be unphysical. One possible reason may be the numerical convergence. In the TSWP calculations, we have used some numerical parameters including the six Jacobi coordinates, the parameters in the L-shape grid space, and the vibrational and rotational basis functions for wavefunction expansion. All of these parameters have been tested in our work to give some converged results shown in this thesis. The absorption potential is also important in numerical simulations. Our test calculations showed that the absorption potential used in this work could well absorb the wave function at the edges of the grid and does not cause any boundary reflction within the energy range considered. So the negative distribution should not be caused by the parameters uesd. We noticed that if the starting wave packet is propagated only along the molecular pathway, there is no negative state distributions, which suggests that the negative distribution is a sign of propagation on the PES away from the molecular pathway. Noted that these resulting negative distributions correspond to high H_2 vibrational states at $v_{HH} = 6 \sim 9$ shown in Fig.3.8, high H_2 rotational states at $j_{HH} = 14$ shown in Fig.3.9, low CO rotational states at $j_{CO} = 0 \sim 15$ shown in Fig.3.10, and low translational energies shown in Fig.3.17 and Fig.3.18. We found that these product state distributions just correspond to those from the roaming atom mechanism, which could also provide a proof to the correlation among those product states. We have further investigated these distribution and found that the wave packet propagated backward to the flux surface provides more population than that propagated forward to the flux surface at some especial product states and therefore the net population for this kind of product state seemly gives some negative values. This may infer some small well or unsmoothed surface on potential energy surface. We see that the PES used in our study is constructed by fitting the calculated energies on two different *ab initio* methods, *i.e.*, CCSD(T) and MR-CI, which is connected by some switch functions but also presents a question: whether it is smooth enough for quantum dynamics studies, especially when this switch between these two fits is related to the important region between the molecular channel and roaming atom channel.

3.3.6 Relative Contribution from Different Channels

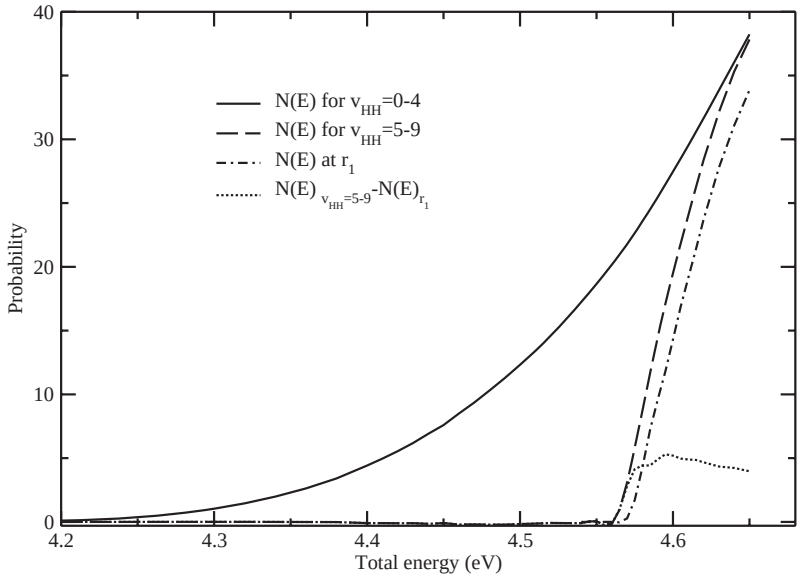

Figure 3.20: Reaction probability for different reaction channels.

Our quantum dynamics results, as well as previous experiments and QCT results, have shown that the dynamical signature of the molecular channel is to produce modest vibrational H_2 and hot rotational CO, while the dynamical signature of the roaming atom channel is to produce highly vibrational H_2 and cold rotational CO. Therefore, we could obtain the reaction probability approximatively for the molecular channel with summing all the population at low H_2 vibrational states of $v_{HH} = 0 \sim 4$ and for the roaming atom channel with summing all the population at high H_2 vibrational states of $v_{HH} = 5 \sim 9$. Fig.3.20 shows the separated reaction probability as function of total energy. The probability for the molecular channel increases as the total energy increases and the curve is very smooth even near the threshold energy, which infers that the open of radical channel may not produce this kind of products. Here, to be mentioned that we used an absorption potential deep in the global minimum well to absorb the trapped wave packet. The probability for the roaming atom channel increases from 4.56eV and above the energy of 4.57eV, this probability includes the reaction both from H_2CO and from H+HCO due to the open radical channel. Similarly, the probability for the radical channel includes two parts: from H+HCO to H_2CO and to H_2+CO. If we plot the difference between these two probabilities, we obtain a very flat curve from 4.57eV shown as the dotted line in Fig.3.20. This curve should not be the probability for the roaming atom channel from H_2CO to H_2+CO, but the difference between this

probability and the probability from H+HCO to H_2CO. So it is difficult to obtain the branching ratio of the different products with energy. However, this problem could be solved if we know the probability for the reaction from H+HCO to H_2CO or H_2+CO with ISSWP approach. In addition, as Bowman *et al.* reported, the radical products increases as the photolysis energy increases. We could predict from the above results that the probability from H_2CO to H_2+CO increases faster by the roaming atom mechanism than by the molecular channel mechanism, *i.e.*, as the excitation energy increases, the roaming atom mechanism begins to play an important role in formaldehyde dissociation to H_2+CO. Recently, Troe[85, 86], Bowman and coworkers[87], and Suits and coworkers[88] have studies the quantum yields from these three channels with total energy higher than the threshold, respectively, from the rates, QCT calculations, and experiments. All of these works were focused on the energy up to 2000cm^{-1} higher than the threshold. In our calculations, it would bring much computational cost for this high total energy range, due to the dense transition states on the dividing surface. However, fortunately we could focus our work just near the threshold, which could also provide some advantages for quantum dynamics calculations over QCT calculations but may need more experiment results for comparisons. Anyway, this issue is still open for both theoretical and experimental work.

3.3.7 Reaction Mechanism

The results shown in Fig.3.11 illustrate the photodissociation leading to molecular products (H_2 and CO) proceeds through two different mechanisms: first, through the well-established skewed transition state yielding vibrationally cold H_2 and rotationally excited CO with large translational energy released. The second mechanism corresponds to the low-j_{CO} shoulder in the CO rotational distribution and the high-v_{HH} shoulder in the H_2 vibrataional distribution. In order to investigate the reaction mechanisms, two initial transition state wave packets are chosen to see how the wave packet propagate on the potential energy surface. Fig.3.21 shows a contour plot for the wave packets propagated for a certain real time, projected on the minimum PES with R and r_1 as coordinates. Fig.3.21(a) clearly indicates the reaction mechanism through the saddle point to produce low vibrational H_2. Fig.3.21(b) shows that there is another pathway far away from the saddle point with larger R and r_1 compared to the saddle point, *i.e.,* the roaming atom mechanism presented by Bowman *et. al.* This channel is open from just near the threshold to the radical channel. To better understand this mechanism, we plotted the corresponding potential energy surface near the radical channel shown in Fig.(3.22). Fig.3.22 shows the energy as a function of the angle $\angle$HoH (o refers to the center mass of HCO) when the distance R

between the the roaming H and o increases, where roaming H is set on the same plane as HCO and the structure of HCO is fixed. This figure shows two reaction pathways near the radical product region: the abstraction of H directly from H_2CO to yield the radical products of H and HCO, *i.e.*, the radical channel; the intramolecular H abstraction with the roaming H facing to the bonded H to yield the molecular products of H_2 and CO, *i.e.*, the intramolecular hydrogen abstraction channel or the roaming atom channel. One way to understand this mechanism is from the dynamics view as talked by Zare[89]. Some of these motions are along the reaction coordinate, that is, they are directed from reactants to products, whereas many other motions do not couple to the reaction coordinate. Energy in these noncoupled modes cannot be used to surmount the barrier that commonly separate reactants from products, and the system must wait some time (the decay time of the resonance) for its energy to redistribute itself and find its way to modes along the reaction coordinate for the collision partners to separate. In the dissociation of formaldehyde, the reaction products are HCO and H as well as CO and H_2. For the H_2+CO channel, the H_2 molecule can be formed directly or can result from the frustrated escape of the H and HCO fragments. In the latter case, the H and HCO partners fail to separate because part of the energy is tied up in vibrational motion of the HCO fragment, which does not couple to the H-HCO coordinate. The loosely bound H atom then bounces around in the attractive potential of the complex until it comes close enough to the H-end of HCO to pull off this H atom, yielding hot vibrationally excited H_2 and cold CO.

3.4 Conclusion

In this study, we reported transition state quantum dynamics calculations for the unimolecular dissociation of formaldehyde on a global potential energy surface[2] and with the nonreacting CO bond length fixed at its value for global minimum. The total cumulative reaction probabilities were calculated on two separate dividing surfaces(S_2 and S_3), respectively, located at the asymptotic regions to two kinds of products, H_2+CO and H+HCO. The comparison of these two $N(E)$s shows two significant steps as the total energy increases, which suggests three reaction channels are involved with total energy lower than 4.60eV, i.e., the molecular channel and the roaming atom channel to produce molecular products of H_2+CO, and the radical channel to radical products of H+HCO. At first with total energy much lower than 4.560eV, formaldehyde dissociates only through the molecular channel to H_2+CO; when the total energy increases to just near 4.560eV, the roaming atom channel opens up; while total energy is above 4.57eV, the

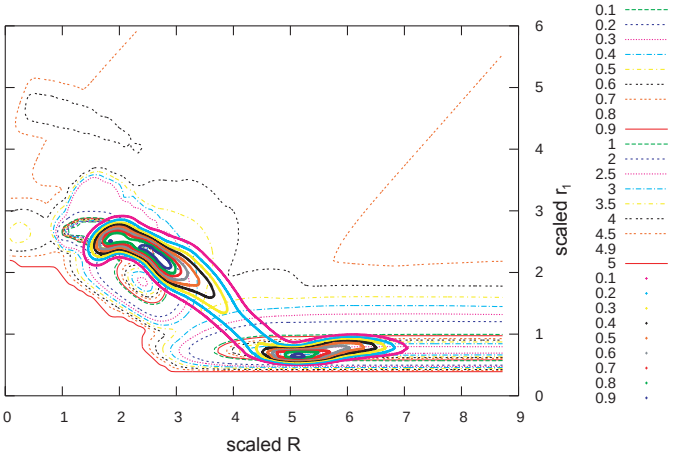

(a)

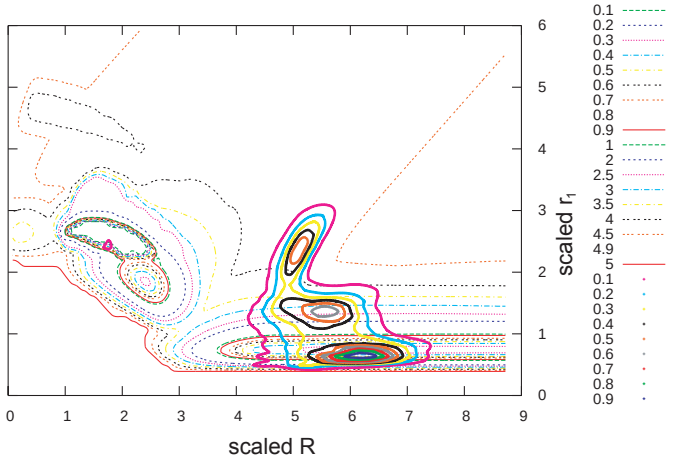

(b)

Figure 3.21: The contour plot for the (a) 19th (b) 200th initial wave packet propagated for a certain real time projected on the minimum potential energy surface.

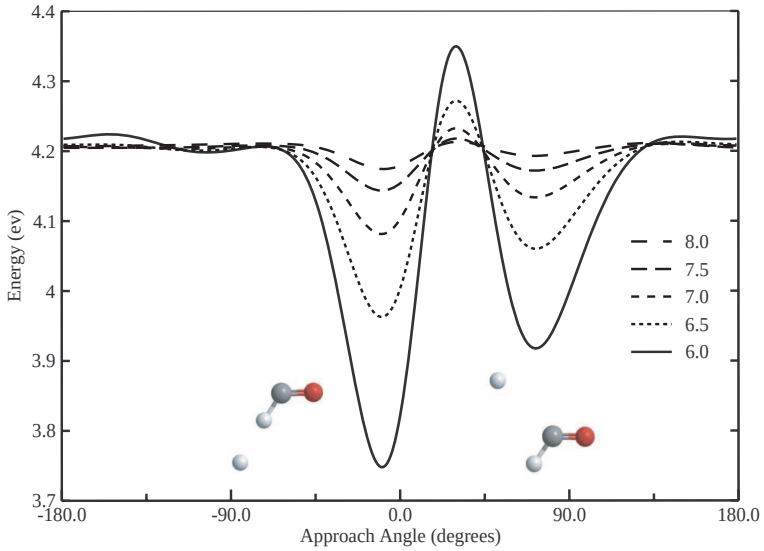

Figure 3.22: The angular dependence of the total energy for a hydrogen atom towards formyl radical.

threshold for the radical channel, formaldehyde also dissociates to radical products of H+HCO.

Both the molecular channel and the roaming atom one produce H_2+CO, however, they show their own dynamics signature on product state distribution. The time-dependent quantum dynamics calculations in this work clearly show that one is to produce modest vibrational H_2 and hot rotational CO with large translational energy released, while the other one is to produce highly vibrational H_2 and cold rotational CO with small translational energy released. The detailed H_2 rotational, H_2 vibrational, CO rotational state distributions given at six total energies not only suggest the state correlations for these two kinds of products, but also confirms that at energies just near and above the threshold of the radical channel(4.57eV), the second pathway, i.e., the roaming atom channel, opens up. These results have shown good agreement with quasiclassical trajectory calculations and experiments, especially the opening of the second kind of products at excitation energy just near and above the threshold to radical channel.

The investigation of time-dependent wave packet propagations also suggests two different reaction mechanisms corresponding to these reaction pathways. The former one is through the well-established skewed transition state and the later one is through a pathway far away from the saddle point, which also confirms the roaming atom mechanism presented by Bowman *et al*[50].

It could be seen that the TSWP approach is very efficient and powerful to calculate $N(E)$ and product state distributions in this work, and the corresponding time-dependent dynamics information provides an alternative way to study reaction mechanism as the classical trajectory study. However, noted that there are some small unphysical negative distributions appearing at the total energy just near the threshold to radical channel. This may be due to the fitting region of two *ab initio* methods on the potential energy surface, where the initial transition state wavepackets are constructed. So this infers a need of a potential energy surface accurate and smooth enough for quantum dynamics calculations. In addition, the quantum calculation for this reduced five-dimensional reaction is still extremely time-consuming due to the dense open states on the first dividing surface within the energy region lower than the threshold of 4.57eV. Kato and co-workers[63] have ever employed normal mode coordinates to define a dividing surface which presents a low density-of-states and only around ten initial wave packets are needed for propagation within the energy region lower than the threshold to radical channel. Even though there is some doubt about using the normal mode coordinates to globally study the dynamics reactions, it infers that an alternative set of coordinates, which could provide a dividing surface with low density-of-states in the transition state region, should be applied to construct initial transition state wavepackets, which could also be transformed to Jacobi coordinates for further propagation, and thus a substantial computational cost can be reduced.

Chapter 4

Polyatomic Reaction Dynamics: $H+CH_4$

4.1 Introduction

In the last chapter, we have presented five dimensional transition state wave packet(TSWP) calculations for four-atom chemical reactions of H_2CO with only the non-reacting CO bond fixed. Recently, more and more researches have focused on quantum reaction dynamics beyond four atoms, i.e, $X+CH_4$ (X=H, F, and Cl), H_2+C_2H, and so on. However, due to the quantum nature of the reactive scattering problem, it is impractical at present to treat polyatomic chemical reactions exactly in full dimension although there has been some progress on this direction[90, 91, 15, 92, 78, 79, 80, 25, 81].

One natural way is to resort to the reduced dimensionality approach to cut down the number of degrees of freedom included in scattering calculations. Clary and co-workers and Nyman and co-workers developed the rotating bond approximation (RBA) and applied it to many important polyatomic reactions by including three to four important degrees of freedom in their calculations[93, 94, 95, 96, 97]. Zhang and co-workers developed the semirigid vibrating rotor target (SVRT) model and implemented it for atom-polyatomic reactions[98, 99, 100, 101, 102]. An alternative way is to use some computational approximation methods to overcome the scaling effort with dimensionality to perform full-dimensionality quantum mechanics calculations, such as, multi-configuration time-dependent Hartree method(MCTDH) [14, 103, 90, 91, 15] and continuous configuration time-dependent self-consistent field(CC-TDSCF) approach[104, 105].

The reaction of hydrogen and methane, $H+CH_4 \rightarrow H_2+CH_3$, is important in combustion chemistry. The reaction is viewed as a prototype of polyatomic reaction and is of significant

interest both experimentally and theoretically[106, 107, 108, 97, 101, 109, 110, 90]. Fundamental knowledge of mechanisms, specific pathways, and rate constants is of key importance to the success of kinetic modelling of this system. The first quantum calculation of this reaction was done in three dimensions(3D)[108], where the system was treated as a collinear four-atom reaction model and the CH_3 group is regarded as a pseudo-diatomic molecule. Yu and Nyman[97] studied this reaction using a four-dimensional(4D) RBU model with the additional freedom of the rotation of CH_3. Both of these time-independent calculations used energy-shifting methods to obtain the thermal rate constant and the agreement between them was generally quite good. However, the calculated rate constants were larger than experiment. Wang and Bowman[109] carried out a six-dimensional study(6D) by treating the three hydrogen atoms in CH_4 as a pseudoatom. Zhang and co-workers[99, 101] studied the same reaction using the SVRT approach in four to five dimensions with an additional umbrella motion considered. The calculated 5D SVRT rate constants was quite in good agreement with experiment, but significantly below the ones obtained from the previous three- and four- degree of freedom reduced dimensionality quantum calculations. A full dimensional quantum study based on the multi-configuration time-dependent Hartree method (MCTDH)[90, 111, 91, 15, 112] was carried out to study the rate constants of this reaction. In this calculation, the cumulative reaction probability was obtained in full dimensionality for total angular momentum J=0, and the thermal rate constants were calculated under the $J-K$ shifting approximation[113]. It was found that the rate constant obtained over the temperature range 200-1000 K agreed with the transition state theory(TST) and the previous three- and four-reduced dimensionality ones, but much higher than the experimental data and the SVRT rate constant.

Some time ago, Palma and Clary[13] proposed an eight-dimensional model to deal with reactions of the type X + YCZ_3 → XY + CZ_3. This is a full dimensional model for the type of reactions under the assumption that the CZ_3 group keeps a C_{3V} symmetry in the reaction. Since the assumption is expected to hold very well in reality, the model is the most realistic one developed so far to calculate the initial state selected reaction probability. Zhang and co-workers[110] successfully implemented the model by using the time-dependent initial state selected wave packet method(ISSWP), and carried out a seven-dimensional (7D) quantum dynamics study for this reaction by fixing the CH bond length in the non-reacting CH_3 group. It was found that the 7D rate constant is much smaller than that obtained by using the 6D atom-triatom model[109], also much smaller than the $J-K$ shifting rate based on a full dimensional (12D) cumulative reaction probability for $J=0$[90, 91]. On the other hand, the 7D rate constant agrees rather well with the

SVRT results[99, 101], in particular with the SVRT5D result[101]. In addition, these calculations also revealed that it was important to include the umbrella motion of CH_3 group in dynamics calculations.

It should be noted that all of the above quantum calculations were done on the same twelve degree of freedom potential energy surface by Jordan and Gilbert[114]. This potential has a C_{3v} transition state with a collinear structure of H-H-C and the center of mass of H_3. However, a significant difference is observed when comparing the results from SVRT and 7D ISSWP models with those from full-dimensional MCTDH model and variational transition state theory(VTST) or TST-related approaches, which show good agreement with each other. Varandas *et al*[115] attribute the huge difference between different theoretical results to the nature of methodologies. Global dynamical methods such as SVRT, ISSWP can produce very different results from the local dynamics methods, such as TST and MCTDH methods which only explore the potential energy surface near the vicinity of the reaction path, but ignore the global topological details of a PES.

In order to further study the difference among those rate constants calculated with different approaches discussed above and experimental data in the temperature range of 200-500 K, and because it becomes possible to study the symmetry stretching motion of CH_3 group in the eight dimensional model[13] with time-dependent quantum dynamics approach, in this work we first calculated the cumulative reactions probability $N(E)$ in 7D and 8D models for $J = 0$ using time-dependent transition state wave packet approach and then employed energy shifting to obtain the thermal rate constants. The results obtained are also compared with previous calculations and experimental data. This chapter is structured as follows. In Section II we present the details of the Hamiltonian and the basis set, followed by the results in Section III. The conclusions are given in Sec. IV.

4.2 Theory

4.2.1 Reaction Rate Constant

The thermal rate constant can be calculated directly, as shown by Miller[7], from the cumulative reaction probability $N(E)$ via ($\hbar$=1)

$$k(T) = \frac{1}{2\pi Q_r(T)} \int_0^\infty dE e^{-E/kT} N(E) \tag{4.1}$$

and

$$N(E) = 2\pi^2 tr[\delta(E-H)F_2\delta(E-H)F_1] \tag{4.2}$$

where $Q_r(T)$ is the partition function of the reactants, H is the full Hamiltonian,

$$F = \frac{1}{2\mu}[\delta(q-q_0)\hat{p}_q + \hat{p}_q\delta(q-q_0)] \tag{4.3}$$

and F_1 and F_2 are the quantum flux operators at dividing surfaces S_1 and S_2 (or S_3) between reactants and products.

The initial wave packets, $|\phi_i^+\rangle$, are constructed at the first dividing surface as $|\phi_i^+\rangle = |\phi_i\rangle|+\rangle$, with $F_1|+\rangle = \lambda|+\rangle$ and $H_{s_1}|\phi_i\rangle = \varepsilon_i|\phi_i\rangle$. The components of the TSWPs at the energy E, $|\psi_i\rangle$, are calculated on the second dividing surface as

$$|\psi_i(E)\rangle = \sqrt{\lambda}\int_{-\infty}^{+\infty} e^{i(E-H)t}\phi_i^+\rangle dt \tag{4.4}$$

Therefore, the CRP $N(E)$ can be computed as

$$N(E) = \sum_i N_i(E) = \sum_i \langle\psi_i|F_2|\psi_i\rangle \tag{4.5}$$

4.2.2 The Coordinate System and the Model Hamiltonian

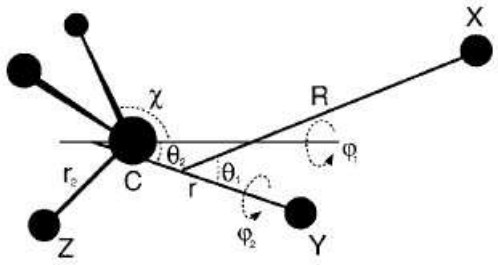

Figure 4.1: The eight-dimensional Jacobi coordinates for the X+YCZ$_3$ system.

Fig. 1 shows the Jacobi coordinate system employed in the present study for the X+YCZ$_3$ → XY + CZ$_3$ reaction. **R** is the vector from the center of mass of YCZ$_3$ to X; **r** is the vector from the center of mass of CZ$_3$ to Y; r_2 is the bond length of CZ; χ is the angle between a CZ bond and the C_{3V} symmetry axis, vector **s**, of CZ$_3$.

To describe the angular coordinates and rotation of the system, it is useful to introduce four frames, namely, space-fixed frame, body-fixed frame (XYCZ$_3$-fixed frame), YCZ$_3$-fixed frame,

and CZ_3-fixed frame. The z-axis of the body-fixed frame lies along the vector **R** and the vector **r** is always in the xz-plane of the frame. The z-axis of the YCZ_3-fixed frame lies along the vector **r** and the vector **s** is always in the xz-plane of the frame. The z-axis of the CZ_3-fixed frame lies along its symmetry axis, vector **s**, and the first Z atom is always in the xz-plane of the frame. The four frames form three pairs of related space and body-fixed frames.

We define the bending angle between vectors **R** and **r** to be θ_1; φ_1 is the azimuth angle of the rotation of YCZ_3 around the vector **r**; θ_2 is the bending angle between vectors **r** and **s**; φ_2 is the azimuth angle of the rotation of CZ_3 around vector **s**.

The 8D model Hamiltonian for the $XYCZ_3$ system is given by[13]

$$\hat{H} = -\frac{1}{2\mu_R}\frac{\partial^2}{\partial R^2} - \frac{1}{2\mu_r}\frac{\partial^2}{\partial r^2} + \frac{(\hat{J}_{tot}-\hat{J})^2}{2\mu_R R^2} + \frac{\hat{l}^2}{2\mu_r r^2} + \hat{K}^{vib}_{\rm CZ} + \hat{K}^{rot}_{\rm CZ} + V(R, r, r_2, \chi, \theta_1, \varphi_1, \theta_2, \varphi_2) \quad (4.6)$$

where μ_R is the reduced mass of the $XYCZ_3$ system and μ_r is the reduced mass of YCZ_3. The first two terms are the kinetic energy operators for **R** and **r**, respectively; $\hat{J}_{tot}$ is the total angular momentum operator of the system; $\hat{J}$ is the rotational angular momentum operator of YCZ_3; and $\hat{l}$ is the orbital angular momentum operator of atom Y with respect to CZ_3. $\hat{K}^{vib}_{CZ}$ and $\hat{K}^{rot}_{CZ}$ are the vibrational and rotational kinetic energy operators of YCZ_3, respectively. No vibration-rotation coupling exists due to the symmetry requirement and the definition of the CZ_3-fixed frame. The two operators have been defined by Palma and Clary as[13],

$$\begin{aligned}
\hat{K}^{vib}_{CZ} &= -\hbar^2\left[\frac{\sin^2\chi}{2\mu_x}+\frac{\cos^2\chi}{2\mu_s}\right]\frac{\partial^2}{\partial r_2^2} - \frac{\hbar^2\cos 2\chi}{2r_2}\left[\frac{1}{\mu_x}-\frac{1}{\mu_s}\right]\frac{\partial}{\partial r_2} - \frac{\hbar^2\sin 2\chi}{2r_2}\left[\frac{1}{\mu_x}-\frac{1}{\mu_s}\right]\frac{\partial^2}{\partial r_2\partial\chi} \\
&+ \frac{3\hbar^2\sin 2\chi}{4r_2^2}\left[\frac{1}{\mu_x}-\frac{1}{\mu_s}\right]\frac{\partial}{\partial\chi} - \frac{\hbar^2}{r_2^2}\left[\frac{\cos^2\chi}{2\mu_x}+\frac{\sin^2\chi}{2\mu_s}\right]\frac{\partial^2}{\partial\chi^2} \\
&- \frac{\hbar^2}{8r_2^2}\left[\frac{3\sin^2\chi-2\cos^2\chi}{\mu_x}+\frac{3\cos^2\chi-2\sin^2\chi}{\mu_s}\right] \qquad (4.7)
\end{aligned}$$

and

$$\hat{K}^{rot}_{\rm CZ} = \frac{1}{2I_A}\hat{j}^2 + (\frac{1}{2I_C}-\frac{1}{2I_A})\hat{j}_z^2 \quad (4.8)$$

where μ_x and μ_s are related to the mass of atoms C and Z, $\mu_x = 3m_z$ and $\mu_s = 3m_cm_z/(m_c + 3m_z)$. I_A and I_C are the rotational inertia of CZ_3, defined as

$$I_A = \frac{3}{2}m_z r_2^2\left(\sin^2\chi + \frac{2m_c}{m_c+3m_z}\cos^2\chi\right) \quad (4.9)$$

and

$$I_C = 3m_z r_2^2\sin^2\chi \quad (4.10)$$

$\hat{j}$ is the rotational angular momentum of CZ_3 and $\hat{J}_z$ is its z-component. The last term $V(R, r, r_2, \chi, \theta_1, \varphi_1, \theta_2, \varphi_2)$ in Eq.(4.6) is the potential energy.

Here if r_2 is fixed at its equilibrium value of 2.067 a.u., the 8D model Hamiltonian above is reduced to 7D one, which was used in the previous 7D calculations[110, 116], and the vibrational kinetic energy operator of YCZ_3, $\hat{K}_{CZ}^{vib}$, is hence simplified as,

$$\hat{K}_{\mathrm{CZ}}^{vib} = -\frac{\hbar^2}{2r_2^2}\left(\frac{\cos^2\chi}{\mu_x} + \frac{\sin^2\chi}{\mu_s}\right)\frac{\partial^2}{\partial\chi^2} - \frac{\hbar^2}{r_2^2}\left[\frac{1}{\mu_s} - \frac{1}{\mu_\chi}\right]\sin\chi\cos\chi\frac{\partial}{\partial\chi} \tag{4.11}$$

4.2.3 Rotational Basis Set for the $XYCZ_3$ System

The rotational basis functions used are similar to those in the initial state wave packet dynamics study of $H+H_2O$[79]. According to the definition of the four frames above, the rotational basis functions for the $XYCZ_3$ system can be written as,

$$\Phi_{Jjlk}^{J_{tot}MK}(\hat{R},\hat{r},\hat{s}) = \bar{D}_{MK}^{J_{tot}}(\hat{R})Y_{jlk}^{JK}(\hat{r},\hat{s}), \tag{4.12}$$

where $\bar{D}_{MK}^{J_{tot}}(\hat{R})$ is defined as

$$\bar{D}_{MK}^{J_{tot}}(\hat{R}) = \sqrt{\frac{2J_{tot}+1}{8\pi^2}}D_{MK}^{*J_{tot}}(\alpha,\beta,\gamma) \tag{4.13}$$

with M and K being the projection of total angular momentum $\hat{J}_{tot}$ on the z-axis of the space-fixed and body-fixed frames, respectively. $\bar{D}_{MK}^{J_{tot}}(\hat{R})$ depend on Euler angles which rotate the space-fixed frame onto the body-fixed frame and are the eigenfunctions of $\hat{J}_{tot}^2$. The spherical harmonics $Y_{jlk}^{JK}(\hat{r},\hat{s})$ are given by

$$Y_{jlk}^{JK}(\hat{r},\hat{s}) = \sum_m \bar{D}_{Km}^{J}(\hat{r})\sqrt{\frac{2l+1}{2J+1}} < jml0|Jm > \bar{D}_{mk}^{j}(\hat{s}) \tag{4.14}$$

where $\bar{D}_{Km}^{J}(\hat{r})$ depend on Euler angles which rotate the XYCZ3 body-fixed frame onto the YCZ_3-fixed frame, and $\bar{D}_{mk}^{j}(\hat{s})$ depend on Euler angles which rotate the YCZ_3-fixed frame onto the CZ_3-fixed frame,

$$\bar{D}_{Km}^{J}(\hat{r}) = \sqrt{\frac{2J+1}{4\pi}}D_{Km}^{*J}(0,\theta_1,\varphi_1), \tag{4.15}$$

$$\bar{D}_{mk}^{j}(\hat{s}) = \sqrt{\frac{2j+1}{4\pi}}D_{mk}^{*j}(0,\theta_2,\varphi_2). \tag{4.16}$$

To explore the space-inversion symmetry of the rotational basis functions given in Eq. 4.12, we can write them in terms of the unitary transformation of the basis function from a space-fixed frame as[79],

$$\Phi_{Jjlk}^{J_{tot}MK}(\hat{R},\hat{r},\hat{s}) = \sum_L \sqrt{\frac{2L+1}{2J_{tot}+1}} < JKL0|J_{tot}K > X_{LJljk}^{J_{tot}M}(\hat{R},\hat{r}',\hat{s}') \tag{4.17}$$

where L is the orbital angular quantum number of atom X with respect to molecule YCZ_3. The space-fixed rotational basis functions $X^{J_{tot}M}_{LJljk}(\hat{R},\hat{r}',\hat{s}')$ are given by

$$X^{J_{Tot}M}_{LJljk}(\hat{R},\hat{r}',\hat{s}') = \sum_{m_J m_L m_j m_l} < Jm_J Lm_L|J_{Tot}M >< jm_j lm_l|Jm_J > Y_{Lm_L}(\hat{R})Y_{lm_l}(\hat{r}')\bar{D}^j_{m_j k}(\hat{s}'), \tag{4.18}$$

where $\hat{R}$, $\hat{r}'$ and $\hat{s}'$ are Euler angles which rotate the $XYCZ_3$-fixed frame, the YCZ_3-fixed frame and the CZ_3-fixed frame onto the space-fixed frame, respectively. The effect of the parity operator, $\hat{\varepsilon}$, is to invert the space-fixed coordinates in the origin: $(\hat{R},\hat{r}',\hat{s}') \rightarrow (-\hat{R},-\hat{r}',-\hat{s}')$. Applying $\hat{\varepsilon}$ to Eq. 4.18, we can easily get

$$\hat{\varepsilon}X^{J_{tot}M}_{LJljk}(\hat{R},\hat{r}',\hat{s}') = X^{J_{tot}M}_{LJljk}(-\hat{R},-\hat{r}',-\hat{s}') = (-1)^{L+l+j+k}X^{J_{tot}M}_{JLjl-k}(\hat{R},\hat{r}',\hat{s}') \tag{4.19}$$

Now, applying $\hat{\varepsilon}$ to Eq. 4.18, we get

$$\begin{aligned}
\hat{\varepsilon}\Phi^{J_{tot}MK}_{Jljk} &= \sum_L \sqrt{\frac{2L+1}{2J_{tot}+1}} < JKL0|J_{tot}K > \hat{\varepsilon}X^{J_{tot}M}_{LJljk}(\hat{R},\hat{r}',\hat{s}') \\
&= \sum_L \sqrt{\frac{2L+1}{2J_{tot}+1}} < JKL0|J_{tot}K > (-1)^{L+l+j+k}X^{J_{tot}M}_{LJlj-k}(\hat{R},\hat{r}',\hat{s}') \\
&= \sum_L \sqrt{\frac{2L+1}{2J_{tot}+1}}(-1)^{J_{tot}+J+l+j+k} < J-KL0|J_{tot}-K > X^{J_{tot}M}_{LJlj-k}(\hat{R},\hat{r}',\hat{s}') \\
&= (-1)^{J_{tot}+J+l+j+k}\Phi^{J_{tot}M-K}_{Jlj-k}
\end{aligned} \tag{4.20}$$

Hence the rotation functions in Eq. 4.12 are not eigenfunctions of the parity operator since $K \rightarrow -K$ and $k \rightarrow -k$. Functions with well defined parity ε can be constructed by taking linear combination of Eq. 4.12,

$$\Phi^{J_{tot}M\bar{K}\varepsilon}_{Jljk}(\hat{R},\hat{r},\hat{s}) = \sqrt{\frac{1}{2(1+\delta_{\bar{K}0}\delta_{k0})}}\left[\Phi^{J_{tot}M\bar{K}}_{Jljk}(\hat{R},\hat{r},\hat{s}) + \varepsilon(-1)^{J_{tot}+J+l+j+k}\Phi^{J_{tot}M-\bar{K}}_{Jlj-k}(\hat{R},\hat{r},\hat{s})\right] \tag{4.21}$$

where $\bar{K} = |K| \geq 0$.

4.2.4 Wavefunction Expansion and Initial Wavefunction Construction

The time-dependent wavefunction is expanded in terms of the parity-adapted rotational basis functions as,

$$\Psi^{J_{tot}M\varepsilon} = \sum_{n,n_r,n_{r_2},n_\chi} \sum_{KJljk} C^{J_{tot}MK\varepsilon}_{nn_rn_{r_2}n_\chi Jljk}(t)G^{n_r}_n(R)F_{n_r}(r)H_{n_{r_2},n_\chi}(r_2,\chi)\Phi^{J_{tot}MK\varepsilon}_{Jljk}(\hat{R},\hat{r},\hat{s}) \tag{4.22}$$

where $C^{J_{tot}MK\varepsilon}_{nn_rn_{r_2}n_\chi Jljk}(t)$ are time-dependent coefficients. n, n_r, n_{r_2} and n_χ are labels for the basis functions in R, r, r_2, and χ, respectively. $G^{n_r}_n$ are sine basis functions for R which are dependent on n_r for their spatial ranges to separate interaction region from asymptotic region[78]. The basis functions $F_{n_r}(r)$ and $H_{n_{r_2},n_\chi}(r_2,\chi)$ are obtained by solving one-dimensional reference Hamiltonian for r and two-dimensional reference Hamiltonian for (r_2, χ), respectively,

$$h_r(r) = -\frac{1}{2\mu_r}\frac{\partial^2}{\partial r^2} + V_r^{\rm ref}(r) \tag{4.23}$$

and

$$h_{r_2,\chi}(\chi) = K^{vib}_{\rm CZ} + V^{\rm ref}_{r_2,\chi}(r_2,\chi) \tag{4.24}$$

where $V_r^{\rm ref}(r)$ and $V^{\rm ref}_{r_2,\chi}(r_2,\chi)$ are the corresponding reference potentials.

The initial wavepacket for the specific state $(J_{tot}, M, \varepsilon)$ of the system is constructed as the direct product of the flux operator eigenfunction and the 7D eigenfunction of the specific state $(J_{tot}, M, \varepsilon)$ for the rest modes on the first dividing surface. In order to choose a proper dividing surface at the transition state region, we define two new coordinates R' and r' by scaling R and r and then rotating by an angle $\gamma = 20°$,

$$\begin{aligned} R' &= \cos\gamma\sqrt[4]{\frac{\mu_R}{\mu_r}}(R-R^\ddagger) + \sin\gamma\sqrt[4]{\frac{\mu_r}{\mu_R}}(r-r^\ddagger) \\ r' &= -\sin\gamma\sqrt[4]{\frac{\mu_R}{\mu_r}}(R-R^\ddagger) + \cos\gamma\sqrt[4]{\frac{\mu_r}{\mu_R}}(r-r^\ddagger). \end{aligned} \tag{4.25}$$

where $R^\ddagger$ and $r^\ddagger$ are the R and r value at the saddle point geometry and thus the dividing surface is located as $r' = 0$ in our calculation. The 7D rovibrational eigenfunction satisfied the following Hamiltonian,

$$\begin{aligned} \hat{H}_{s_1} &= -\frac{1}{2\sqrt{\mu_R\mu_r}}\frac{\partial^2}{\partial R'^2} + \frac{(\hat{J}_{tot}-\hat{J})^2}{2\mu_R R^2_{R',r'=0}} + \frac{\hat{l}^2}{2\mu_r r^2_{R',r'=0}} \\ &+ \hat{K}^{vib}_{\rm CZ} + \hat{K}^{rot}_{\rm CZ} + V(R',r'=0,r_2,\chi,\theta_1,\varphi_1,\theta_2,\varphi_2) \end{aligned} \tag{4.26}$$

The initial wave packets at first are obtained in the coordinate of (R',r') and then are converted to the coordinate of (R, r) via some collocation matrices.

4.2.5 Wavefunction Propagation and Cumulative Reaction Probability Calculation

The wavefunction is propagated using the split-operator propagator,

$$\Psi(t+\Delta) = e^{-iH_0\Delta/2}e^{-iU\Delta}e^{-iH_0\Delta/2}\Psi(t) \tag{4.27}$$

where the reference Hamiltonian H_0 is defined as

$$H_0 = -\frac{1}{2\mu_R}\frac{\partial^2}{\partial R^2} + h_r(r) + h_{r_2,\chi}(r_2,\chi) \tag{4.28}$$

and the reference potential U is defined as

$$U = \frac{(\hat{J}_{tot} - \hat{J})^2}{2\mu_R R^2} + \frac{\hat{l}^2}{2\mu_r r^2} + \hat{K}_{\mathrm{CZ}}^{rot} + V(R, r, r_2, \chi, \theta_1, \varphi_1, \theta_2, \varphi_2) - V_r^{\mathrm{ref}}(r) - V_{r_2,\chi}^{\mathrm{ref}}(r_2, \chi). \tag{4.29}$$

The cumulative reaction probability, $N_i(E)$, for a specific initial wave packet for a whole energy range can be calculated from the time-independent wave function at a second surface $r = r_s$,

$$N_i(E) = \frac{\hbar}{\mu_r}\mathrm{Im}(\langle\psi_{iE}|\psi'_{iE}\rangle)|_{r=r_s} \tag{4.30}$$

where ψ_{iE} and ψ'_{iE} are the time-independent wave function and its first derivative in r. The time-independent wave function ψ_{iE} is constructed by a Fourier transformation of the time-dependent wave packet as,

$$|\psi_{iE}\rangle = \sqrt{\lambda}\int_{-\infty}^{+\infty} e^{i(E-H)t/\hbar}\left|\Psi_i^+(0)\right\rangle dt \tag{4.31}$$

4.3 Results and Discussions

An L-shaped wave function expansion for R and r was used to reduce the size of the basis set[78]. A total number of 60 sine basis functions covering a range from 3.0 to 15.0 Bohr were used for R with 18 grid points in the interaction region; and 6 and 25 basis functions were used for r in the asymptotic and interaction regions, respectively. For the umbrella motion 6 basis functions were used. 3 basis functions were used for the symmetry stretching of CH_3 in 8D calculations to give convergent results within the temperature range considered. In 7D calculations, the bond length of CH was fixed at its equilibrium value of 2.067a.u.. The size of the rotational basis functions is controlled by the parameters, J_{max}=45, l_{max}=27, j_{max}=18 and k_{max}=18, resulting in a total of 32,164 coupled rotational basis function for $J = 0$ with even parity after considering parity and C_{3V} symmetry of the CH_3 group. The vibrational eigenfunctions on the first dividing surface (across the saddle point) were solved using the same basis set above.

As a result of our study we first presented in Fig.(4.2) the plot of cumulative reaction probability as a function of total energy for 7D calculations with CH bond length fixed. The potential energy of H+CH_4 defines the zero of energy in the figure and the corresponding zero point energy of the reactants is 0.42eV. The total cumulative reaction probability shows typical threshold behavior and increases steadily with the increase of total energy in the energy region considered here.

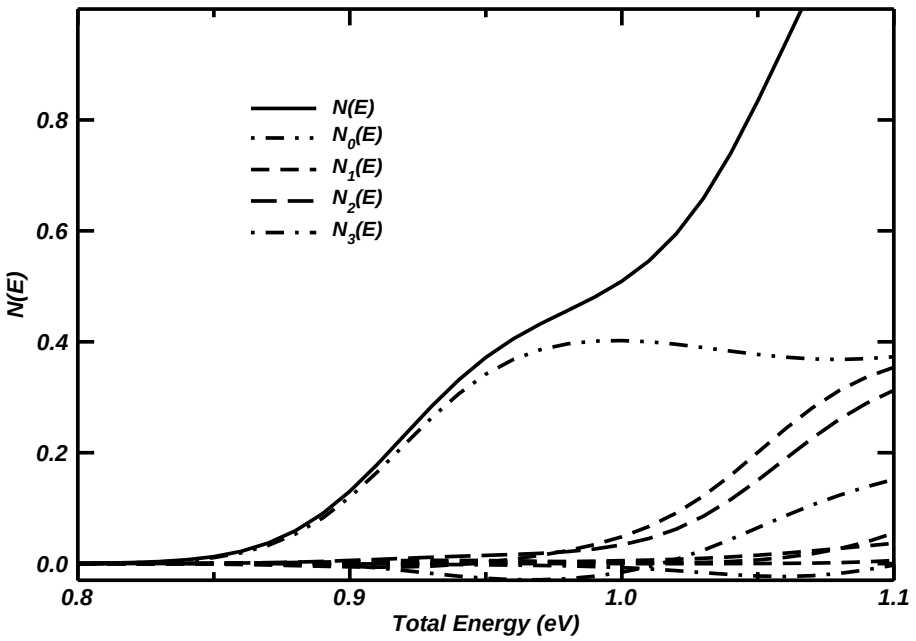

Figure 4.2: 7D total cumulative reaction probability for $J = 0$ and the different initial transition state wave packet contributions as a function of energy.

The threshold is about 0.84eV, while the dynamics barrier at the saddle point is 0.90eV, which suggests the possibility of tunneling. In addition to the cumulative reaction probability, Fig.(4.2) also shows the corresponding contributions of different initial transition state wave packets. As expected, the ground vibrational state yields the dominating contribution within the relevant energy range. Only at higher energies contributions from the several lowest excitation become also relevant. Here, according to previous work[90], besides the ground state, there should be two degenerate excited states significantly contributing to the systems reactivity, which is viewed as the first excitations of the doubly degenerate bending normal mode (v_b) of the transition state. However because only the even H-H-CH_3 bending states occur for a non-rotating CH_5 transition state with C_{3V} symmetry, we show the probability for the v_b=2 state (long dashed line in Fig.4.2) and consider the probability for the v_b=1 state employing an energy shifting approximation. In addition, one feature of the transition state wave packet approach concerns the contributions

mainly from the third and sixth initial transition state wave packets, which display small negative values at some energies. This may be due to the location of the first dividing surface, where the initial wave packets are constructed, and it should cause no real problem as discussed in some previous work[84].

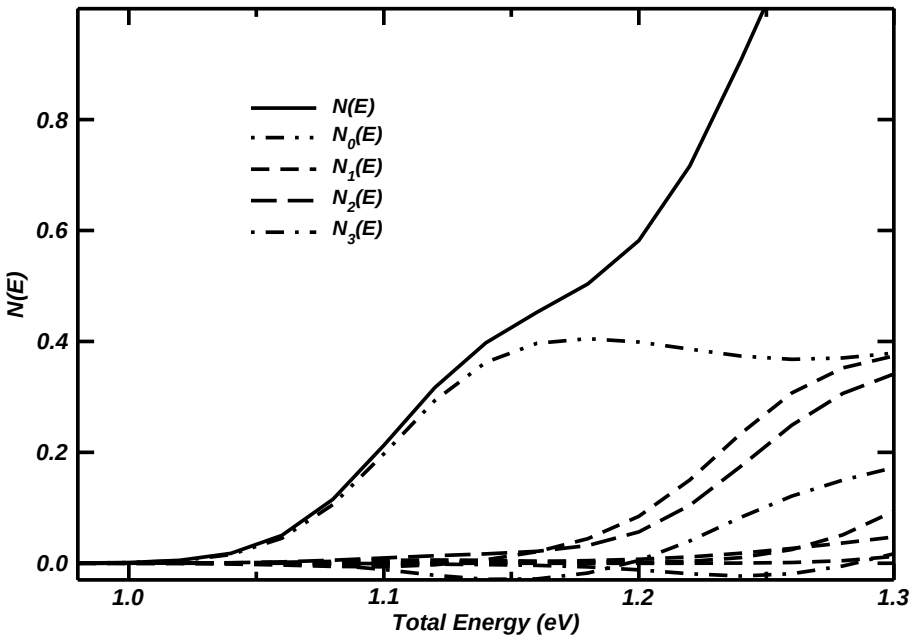

Figure 4.3: 8D cumulative reaction probability for $J = 0$ and the different initial transition state wave packet contributions as a function of energy.

Based on the eight-dimensional model proposed by Palma and Clary, we studied this reaction process with the symmetry stretching motion for CH_3 group considered, i.e., the bond length for CH in CH_3 group. Because the excitation energy for this stretching motion is high (around 2950cm^{-1}) and the temperature range we considered is low from 200 to 500K, most of the wave packets are localized at the ground state for this motion and hence only three basis functions are enough to describe this mode in the whole propagation. The cumulative reaction probability obtained from these 8D calculations is plotted in Fig.(4.3) as a function of total energy. Similar to the 7D results, the potential energy of H+CH_4 defines the zero of energy. With the contribution

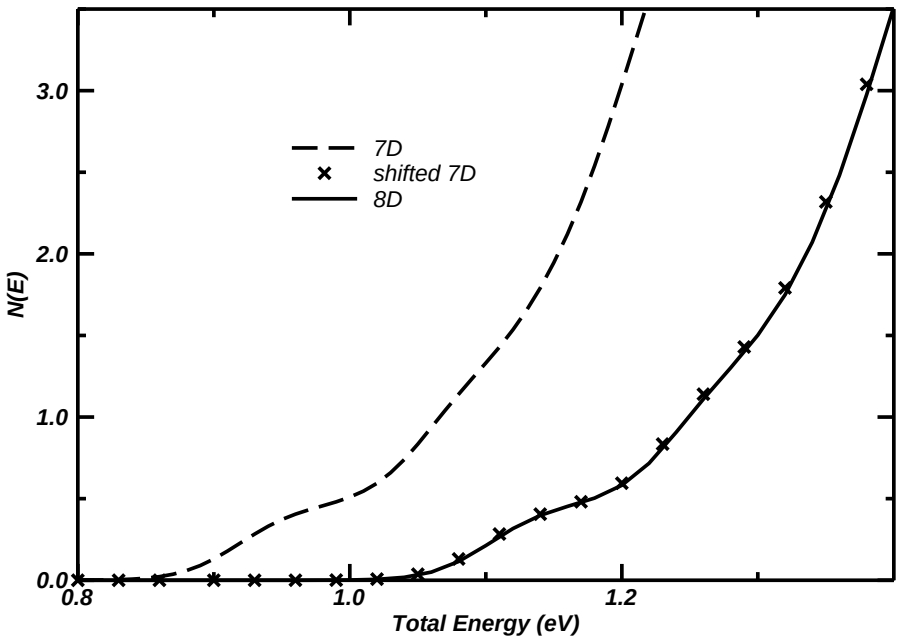

Figure 4.4: Comparison of 7D (solid line) and 8D (dashed line) cumulative reaction probability for $J = 0$ as a function of energy. And a shifted 7D $N(E)$(dotted line) with total energy increased by 0.18eV is also plotted for better comparison.

from the additional symmetry stretching mode considered, the zero point energy of the reactants increased to 0.60eV and the dynamics barrier at the saddle point to 1.08eV, which suggests this stretching motion does not change between the equilibrium CH_4 and the saddle point of CH_5 if comparing to the 7D results. As expected, the threshold of the cumulative reaction probability increases to around 1.02eV. Direct comparison of the $N(E)$ for the eight-dimensional model with the seven-dimensional one shows that the 8D curve is shifted to high energy with respect to the 7D one but it almost has the same shape within the energy range considered.

From the above-mentioned cumulative reaction probabilities for total angular momentum equal zero (J=0) thermal rate constant values were calculated for temperature values between 200 and 500 K employing the J-shifting approximation. The classical rotational partition function with the moments of inertia at the transition state geometry (21430, 54803, and 54803 a.u.) is

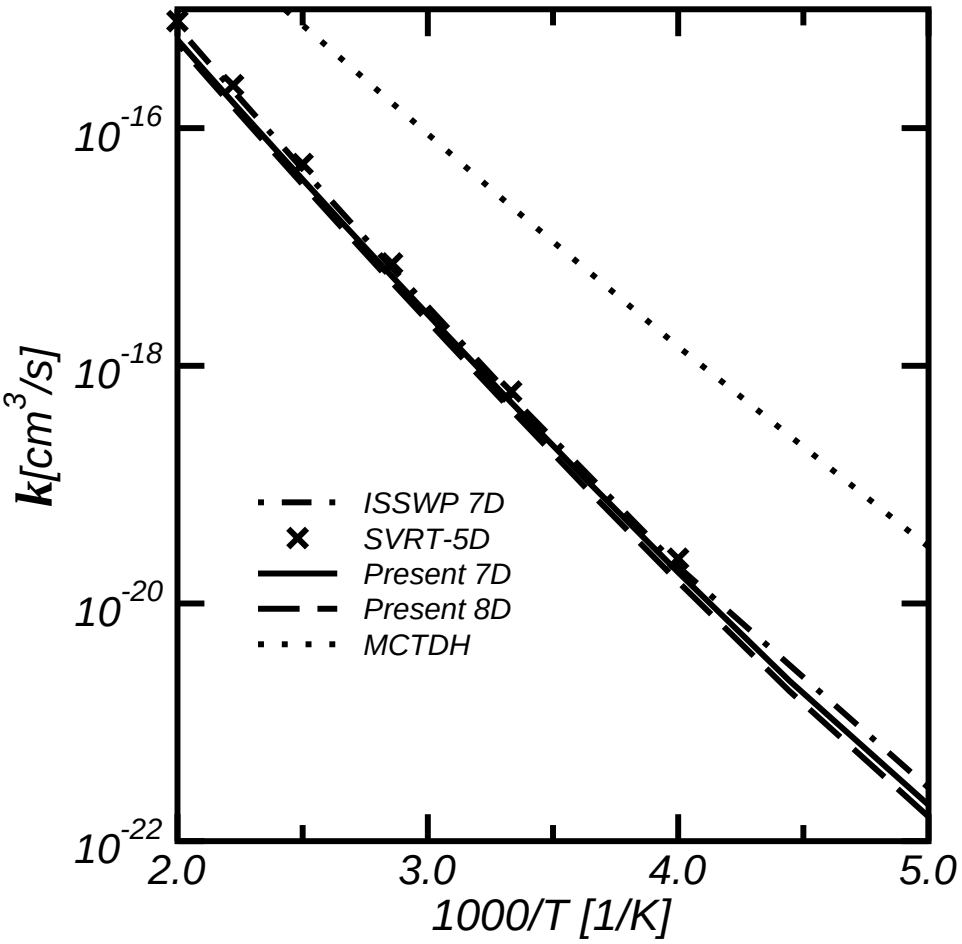

Figure 4.5: Arrhenius plot of the 7D and 8D thermal rate constants, in comparison with the 5D-SVRT and MCTDH rate constants.

used in this calculation. It should be noted that all three moments of inertia at the transition state geometry are quite large. The reactant partition function, which is required in Eq.(4.1), is described as

$$Q_r(T) = Q_{rot,CH_4}(T)Q_{vib,CH_4}(T)Q_{trans,H+CH_4}(T). \tag{4.32}$$

Here $Q_{trans,H+CH_4}(T)$ is the partition function of the relative translational motion of the two reactants. $Q_{rot,CH_4}(T)$ is the rotational partition function of methane and $Q_{vib,CH_4}(T)$ the vibrational partition function. Within the temperature range considered, rotational and vibrational motions of methane can be considered separable and the classical expression for the rotational partition function can be employed. The harmonic approximation for vibrational partition function is used based on the solving of bound states for CH_4. Because only the even CH bending states occur for a non-rotating CH_4 molecule, the excitation energies calculated in this study are 2880 cm^{-1}, 2734 cm^{-1}, 1299 cm^{-1}, and 2947 cm^{-1}, respectively, for the (1000), (0200), (0010), and (0001) states. Here (v_s, v_b, v_u, v_{ss}) denotes the CH_4 state, where v_s, v_b, v_u, and v_{ss} represent, respectively, the stretching excitation of the reactive CH bond, the bending excitation of the reactive CH bond, the umbrella excitation of the CH_3 group, and the symmetry stretching excitation of the CH_3 group. Hence the frequency used for the CH bending motion approximate 1367cm^{-1}. In addition, in the computation of $k(T)$ the $N(E)$ with energies up to 1.2eV for 7D model and 1.4eV for 8D model is considered and also is enough to give converged $k(T)$ within the temperature range of 200-500K. The corresponding Arrhenius plot for $k(T)$ is shown in Fig.4.5 together with previous theoretical and experimental results.

First the rate constants for these 7D and 8D models differ only by 10%-20%, which suggests that the additional mode, i.e., the symmetry stretching motion for the CH_3 group, does not change the dynamics of the process within the temperature range of 200-500K. By comparing the rate constants with a previous result calculated by the same 7D model but with the initial state selected time-dependent wave packet method(ISSWP)[110], one can see a quite good agreement, showing only 20-30% difference. One should note that the 7D ISSWP rate constant was for the ground rovibrational initial state of CH_4. Based on the fact that the vibrational excitation has little effect on the JG PES and the assumption that initial rotational excitations of CH_4 also have little effect on the dynamics, one can approximately treat it as the thermal rate constant. On the other hand, the present study takes into account the effect of CH_4 initial rovibrational excitations, but uses the J-K shifting approximation to yield the thermal rate constant. With the very different approximations employed in these two calculations, the agreement between the present and the ISSWP studies on the rate constant can be considered to be quite good. This

also indicates that the initial rotational excitation of CH_4 does not have any important effect on the reaction dynamics for this reaction on the JG PES. Finally, one can also see that the present TSWP rate constant agrees with the SVRT-5D result quite well.

Now we compare these 7D and 8D rate constants with some earlier results obtained using other approximate methods. The agreement between the present 7D/8D rates and the SVRT-5D result is good. In the temperature region considered here, they differ by 30%. In the SVRT approach to atom-polyatomic reactions, the reacting polyatomic molecule is treated as semi-rigid vibrating rotors whose spatial motion is described exactly. As a result of accurate treatment of the spatial motion, the SVRT model is capable of providing rather accurate results if the geometry of the polyatomic molecule can be properly chosen.

However, the present 7D and 8D rate constants are much smaller by one to two orders of magnitude than those obtained by using the MCTDH method. Since both these two results are obtained with the $J-K$ shifting approximation based on a total cumulative reaction probability for J=0, the huge difference shows its special importance. As the 8D model we used in this study is the most realistic so far for this six-atom reaction with only keeping the CH_3 a C_{3V} symmetry, the results would be reliable if this assumption is kept very well in the low temperature range. Hence one possible reason is that the rest four dimensions not considered in these 8D calculations, i.e., the two asymmetry stretching motions and two asymmetry bending motions for CH_3 group, may play some role to the rate constants. However, according to previous MCTDH calculations[111], the difference between 8D and 12D MCTDH rate constants is less than 70% at low temperature of 200K and even less to 35% at high temperature of 500K. So we cannot attribute the difference between TSWP and MCTDH results only to the dimensionality. Another possible reason may be the nature of methodologies. TSWP or ISSWP, employing Jacobi coordinates for the reaction system, is a kind of global dynamical method, while MCTDH using normal modes explores the potential energy surface near the vicinity of the reaction path, but ignores the global topological details of a PES.

In addition, the accuracy of JG-PES is important for comparison between calculation and experimental results. Recently, Manthe and coworkers have systematically constructed a PES based on *ab initio* calculation at level of CCSD(T)/cc-pVTZ and employed the MCTDH method to calculate the rates, which did give a good result only smaller by a factor of 2-4 comparing with the experimental results but smaller by a factor of two orders of magnitude comparing with the MCTDH results on JG-PES. This huge improvement may be the result of the increased barrier height, because the vibrationally adiabatic barrier heights is 13.4kcal/mol for this *ab initio* PES

but 10.9kcal/mol for the Jordan-Gilbert PES[112]. It also presents an urgent need to calculate the rate constants with TSWP and ISSWP approach on an accurate *ab initio* PES. Recently, a new 8D PES was constructed employing the Grow package[28] based on the *ab initio* calculations at level of CCSD(T) and the time-dependent wave packet calculations using both the TSWP and ISSWP approaches will be reported on this new 8D PES soon.

4.4 Conclusions

A seven- and eight- dimensional transition state wave packet dynamics calculations have been done to study the $H+CH_4 \rightarrow H_2+CH_3$ reaction on the JG-PES. We employed the reduced-dimensional model for the $X+YCZ_3$ type of reaction, originally proposed by Palma and Clary[13], by restricting the CH_3 group under C_{3V} symmetry. In the seven dimensional calculations, the CH bond length in the CH_3 group is fixed at its equilibrium value of 2.067a.u. The remaining seven degrees of freedom were included in this study exactly. In the eight dimensional calculations, all the eight modes were included exactly. For both of these two models, we calculated the cumulative reaction probability at J=0 for the ground state and some vibrationally excited transition states on the dividing surface across the saddle point. Based on the obtained cumulative reaction probabilities for J=0, the rate constants were calculated for temperature values between 200 and 500 K employing the J-shifting approximation. The 7D and 8D results agree perfectly with each other, suggesting the additional mode for the symmetry stretching in CH_3 group does not change in reaction within the temperature range considered here. The results also show quite good agreement with the previous 7D ISSWP rates, the 5D-SVRT rates, and experimental data, but much smaller than the full-dimensional MCTDH results.

Chapter 5

Continuous Configuration Time Dependent Self-Consistent Field Method(CC-TDSCF)

5.1 Introduction

In the last two chapters, we have applied time dependent transition state wavepacket approach (TSWP) to study the four-atomic system (H_2CO) and the reduced seven and eight dimensional system of H+CH_4. It is obvious that during the last two decades with development of various efficient representation schemes[117, 37, 118] and time propagators[30, 32], the time dependent wave packet method has became a dominant computational tool for studying complex chemical dynamics problems with more than three degrees of freedom. It has enjoyed considerable successes on accurate quantum reactive scattering studies of four-atom chemical reactions in full six dimensions[25, 119, 77, 120].

The main advantage of the TD method over the traditional time-independent method is that it scales almost linearly with the number of basis functions. However, due to the quantum nature that number of basis functions grows exponentially with dimensionality, it is only practical at present to deal with seven to eight strongly coupled degrees of freedom[110]. Hence, to study quantum dynamical problems involving many atoms, one has to resort to the reduced dimensionality approach to cut down the number of degrees of freedom included in dynamical studies, or

some computational approximate methods to overcome the scaling of effort with dimensionality.

A promising approach is the time-dependent self-consistent field (TDSCF) method[121, 122, 123, 124, 125, 126, 127, 128, 129, 130]. In the simplest version, i.e. the single configuration time-dependent self-consistent field (SC-TDSCF) approach, the wavefunction of the system is written as a direct product of the wavefunctions for subsystems[121, 122, 123, 124, 126]. A principal drawback of SC-TDSCF is that it replaces exact interaction between subsystems by mean-field coupling, resulting in the lack of correlations between subsystems. One way to account for the important correlations neglected in SC-TDSCF is to add wavefunctions with different configurations to give more flexibility to the wavefunction of the system, resulting in the so-called multiconfiguration time-dependent self-consistent field (MC-TDSCF) method[127, 128, 129, 130, 131]. Wavefunctions with different configurations are usually constructed by imposing orthogonal condition explicitly, making it hard to use more than a few configurations in numerical implementation. Furthermore, the resulting equations for MC-TDSCF are very complicated compared to those in SC-TDSCF method. For these reasons, MC-TDSCF has only been applied to some model problems.

The closely related multiconfiguration time-dependent Hartree method (MCTDH) generalizes MC-TDSCF in a systematic way, thus eliminating the need for choices of the TDSCF states[14, 103]. It has successfully been applied to study various realistic and complex quantum dynamical problems (see Ref. [103] for references). Very recently, it was successfully applied to calculate the $J = 0$ cumulative reaction probability for the six atom H + CH_4 reaction in full 12 dimensions on an *ab initio* potential energy surface (PES), from which the thermal rate constants in a broad temperature region were obtained for the reaction[15]. However, the general application of MCTDH method to strongly correlated systems yields a numerical method wherein the number of possible TDSCF configuration grows exponentially with the number of degrees of freedom, again confining practical use of the method to relatively small systems.

Recently, we proposed a new and efficient scheme for MC-TDSCF, namely, continuous-configuration time-dependent self-consistent field (CC-TDSCF) method[104]. Very often dynamical processes in polyatomic systems can be described as a system of a few strongly coupled degrees of freedom which characterize the process of interest, coupled with clusters of bath modes. Bath modes inside a cluster may be coupled to each other, but the coupling between bath modes in different clusters may be neglected. The basic idea for our new method is to use discrete variable representation (DVR)[37] for the system and then to each DVR point of the system we associate a configuration of wavefunction in terms of direct product wavefunctions for different clusters of

the bath modes. In this way, the correlations between the system and bath modes, as well as the correlations between bath modes in each individual cluster can be described properly, while the correlations between bath modes in different clusters are neglected. Since DVR used for the system are orthogonal, the resulting equations are as simple in structure as those for SC-TDSCF. The dimensionalities of the equations are determined by the number of degrees of freedom in the system and in each individual cluster of bath modes. The method was tested on a model problem of a one-dimensional double well linearly coupled to a harmonic bath[132, 133, 17]. It was found to this model harmonic bath system the CC-TDSCF approach is much more accurate than the traditional SC-TDSCF method, because it allows the bath wave function to change continuously along the system coordinate, in contrast to the SC-TDSCF method which just uses one bath wave function. Our test demonstrated that the CC-TDSCF approach was capable of producing semi-quantitative, or even quantitative results.

In the present work we test CC-TDSCF method on three important complex systems: the H + $CH_4 \rightarrow H_2 + CH_3$ reaction, the hydrogen diffusion on Cu(100) surface, and the double well coupled to a dissipative bath. The H + $CH_4 \rightarrow H_2 + CH_3$ reaction, due to its important roles in CH_4/O_2 combustion chemistry, has been the subject of both experimental and theoretical interest for many years. Because five of the six atoms involved are hydrogens, it is an ideal candidate for high quality *ab initio* quantum chemistry calculations of the potential energy surface and quantum dynamics studies. This reaction has become a benchmark for developing and testing various theoretical methods to accurately study polyatomic chemical reactions[90, 91, 99, 100, 101, 109, 108, 110]. Very recently, Manthe and coworkers constructed a high quality PES for the reaction in the vicinity of the saddle point. The PES can be used to calculate thermal rate constant for the reaction by using flux-flux autocorrelation based methods[15]. The cumulative reaction probabilities for the total angular momentum J=0 were calculated on the PES from which the thermal rate constants for the reaction in a broad range of temperature were obtained. It was found that the theoretical thermal rate constants has an accuracy comparable to or even exceeding experimental precision. In this work we use the PES developed by Manthe and coworkers to test the accuracy of the CC-TDSCF method for the H + CH_4 reaction.

Hydrogen diffusion on metals is a phenomenon of great fundamental and technological importance. Due to the small adsorbate mass, quantum-mechanical tunneling through the classical migration barriers becomes the dominating diffusion mechanism at sufficiently low temperatures. Recently Lauhon and Ho have studied the self diffusion of hydrogen atoms on the Cu(100) surface. Their results reveal a sharp transition from thermally activated diffusion to quantum tunneling

at T=60 K[134]. Various versions of TST approaches, as well as the quantum version of the transition state theory developed by Miller and co-workers[135, 7], have been also developed to study the hydrogen diffusion[136, 137, 138, 139, 16, 140]. However in most studies, the rigid surface model was used, or some *ab initio* calculations were done to provide an optimized potential energy for H on a flexible surface[141], that is, surface modes were neglected in their quantum calculations. Some time ago, Zhang and Light[16] have investigated the role of surface modes in the quantum dynamics of hydrogen diffusion at temperatures in the 120-600K range based on a potential developed by Wonchoba and Truhlar[142] and with the transition state wave packet approach using the flux-flux correlation function formalism for the rate constant. It was found that eight degrees of freedom of the surrounding surface Cu atoms are needed to sufficiently damp the recrossing of the transition state surface in order to converge the correlation expression and determine the rate constant. In this work, we use the same system model and potential energy surface to test the application of the CC-TDSCF method to this high-dimensional system.

The model system of a double well coupled to a dissipative bath is extensively used to study the kinetics of a particle in common condensed phase environments. Generally the conventional description of a reactive event in the condensed phase involves a reaction coordinate, the 'system'. coupled to a large number of harmonic 'bath' degrees of freedom which mimic the effects of the environment. The most important character of this system is the Kramers turnover, i.e., the reaction rate depends nonmonotonically on the friction, increasing at small friction (energy-diffusion-limited regime) and eventually falling off with the friction constant when the latter becomes large enough to ensure Boltzmann equilibrium (spatial diffusion regime). This system has been widely studied with classical mechanical methods, quantum transition state theory, and recently it has been used to test new quantum dynamics methodologies, in particular for those semiclassical theory based methodologies. In this work, we apply the CC-TDSCF and exact TSWP approaches to study the reaction rate for the barrier crossing of a proton based on the flux-flux correlation function calculations.

In the following section we introduce the CC-TDSCF method in a general form. In Sec. III, we then present the results for H+CH_4 with some seven dimensional calculations and ten dimensional calculations by using the approximation CC-TDSCF method, in comparison with the results from exact calculations. In Sec. IV, we report the results for the hydrogen diffusion on Cu(100) surface with CC-TDSCF method. In Sec. V, the results for the double well coupled to a dissipative bath are presented.

5.2 Theory

5.2.1 CC-TDSCF Method

Consider a general multidimensional problem with Hamiltonian written as

$$\hat{H}(\mathbf{s},\mathbf{x}^1,\mathbf{x}^2,...,\mathbf{x}^N) = \hat{h}(\mathbf{s}) + \sum_i^N \hat{h}(\mathbf{x}^i) + \mathbf{V}(\mathbf{s},\mathbf{x}^1,\mathbf{x}^2,...,\mathbf{x}^N), \tag{5.1}$$

where $\mathbf{s}$ and $\mathbf{x}^i$ $(i = 1,...,N)$ are multidimensional vectors, with dimension equal to n_s and n_i, respectively. We call $\mathbf{s}$ as system coordinates, and $\mathbf{x}^i$ as ith cluster of bath coordinates. Hence the total dimension of the problem is $n_s + \sum_i^N n_i$. We partition it into an n_s dimensional system and N clusters of bath modes. In Eq. 5.1, the Hamiltonians for system $\mathbf{s}$ and bath cluster $\mathbf{x}^i$ are given by

$$\hat{h}(\mathbf{s}) = \sum_j^{n_s} \left[\hat{T}(s_j) + V(s_j)\right] = \sum_j^{n_s} \hat{h}(s_j), \tag{5.2}$$

$$\hat{h}(\mathbf{x}^i) = \sum_j^{n_j} \left[\hat{T}(x_j^i) + V(x_j^i)\right] = \sum_j^{n_j} \hat{h}(x_j^i), \tag{5.3}$$

where $\hat{T}$ is the kinetic energy operator, $V(x)$ is the one dimensional reference for coordinate x.

The CC-TDSCF *ansatz* for the total wave function is written as follows[104]

$$\Psi(\mathbf{s},\mathbf{x}^1,\cdots,\mathbf{x}^N,t) = \sum_{\alpha=1}^{M} C_\alpha(t)\,|\mathbf{s}_\alpha\rangle\,\Phi_\alpha(\mathbf{x}^1,\cdots,\mathbf{x}^N,t), \tag{5.4}$$

where $|\mathbf{s}_\alpha\rangle$ denotes DVR points for the system coordinates $\mathbf{s}$ which is constructed via direct product of DVR grids for individual coordinate s_i $(i = 1,...,n_s)$; $\Phi_\alpha(\mathbf{x}^1,\cdots,\mathbf{x}^N,t)$, which depends on the DVR point $|\mathbf{s}_\alpha\rangle$, is written as a product of single-mode functions as in the single configuration TDSCF,

$$\Phi_\alpha(\mathbf{x}^1,\cdots,\mathbf{x}^N,t) = \prod_{i=1}^{N} \phi_\alpha^i(\mathbf{x}^i,t), \tag{5.5}$$

where $\phi_\alpha^i(\mathbf{x}^i,t)$ is the time-dependent wave function for the ith cluster of bath coordinates, $\mathbf{x}^i$, at $|\mathbf{s}_\alpha\rangle$ DVR point for the system coordinates. It has the following the constraints

$$\langle\phi_\alpha^i(t)|\frac{\partial}{\partial t}\phi_\alpha^i(t)\rangle = 0, \quad \text{and} \quad \langle\phi_\alpha^i(0)|\phi_\alpha^i(0)\rangle = 1, \tag{5.6}$$

for $i = 1,2,\cdots,N$. These constraints will guarantee that the single-mode functions are normalized at any time t.

Now we introduce the "single-hole function":

$$\Phi_\alpha^{(i)} = \phi_\alpha^1 \cdots \phi_\alpha^{(i-1)} \phi_\alpha^{(i+1)} \cdots \phi_\alpha^N, \tag{5.7}$$

then Φ_α in Eq. 5.5 can be written as

$$\Phi_\alpha = \phi_\alpha^i \, \Phi_\alpha^{(i)}. \tag{5.8}$$

Employing the Dirac-Frenkel variational principle[143], we can get the equations of motions as[104]

$$i \, \dot{C}_\alpha = \sum_\beta \langle \mathbf{s}_\alpha \Phi_\alpha | \hat{H} | \mathbf{s}_\beta \Phi_\beta \rangle \, C_\beta, \quad \text{for } \alpha = 1, \cdots, M; \tag{5.9}$$

$$i \left[\dot{C}_\alpha \, \phi_\alpha^i + C_\alpha \, \dot{\phi}_\alpha^i \right] = \sum_\beta \langle \mathbf{s}_\alpha \Phi_\alpha^{(i)} | \hat{H} | \mathbf{s}_\beta \Phi_\beta^{(i)} \rangle \left[C_\beta \, \phi_\beta^i \right], \quad \text{for } i = 1, 2, \cdots, N. \tag{5.10}$$

By defining a new function,

$$\varphi_\alpha^i = C_\alpha \, \phi_\alpha^i, \tag{5.11}$$

we can rewrite Eq. 5.10 as

$$i \dot{\varphi}_\alpha^i = \sum_\beta \langle \mathbf{s}_\alpha \Phi_\alpha^{(i)} | \hat{H} | \mathbf{s}_\beta \Phi_\beta^{(i)} \rangle \, \varphi_\beta^i, \quad i = 1, \cdots, N. \tag{5.12}$$

The single-mode function ϕ_α^i can be obtained by multiplying C_α^* on both sides of Eq. 5.11 and resorting the normalization conditions for the single-mode functions,

$$C_\alpha^* \varphi_\alpha^i = |C_\alpha|^2 \, \phi_\alpha^i, \qquad \Longrightarrow \qquad \phi_\alpha^i = \frac{C_\alpha^* \varphi_\alpha^i}{||C_\alpha^* \varphi_\alpha^i||}, \tag{5.13}$$

where $||f|| = \sqrt{\langle f | f \rangle}$ denotes the modulo of a function.

We can see from Eq.5.9 that the evolution of C_i in Eq.5.9 is governed by an effective Hamiltonian arising from averaging the total Hamiltonian over all the bath modes at each DVR point in the system coordinates, while the evolution of wave function for the ith cluster of bath modes is governed by an effective Hamiltonian arising from averaging the total Hamiltonian over all the bath clusters except itself (ith mode) on each DVR point in the system coordinates. Hence to propagate the total wave function, one needs to solve an n_s dimensional equation for the system, and N equations for all the N bath clusters with a dimension equal to $n_s + n_i$ for the ith cluster.

5.2.2 Propagation of CC-TDSCF equations

To propagate CC-TDSCF equations given in Eq. 5.9 and 5.12, one need to calculate the averages of Hamiltonian over wavefunctions. Let us first take a look at the average in Eq. 5.12. Substituting the Hamiltonian given in Eq. 5.1 into the average, we can get

$$\begin{aligned}
&\langle \mathbf{s}_\alpha \Phi_\alpha^{(i)} | \hat{H} | \mathbf{s}_\beta \Phi_\beta^{(i)} \rangle = \langle \mathbf{s}_\alpha \Phi_\alpha^{(i)} \left| \hat{h}(\mathbf{s}) + \sum_k^N \hat{h}(\mathbf{x}^k) + \mathbf{V}(\mathbf{s}, \mathbf{x}^1, \mathbf{x}^2, ..., \mathbf{x}^N) \right| \mathbf{s}_\beta \Phi_\beta^{(i)} \rangle \\
= \;& \langle \mathbf{s}_\alpha | \hat{h}(\mathbf{s}) | \mathbf{s}_\beta \rangle \langle \Phi_\alpha^{(i)} | \Phi_\beta^{(i)} \rangle + \left[\sum_k^N \langle \Phi_\alpha^{(i)} | \hat{h}(\mathbf{x}^k) | \Phi_\alpha^{(i)} \rangle + \langle \Phi_\alpha^{(i)} | \mathbf{V}(\mathbf{s}_\alpha, \mathbf{x}^1, \mathbf{x}^2, ..., \mathbf{x}^N) | \Phi_\alpha^{(i)} \rangle \right] \delta_{\alpha,\beta} \\
= \;& \langle \mathbf{s}_\alpha | \hat{h}(\mathbf{s}) | \mathbf{s}_\beta \rangle \langle \Phi_\alpha^{(i)} | \Phi_\beta^{(i)} \rangle + \left[\hat{h}(\mathbf{x}^i) + \sum_{k \neq i}^N E_\alpha^{eff}(\mathbf{x}^k) + V^{eff}(\mathbf{s}_\alpha, \mathbf{x}^i) \right] \delta_{\alpha,\beta}, \qquad (5.14)
\end{aligned}$$

where

$$E_\alpha^{eff}(\mathbf{x}^k) = \langle \phi_\alpha^k(\mathbf{x}^k, t) | h(\mathbf{x}^k) | \phi_\alpha^k(\mathbf{x}^k, t) \rangle, \qquad (5.15)$$

with $\phi_\alpha^k(\mathbf{x}^k, t)$ given in Eq. 5.5, is the expectation value of Hamiltonian, or, energy for ith bath cluster at $|\mathbf{s}_\alpha\rangle$ DVR point. $V_{eff}(\mathbf{s}_\alpha, \mathbf{x}^i)$ in Eq. 5.14 is the effective potential at system DVR $|\mathbf{s}_\alpha\rangle$ and coordinates for ith bath cluster $\mathbf{x}^i$.

To discuss the first term in Eq. 5.14, we write a system DVR point $|\alpha\rangle$ as $|s_{k\mu}\rangle|\alpha^{(k)}\rangle$, with $|s_{k\mu}\rangle$ denoting the μth DVR point for kth system coordinate, $|\alpha^{(k)}\rangle$ denoting the corresponding DVR points for the other coordinates in the system. For kth system coordinate, we have,

$$\langle s_{k\mu} | \langle \alpha^{(k)} | \hat{h}(s_k) | s_{k\nu} \rangle | \beta^{(k)} \rangle \langle \Phi^{(i)}_{s_{k\mu}\alpha^{(k)}} | \Phi^{(i)}_{s_{k\nu}\beta^{(k)}} \rangle = \langle s_{k\mu} | \hat{h}(s_k) | s_{k\nu} \rangle \langle \Phi^{(i)}_{s_{k\mu}\alpha^{(k)}} | \Phi^{(i)}_{s_{k\nu}\beta^{(k)}} \rangle \delta_{\alpha^{(k)}\beta^{(k)}}. \quad (5.16)$$

Hence $\langle \mathbf{s}_\alpha | \hat{h}(\mathbf{s}) | \mathbf{s}_\beta \rangle \langle \Phi_\alpha^{(i)} | \Phi_\beta^{(i)} \rangle$ matrix is block diagonal for each system coordinate as in ordinary DVR representation. But the matrix for each system coordinate is now time-dependent, in contrast to that in ordinary DVR representation.

Once having matrix elements for $\langle \mathbf{s}_\alpha \Phi_\alpha^{(i)} | \hat{H} | \mathbf{s}_\beta \Phi_\beta^{(i)} \rangle$, it is straightforward to do one more integration with the wave function for ith bath cluster to get

$$\begin{aligned}
&\langle \mathbf{s}_\alpha \Phi_\alpha | \hat{H} | \mathbf{s}_\beta \Phi_\beta \rangle = \langle \phi_\alpha^i | \langle \mathbf{s}_\alpha \Phi_\alpha^{(i)} | \hat{H} | \mathbf{s}_\beta \Phi_\beta^{(i)} \rangle | \phi_\beta^i \rangle \\
= \;& \langle \mathbf{s}_\alpha | \hat{h}(\mathbf{s}) | \mathbf{s}_\beta \rangle \langle \Phi_\alpha | \Phi_\beta \rangle + \left[\sum_k^N E_\alpha^{eff}(\mathbf{x}^k) + V^{eff}(\mathbf{s}_\alpha) \right] \delta_{\alpha,\beta}. \qquad (5.17)
\end{aligned}$$

With matrix elements for $\langle \mathbf{s}_\alpha \Phi_\alpha | \hat{H} | \mathbf{s}_\beta \Phi_\beta \rangle$ and $\langle \mathbf{s}_\alpha \Phi_\alpha^{(i)} | \hat{H} | \mathbf{s}_\beta \Phi_\beta^{(i)} \rangle$ written down, we can propagate the equations of motion for $C_\alpha(t)$ and ϕ_α^i. We use split-operator method to carry out these propagations. Everything is very straightforward, as in ordinary DVR based wave packet

propagation, except that the Hamiltonians involved now are time-dependent. So we have to diagonalize relevant matrices at every step. This may produce a bottleneck for computational speed if the maximum number of DVR points used for one system coordinate becomes large. While in the current applications this number is around 50, so it does not cause any problem to the computation.

5.3 Application to the H + CH_4 System

5.3.1 Theory

The thermal rate constant, $k(T)$, can be calculated from the time integral of a flux-flux autocorrelation function[16, 144, 145]

$$k(T) = Q_r(T)^{-1} \int_{-\infty}^{\infty} dt\, C_{ff}(t), \tag{5.18}$$

where $Q_r(T)$ is the reactant partition function,

$$C_{ff}(t) = \mathrm{tr}[\hat{F} e^{i\hat{H}t_c^*} \hat{F} e^{-i\hat{H}t_c}] = \sum_{n=0} C_{ff}^n(t), \tag{5.19}$$

and $t_c = t - i\beta/2$ with $\beta = (k_B T)^{-1}$. C_{ff}^n is defined as the autocorrelation function for the nth transition state wave packet[16]. In present study, we focus on the flux-flux autocorrelation function for its ground transition state wave packet[16],

$$C_{ff}(t) = C_{ff}^0(t) = \langle \psi_g(t) | \hat{F} | \psi_g(t) \rangle. \tag{5.20}$$

The wave function $\psi_g(t)$ for the ground state transition state wave packet is given by,

$$\psi_g(t) = e^{-i\hat{H}t} e^{-\hat{H}\beta/2} \sqrt{\lambda} |+\rangle |g_0(\mathbf{s}') g_1(\mathbf{x}^1) \cdots g_N(\mathbf{x}^N)\rangle, \tag{5.21}$$

where $|g_k(\mathbf{x}^k)\rangle (k = 1, 2, ..., N)$ is the ground state wave function for $h_k(\mathbf{x}^k)$, $|+\rangle$ is the flux operator eigenfunction with non-zero eigenvalue of λ for coordinate perpendicular to the dividing surface in system, $|g_0(\mathbf{s}')\rangle$ is the ground state wave function on the dividing surface $\mathbf{s}'$. From Eq. 5.21, one can see that we first propagate each transition state wave packet in imaginary time to $\beta/2$, and then propagate it in real time.

Following Manthe and coworkers[90, 91, 15], we use transition state normal coordinate system in our calculation to minimize correlation effects in the transition state region. Normal modes and normal coordinates were calculated at the transition state geometry and the corresponding

linear transformation matrix was used throughout the calculation to convert the working coordinates into Cartesian coordinates. The transition state for the reaction, H_a-H_b-CH_3, is of C_{3v} symmetry with H_a-H_b-C lying on the C_{3v} symmetry axis. Here we labelled two hydrogen atoms involving in reaction to distinguish them from three other hydrogen atoms in the CH_3 group. For such a system of six atoms, there are 12 normal vibrational modes. They are the imaginary mode (Q_1) concerning the asymmetric stretching motion of the H_a-H_b-CH_3 fragments on the C_{3v} symmetry axis, a doubly degenerate low-frequency bending modes (Q_2,Q_3) mainly involving the motion of H_a atom, an umbrella mode (Q_4) for the non-reacting CH_3 group, a doubly degenerate high-frequency bending modes (Q_5,Q_6) mainly involving the motion of H_b atom, another doubly degenerate bending modes (Q_7,Q_8) essentially involving the motion of the hydrogens in nonreacting CH_3 group, a symmetric stretching mode (Q_9) of the H_a-H_b-CH_3 fragments on the C_{3v} symmetry axis, and a symmetric (Q_{10}) and doubly degenerate asymmetric stretches (Q_{11},Q_{12}) concerning mainly the nonreacting CH_3 group. Among all these modes, Q_1 and Q_9 are directly relevant to the reaction.

With mixed derivatives in the kinetic energy resulting from vibrational angular momentum neglected, the Hamiltonian for the system can be simply written as

$$\begin{aligned}\hat{H}(Q_1, Q_2, \cdots, Q_{12}) &= \sum_{i=1}^{12} -\frac{1}{2}\frac{\partial^2}{\partial Q_i^2} + \mathcal{V}(Q_1, Q_2, \cdots, Q_{12}) \\ &= \sum_{i=1}^{12} h_i(Q_i) + V(Q_1, Q_2, \cdots, Q_{12}), \end{aligned} \tag{5.22}$$

where

$$h_i(Q_i) = -\frac{1}{2}\frac{\partial^2}{\partial Q_i^2} + V_i(Q_i) \tag{5.23}$$

is the one-dimensional Hamiltonian for these normal modes. The reference potential $V_i(Q_i)$ for mode i is taken as

$$\begin{aligned} V_i(Q_i) &= 0, \quad \text{for } Q_1,\ Q_4, \text{ and } Q_9 \\ V_i(Q_i) &= \mathcal{V}(Q_1 = 0, \cdots, Q_i, \cdots, Q_{12} = 0) \quad \text{for other coordinates.} \end{aligned}$$

To choose a proper dividing surface, we define two new coordinates Q_1' and Q_9' by rotating Q_1 and Q_9 coordinates by an angle $\theta = 25°$,

$$\begin{aligned} Q_1' &= \sin\theta\, Q_1 + \cos\theta\, Q_9 \\ Q_9' &= \cos\theta\, Q_1 - \sin\theta\, Q_9. \end{aligned}$$

The dividing surface is located as $Q_1' = 0$ in our calculation.

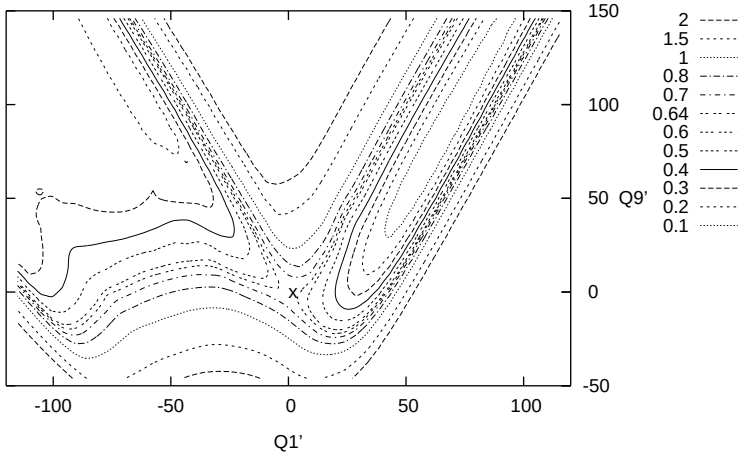

Figure 5.1: The minimum potential energy surface projected on the normal coordinates for Q_1' and Q_9' with energy minimized on the other coordinates. The unit for the coordinates is bohr· amu$^{1/2}$ and for energy is eV.

5.3.2 Numerical Details

To check the accuracy of the CC-TDSCF method, we need to calculate the autocorrelation functions by using exact quantum dynamics method. With the computer available to us, we are able to include up to ten of out the total twelve degrees of freedom. Intensive tests reveal that the doubly degenerate bending modes (Q_7,Q_8) involving the motion of the hydrogens in nonreacting CH_3 group essentially play no role in the dynamics, hence are excluded in this study. We use 49 sine-DVR in a range of [-120,120] for Q_1, 13 sine-DVR in a range of [-100,50] for Q_4, 29 sine-DVR in a range of [-50,150] for Q_9. For Q_2, Q_3, Q_5, Q_6, Q_{11}, and Q_{12}, we use 5 potential optimized DVR (PODVR)[38], and for Q_{10}, we use 6 PODVR. Hence the basis number used in the exact ten-dimensional quantum dynamics calculation reaches 1.7×10^9. The temperature considered in this study is 500 K. We propagate wave packet 50 steps for imaginary time propagation in Eq. 5.21. For real time propagation, the time step is 5 a.u. for the exact calculation, 1 a.u. for the CC-TDSCF method because of the self-consistent nature of the method.

5.3.3 Seven-dimensional (7D) Results

We first test the CC-TDSCF method on seven low frequency modes, i.e. Q_1, Q_2, Q_3, Q_4, Q_5, Q_6, and Q_9. In the CC-TDSCF calculation, we choose Q_1 and Q_9 as the system coordinates **s**. The other five coordinates involved, Q_2, Q_3, Q_4, Q_5, Q_6, are treated as five bath clusters, i.e. with one coordinate in every bath cluster. In the work, we use $\{(1,9),(2),(3),(4),(5),(6)\}$ to denote this kind of partition in coordinates, with the numbers in the first pair of parentheses referring the system coordinates, and the number(s) in the following pairs of parentheses referring the coordinate(s) in each bath cluster. Under this partition, one needs to solve one two-dimensional equation for the system, plus five three-dimensional equations for the bath clusters.

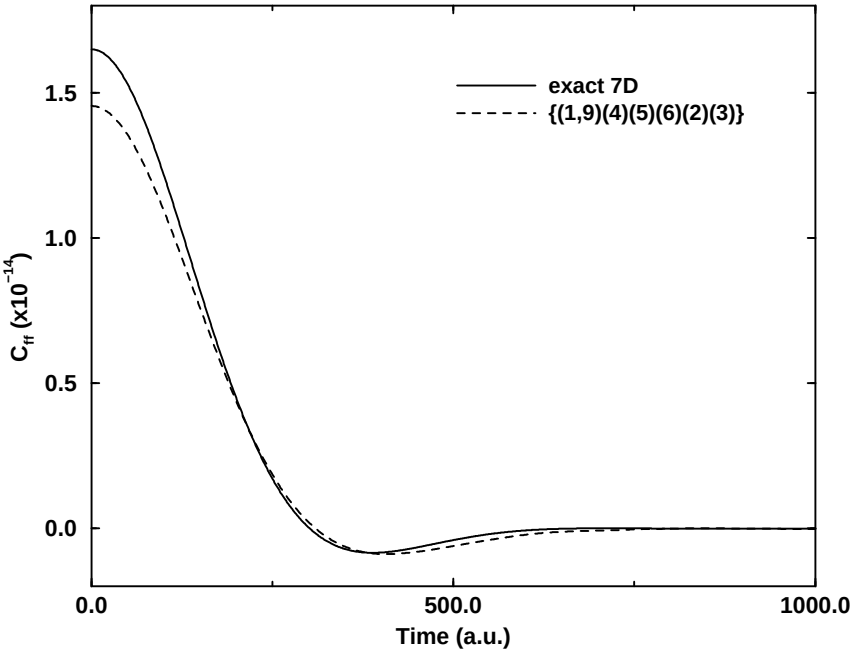

Figure 5.2: C_{ff} as a function of real time propagation for the ground transition state by using both exact quantum method and CC-TDSCF method with Q_1, Q_2, Q_3, Q_4, Q_5, Q_6, Q_9 included in calculations.

Fig.5.2 shows C_{ff} as a function of real time propagation, t, for the ground transition state by using both exact quantum method and CC-TDSCF method. The exact C_{ff} shown in Fig.5.2 exhibits a typical behavior for the flux-flux autocorrelation function for a direct reaction: it decays quickly as time increases, goes through zero at $t \sim 300$ a.u., then becomes a little bit negative, and finally gets stabilized at zero at $t \sim 700$ a.u. Hence for the temperature considered here, recrossing in flux-flux autocorrelation does occur, although it is not substantial. From Fig.5.2,

we can see that overall agreement between the CC-TDSCF C_{ff} and the exact one is quite good. At $t = 0$, it is about 12% smaller than the exact C_{ff}. It decays slightly slower than the exact C_{ff}, hence crosses with the exact C_{ff} curve at $t \sim 220$ a.u. The CC-TDSCF C_{ff} also moves in and out of the recrossing region slightly slower than the exact one.

It is quite interesting to see that the largest difference between CC-TDSCF and exact C_{ff} is at $t = 0$, right after the imaginary time propagation. Neglecting of correlations between bath modes prevent the whole system from relaxing as in the exact treatment during imaginary time propagation, making the CC-TDSCF C_{ff} at $t = 0$ smaller than the exact one. While during the real time propagation, neglecting of correlations between bath modes makes the whole system slower in dissipating energy and in moving away from the dividing surface. As a result, the CC-TDSCF C_{ff} decays slightly slower than the exact one as shown in Fig.5.2.

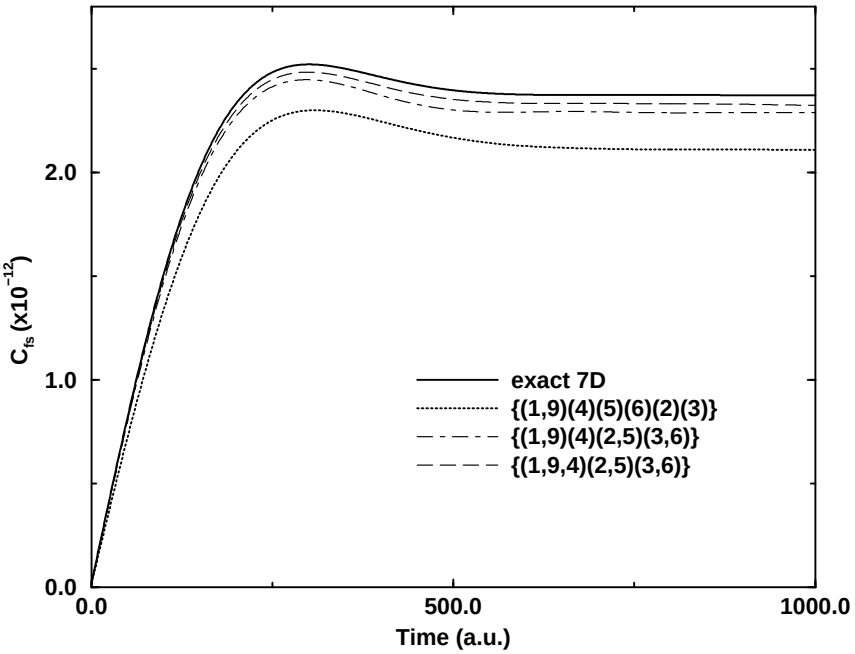

Figure 5.3: C_{fs} as a function of real time propagation for the ground transition state by using both exact quantum method and CC-TDSCF method with Q_1, Q_2, Q_3, Q_4, Q_5, Q_6, Q_9 included in calculations.

Fig.5.3 shows the exact and CC-TDSCF C_{fs} as a function of time by integrating the C_{ff} function shown in Fig.5.2. The curves look very similar, except that the CC-TDSCF C_{fs} is lower than the exact one. At $t \sim 300$ a.u. when they reach their maximum values, the CC-TDSCF C_{fs} is about 9% smaller than the exact one. The difference increases to 12% at $t \sim 700$ a.u. when they are stabilized. Thus the CC-TDSCF method introduces an error of 12% by approximating

a seven-dimensional problem with one two-dimensional plus five three-dimensional problems.

Under the $\{(1,9),(2),(3),(4),(5),(6)\}$ partition, we only took into account the correlations between system coordinates and individual bath coordinate, while neglected the correlations between bath coordinates. To investigate the importance of the correlations between bath coordinates, we carried many calculations by using different partition of the coordinates. It was found that the H_a bending modes Q_2 and Q_3 have substantial correlations with the H_b bending modes Q_5 and Q_6 on the same plane, i.e. Q_2 correlates Q_5, Q_3 correlates with Q_6. Thus an higher accuracy may be achieved by putting Q_2 and Q_5 in one bath cluster, Q_3 and Q_6 in another bath cluster. As we can see from Fig.5.3 that CC-TDSCF C_{fs} with the $\{(1,9),(4),(2,5),(3,6)\}$ partition is considerably more accurate than that with the $\{(1,9),(2),(3),(4),(5),(6)\}$ partition, when compared to the exact result. It is only smaller than the exact result by 3.5%. Under this partition, one needs to solve one two-dimensional equation for the system, one three-dimensional equation for Q_4, two four-dimensional equations for (Q_2, Q_5) and (Q_3, Q_6). If we put the umbrella mode Q_4 in the system, i.e. with a $\{(1,9,4),(2,5),(3,6)\}$ partition, we can further reduce the difference between the CC-TDSCF and exact C_{fs} to 2%. As we can see from Fig.5.3 that the CC-TDSCF C_{fs} with the $\{(1,9,4),(2,5),(3,6)\}$ partition is essentially identical to the exact one, indicating that there is very little correlation between (Q_2, Q_5) and (Q_3, Q_6) clusters. Another way to improve the accuracy of the $\{(1,9),(4),(2,5),(3,6)\}$ partition is to move Q_2 and Q_3 modes to the system, resulting a $\{(1,9,2,3),(4),(5),(6)\}$ partition. Fig.5.3 shows that the accuracy of the $\{(1,9,2,3),(4),(5),(6)\}$ partition is very close to that of the $\{(1,9,4),(2,5),(3,6)\}$ partition. Compared to the $\{(1,9),(4),(2,5),(3,6)\}$ partition, the $\{(1,9,4),(2,5),(3,6)\}$ partition takes into account the correlations between Q_4 mode and Q_2, Q_3, Q_5, Q_6 modes, while the $\{(1,9,2,3),(4),(5),(6)\}$ partition takes into account the correlation between Q_4 mode and Q_2, Q_3 modes, the correlations between Q_2 and Q_6, Q_3 and Q_5. The close agreement between the $\{(1,9,4),(2,5),(3,6)\}$ partition and the $\{(1,9,2,3),(4),(5),(6)\}$ partition indicates to some extend that the correlation between Q_4 mode and Q_2, Q_3 modes are more important than the correlation between Q_4 mode and Q_5, Q_6 modes.

5.3.4 Ten Dimensional (10D) Results

Fig.5.4 and Fig.5.5 shows C_{ff} and C_{fs}, respectively, as a function of real time propagation, t, for the ground transition state by using both exact quantum method and CC-TDSCF method with Q_{10}, Q_{11}, and Q_{12} included in dynamical calculations. Before comparing the exact 10D result with the CC-TDSCF ones, let us make a comparison between the 7D and 10D exact results shown

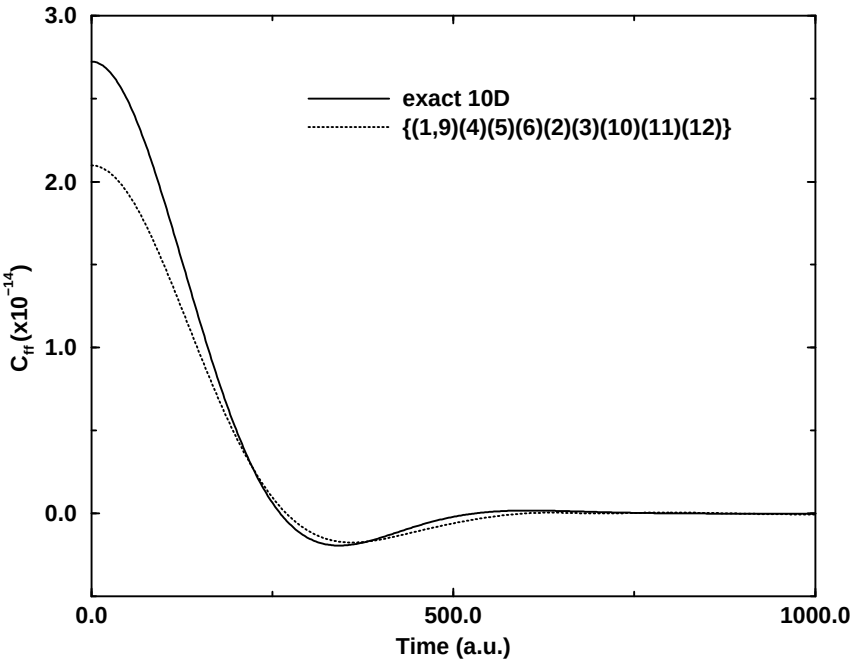

Figure 5.4: Same as Fig.5.2 except with three high frequency modes, Q_{10}, Q_{11}, and Q_{12} included.

in Fig.5.2 and 5.4. In our calculations, we set the ground state energy for every degree of freedom included in the calculation to be zero. Hence, if a degree of freedom plays no role to the dynamics, C_{ff} will only change very little (due to potential average effect) when that degree of freedom is included in dynamics calculations. Fig.5.4 show that the exact C_{ff} changes substantially when Q_{10}, Q_{11}, and Q_{12} are included in dynamical calculation. At $t = 0$, the 10D C_{ff} in Fig.5.4 is larger than 7D C_{ff} in Fig. 5.2 by about 60%. For the corresponding C_{fs} shown in Fig.5.3 and Fig.5.5, the 10D C_{fs} is about 50% larger than the 7D C_{fs}. It is well known that there is some kind of mixing between these stretching modes and the umbrella mode in normal coordinates, in particular at geometries far way from the reference geometry. Hence freezing stretch modes as in the 7D calculation may substantially underestimate C_{fs}, as discussed by Miller and coworkers in the H_2 + OH system[146].

As in the 7D case shown in Fig.5.2, we carried out a CC-TDSCF calculation with a $\{(1,9),(2),(3),(4),(5),(6),(10),(11),(12)\}$ partition. The comparison between the exact 10D C_{ff} and the CC-TDSCF one shown in Fig.5.4 is very similar to that in Fig.5.2, except that the difference between these two curves increases. At $t = 0$, the exact one is larger than the CC-TDSCF one by 22%. Consequently, the difference in C_{fs} between them shown in Fig.5.5 also increases compared

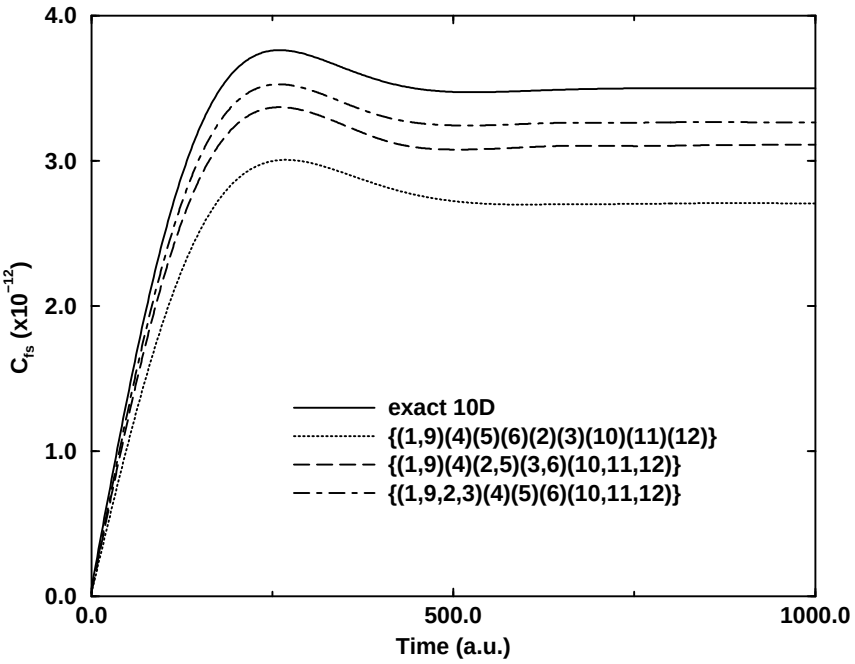

Figure 5.5: Same as Fig.5.3 except with three high frequency modes, Q_{10}, Q_{11}, and Q_{12} included.

to that in 7D. When stabilized, the exact C_{fs} is about 22% larger than the CC-TDSCF one. Thus, these three high frequency modes also have some strong correlations with themselves or other modes. Once again, we can see that the CC-TDSCF C_{ff} decays slower than the exact one as in 7D case, and it becomes slightly larger than the exact one at $t \sim 230$ a.u. for the reason discussed.

As in 7D calculations shown in Fig.5.3, bath modes are combined together as clusters to take into account the correlations between them. One partition we tried is $\{(1,9)$,(4),$(2,5)$,$(3,6)$, $(10,11,12)\}$ following the 7D calculation, with additional three high frequency modes put in one cluster. As we can see from Fig.5.5 that the $\{(1,9),(4),(2,5),(3,6),(10,11,12)\}$ partition is considerably more accurate than the $\{(1,9),(2),(3),(4),(5),(6),(10),(11),(12)\}$. It cuts the error of the later partition by half to about 11%, compared to the exact result. But this error is obviously larger than that of 3.5% for the $\{(1,9),(4),(2,5),(3,6)\}$ partition, indicating Q_{10}, Q_{11}, and Q_{12} modes not only correlate among themselves, they also correlate to other modes.

After intensive tests, we found that Q_{10}, Q_{11}, and Q_{12} also correlate with Q_2 and Q_3 modes. Since $Q_2(Q_3)$ correlates with Q_4, Q_5, Q_6 modes to some extend, one way to take into account all the correlations Q_2 and Q_3 have with Q_4, Q_5, Q_6, Q_{10}, Q_{11}, and Q_{12} modes is to put Q_2 and Q_3

in the system, resulting in a $\{(1,9,2,3),(4),(5),(6),(10,11,12)\}$ partition. Under this partition, one needs to solve one four-dimensional equation for the system, three five-dimensional equation for Q_4, Q_5, and Q_6, and one seven-dimensional equation for Q_{10}, Q_{11}, and Q_{12}. It sounds quite expansive to solve these equations, but compared to solving the original ten-dimensional equation, the computational effort involved here is substantially reduced because the number of basis used in the exact 10D calculations is $13 \times 5 \times 5 = 325$ times larger than that for the seven-dimensional equation. For the basis set used in this study, the CC-TDSCF calculation is about a factor of 10 faster than the exact one. As we can see from Fig.5.5 that The CC-TDSCF C_{fs} with the $\{(1,9,2,3),(4),(5),(6),(10,11,12)\}$ partition agrees with the exact one rather well. It is only smaller than the exact one by 6% at $t = 700$ a.u.

5.3.5 Conclusions

We calculated the flux-flux autocorrelation functions for the H + CH_4 reaction by using the exact quantum dynamics method and CC-TDSCF method on the potential energy surface recently developed by Manthe and coworkers. Since Q_7 and Q_8 are not important to the dynamics, we did not include them in present study. For the remaining ten modes, we carried two sets of calculations, one with seven low frequency modes, $Q_1 - Q_6$, and Q_9 included, the other including all these ten modes.

Comparison of flux-flux autocorrelation functions obtained by using the exact dynamics method and the CC-TDSCF method revealed that the CC-TDSCF method is capable of producing very accurate results. For the 7D case, the largest difference between the exact one and the CC-TDSCF one is 12% when the five bath modes were treated as five bath clusters in the $\{(1,9),(2),(3),(4),(5),(6)\}$ partition. This error was reduced to 3.5% when the $\{(1,9),(4),(2,5),(3,6)\}$ partition was employed. The CC-TDSCF method gave an error of 2% with the $\{(1,4,9),(2,5),(3,6)\}$ partition. When the three high frequency modes Q_{10}, Q_{11}, and Q_{12} were included in dynamics calculations, a simple $\{(1,9),(2),(3),(4),(5),(6),(10),(11),(12)\}$ partition gave an error of 22%, indicating these three high frequency modes have some strong correlations among themselves and/or with other bath modes. By using a $\{(1,9)$,(4),$(2,5)$,$(3,6)$, $(10,11,12)\}$ partition, we can reduce the error to 11%. The error can be reduced further to 6% by putting Q_2 and Q_3 in the system in a $\{(1,9,2,3),(4),(5),(6),(10,11,12)\}$ partition.

All these calculations clearly showed that the CC-TDSCF method is a very powerful approximation quantum dynamics method. It allows us to partition a big problem into several smaller ones. By changing partition systematically, one can investigate the correlations between different

degrees of freedom. By grouping modes with strong correlations together as a cluster, one can systematically improve accuracy of the result. And by choosing the system and bath clusters carefully, one can always keep the number of dimensions in CC-TDSCF within the computational power resource.

5.4 Application to the H Diffusion on Cu(100) Surface

The diffusion dynamics of a H atom on the Cu(100) surface in the uncorrelated hopping regime has already been investigated by Zhang and Light[16] using the transition state wave packet (TSWP) approach and the flux-flux correlation function to calculate the thermal rate constant. This time-dependent quantum simulation showed that the motions of the surface are important to damp the recrossing of the transition state surface in order to converge the correlation function and determine the hopping rate. However, due to the demanding nature of quantum dynamical calculations, only up to eight degrees of freedom for the surrounding surface were included, even though the inclusion of eight degrees of freedom are sufficient to damp the recrossing. Since the scale of CC-TDSCF approximation approach is determined by the product of the number of basis functions for system modes and the sum of the numbers of basis functions for each bath cluster, this smaller number, compared to that of the exact TSWP, shows its potential to solve this problem. We first have to check the possibility of its applications to this kind of systems. In this work we calculated the flux-flux autocorrelation functions by using both the exact quantum dynamics approach and CC-TDSCF approach for comparison.

5.4.1 System Model and Potential Energy Surface

Following the previous work, we use the same model system and potential energy surface to study hydrogen diffusion on Cu(100) surface, i.e., the potential energy surface is approximated as the sum of Morse-spline potentials for both the H-Cu and Cu-Cu pair interactions as used by Wonchoba and Truhlar [142] (WT). The functional form is

$$V(R) = \begin{cases} D[(1-e^{-\alpha(R-R_e)})^2 - 1], & R \le R_c - D_c \\ \sum_{i=3}^{i=5} C_i (R - R_c - D_c)^i, & R_c - D_c \le R \le R_c + D_c \\ 0, & R > R_c + D_c \end{cases} \tag{5.24}$$

where R is the Cu-Cu or H-Cu interatomic distance, D, α, and R_e are Morse parameters, and R_c, D_c, and C_i control the spline fits. The potential cutoff is $R_c + D_c$. All the parameters are shown in Table I for easy reference.

Table 5.1: Parameters used for Cu-Cu and H-Cu pair potentials

Parameter	Cu-Cu	H-Cu
$\alpha(\overset{\circ}{A}^{-1})$	2.287	1.43
$D(eV)$	0.40926	0.31602
$R_e(\overset{\circ}{A})$	2.578942	2.34
$R_c(\overset{\circ}{A})$	5.157883	7.02
$C_3(eV\overset{\circ}{A}^{-3})$	19.39	6.7049
$C_4(eV\overset{\circ}{A}^{-4})$	270.24	94.05
$C_5(eV\overset{\circ}{A}^{-5})$	1013.54	353.68
$D_c(\overset{\circ}{A})$	0.0529	0.0529

A lattice constant of $d = 3.5818\ \overset{\circ}{A}$ is also used by minimizing the interaction potential between a Cu atom and all its neighboring Cu atoms within distance R_c+D_c as done by Zhang and Truhlar [142]. This value is close to the experimental lattice constant of $3.61\overset{\circ}{A}$ for Cu. Thus the nearest neighbor distance between two Cu atoms on the (100) surface is $a = d/\sqrt{(}2) = 2.5327\ \overset{\circ}{A}$, and the interplanar distance is $d/2 = 1.7909\ \overset{\circ}{A}$. The Cu atoms on the surface are further relaxed with the distance between the first and second (100) plane of Cu atoms increased by $0.0267\overset{\circ}{A}$ so that the surface Cu atoms are in their equilibrium positions in the direction perpendicular to the surface.

In this model system, only six of the Cu atoms in the lattice are allowed to move, but the rest of the Cu atoms are held fixed at the positions described above to provide a surrounding framework for the mobile Cu atoms. The surrounding set of atoms extends far enough in all directions such that it includes all bulk lattice sites within the cutoff distance of the interaction potential to any movable Cu atom. Thus the lattice is effectively infinite, and any further increase in the lattice of fixed Cu atoms will not have any effect on the movable Cu atoms or the H atom.

Figure 5.6 shows the geometry of the six mobile Cu atoms labelled from 1 to 6 which will be explicitly included in the quantum calculations, together with the two equilibrium binding sites of H denoted as R (reactant) and P (product). The surface diffusion process to be modelled consists of the H atom hopping from site R to site P. The saddle point for this hopping process is denoted by S in Fig.5.6. Similarly, these six mobile Cu atoms are divided into three groups, $(1, 2)$, $(3, 4)$,

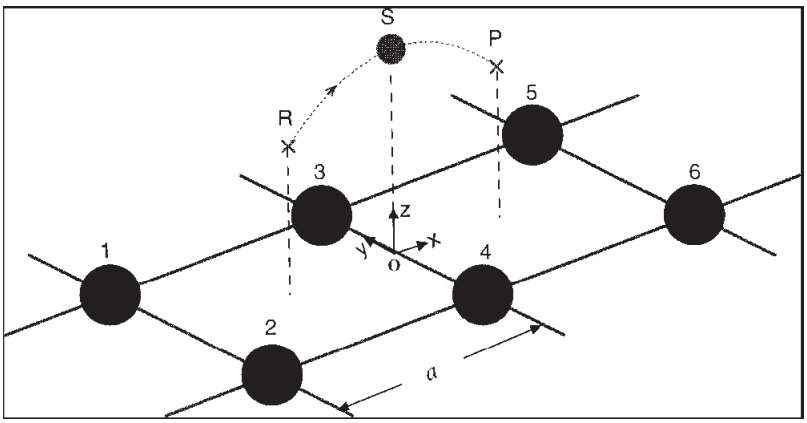

Figure 5.6: Reactant site (R), saddle point (S), product site (P), and the hopping path for diffusion of an H adatom on the Cu(100) surface. The six nearest neighbor Cu atoms to the saddle point are labeled from 1 to 6. The coordinate system for the H atom is also shown.

and $(5,6)$. For each group of Cu atoms, there are a total of six degrees of freedom. These six individual degrees of freedom are combined into vibrational modes of relative and center of mass motion for each pair as we do for a two particle system. For example, for the $(1,2)$ group the original six degrees of freedom are denoted as (x_i, y_i, z_i) $(i = 1, 2)$, measured as the displacement of a Cu atom away from its original given position. The modes of relative and center of mass motions are then defined as,

$$\begin{aligned} x^{12} &= x_1 - x_2; \quad X^{12} = \frac{x_1 + x_2}{2}, \\ y^{12} &= y_1 - y_2; \quad Y^{12} = \frac{y_1 + y_2}{2}, \\ z^{12} &= z_1 - z_2; \quad Z^{12} = \frac{z_1 + z_2}{2}, \end{aligned} \tag{5.25}$$

To calculate $k(T)$, we choose $x = 0$ to be the surface dividing the two unit cells surrounded by the six movable Cu atoms as shown in Fig.5.6. On this dividing surface we construct the transition state wave packets and measure the flux correlation functions. With this dividing surface the system is symmetric with respect to $x = 0$ provided we treat the (identical) (1,2) and the (5,6) Cu groups equally. Therefore, we can calculate the thermal rate constant by propagating the wave packets from 0 to a time t when the time integral of the correlation function is converged. In order to facilitate monitoring the convergence the time integral, in most cases, we will show the integral of $C^i_{ff}(T,t)$ with time,

$$C^i_{fs}(t) = \int_0^t C^i_{ff}(T,t')dt' \tag{5.26}$$

It is important to note that only when the system is symmetric with respect to the dividing surface, is $C^i_{fs}(\infty)$ directly related to $k(T)$. Otherwise, $C^i_{fs}(t)$ is just a notation for the integral of $C^i_{ff}(T,t)$ from time 0 to t.

5.4.2 Numerical Details

The results presented here are for $T = 300K$. The H atom is restricted to the two unit cells surrounding the saddle point where the initial wave packets are constructed as shown in Fig.5.6 because we are only concerned with diffusion due to the uncorrelated hops between neighboring unit cells. The range of the z coordinate is $[1.0, 4.8]a_0$. The number of steps used to propagate a transition state wave packet by $\beta/2$ varies with temperature. At $T = 300K$, 30 steps are used. For the real time propagation, we use $\Delta t = 15a.u.$ for exact transition state wave packet study and $\Delta = 5a.u.$ for continuous configuration time-dependent self-consistent field (CC-TDSCF) study.

5.4.3 Results and Discussions

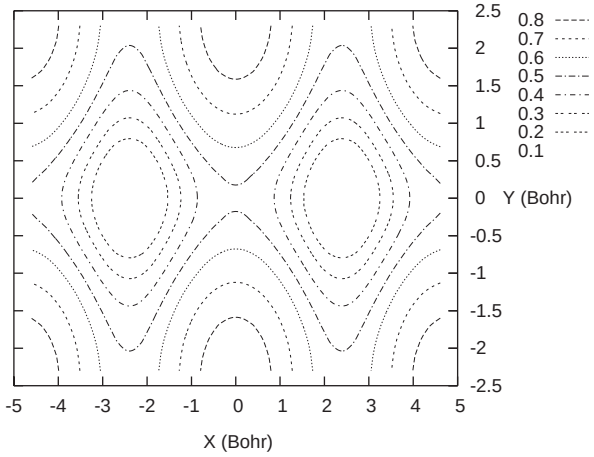

Figure 5.7: The minimum potential energy surface projected on the coordinates for x^H and y^H with energy minimized on the other nine coordinates (z^H, X^{12}, y^{12}, Z^{12}, X^{56}, y^{56}, Z^{56}, X^{34}, y^{34}, Z^{34}). The unit for energy is eV.

In order to describe the diffusion of hydrogen on the mobile Cu surface, there are three degrees of freedom to describe the motions of the H adatom at x, y, and z directions and eighteen degrees of freedom defined in Eq.(5.25) to describe the six mobile Cu atoms, including the six modes for

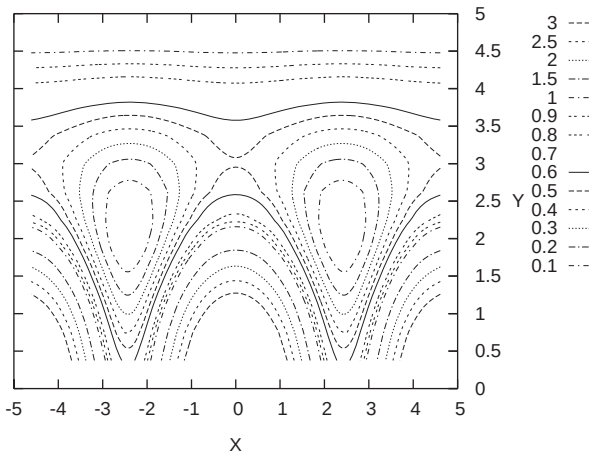

Figure 5.8: The minimum potential energy surface projected on the coordinates for x^H and z^H with energy minimized on the other nine coordinates (y^H, X^{12}, y^{12}, Z^{12}, X^{56}, y^{56}, Z^{56}, X^{34}, y^{34}, Z^{34}). The unit for energy is eV.

the (1,2) Cu group, for the (3,4) Cu group and for the (5,6) Cu group. As reported, for the (1,2) Cu group or (5,6) Cu group, there are three of six modes which are significantly excited during the propagation of the transition state wave packet. They are the center of mass mode in the x direction (X^{12} or X^{56}), the relative motion in the y direction (y^{12} or y^{56}), and the center of mass mode in the z direction (Z^{12} or Z^{56}). The other three modes essentially remain in their ground states. This suggests that the six surface modes for the (1,2) Cu group and (5,6) Cu group (X^{12}, y^{12}, Z^{12}, X^{56}, y^{56}, and Z^{56}) are much strongly coupled the motion of the H adatom. It can be understood easily in a classical picture with the help of Fig.5.6. When the H atom falls from the saddle point, it will move on the $y = 0$ plane toward the binding site (R or P) and get close to the (1,2) or (5,6) Cu group. The forces from the H atom on the 1 and 2 Cu pair (or 5 and 6 Cu pair) have the same magnitude and direction on the two atoms in the x and z directions, but are opposed in the y direction. Thus in x and z, the H atom pushes the 1 and 2 Cu atoms (or 5 and 6 Cu atoms) in the same direction, exciting the center of mass motions, but in the y direction relative motion is excited. However, the motions for the (3,4) Cu pair are different from the (1,2) Cu group and (5,6) Cu group, since they are the unique "transition state pair". The excitation of the Cu pair in the x direction is very mild compared to that for the other two Cu groups. The relative motion in the y direction (y^{34}) and the center of mass mode in the z direction (Z^{34}) are also strongly coupled with the hydrogen motion. So there are eight surface modes (X^{12}, y^{12}, Z^{12}, X^{56}, y^{56}, Z^{56}, y^{34}, Z^{34}) strongly coupled with the motion of the H atom and two modes (X^{34} and

z^{34}) are mildly coupled, while the rest surface modes are weakly coupled. In this study, we have used two sets of modes to compare the calculation results with the exact transition state wave packet method and the CC-TDSCF method. One set of modes includes the hydrogen motion on x and z direction and the eight important surface modes and X^{34}. This is reasonable because the diffusion of the H adatom from the saddle point to reactant site or the product site is on the xz plane and we then could consider only these two motions to save calculation time. The other set of modes includes the hydrogen motions on x, y, z directions and the eight important surface modes as previous work. In addition, the range of the H atom motion is limited to two unit cells, because we also want to see only how the energy of the H atom can transfer to the Cu motion to stabilize C_{fs}. For each of these Cu modes, we use three to four vibrational states which are obtained from the optimized configuration of the system with the H adatom on the saddle point. This guarantees that the Cu vibrations are not excited when the H atom sits on the saddle point.

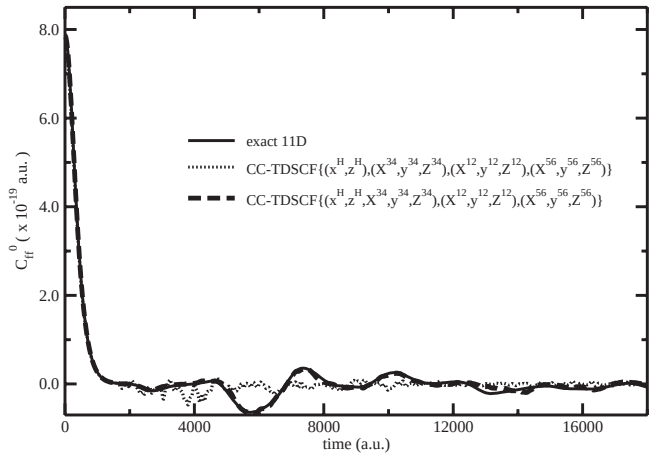

Figure 5.9: C^0_{ff} as a function of real time t for the ground transition state by using both the exact transition state wave packet method and CC-TDSCF method with the hydrogen motions only on x and z direction, and the nine surface modes (X^{12}, y^{12}, Z^{12}, X^{56}, y^{56}, Z^{56}, X^{34}, y^{34}, Z^{34}) included in calculations.

We first test the CC-TDSCF method on the eleven modes, x^H, z^H, X^{12}, y^{12}, Z^{12}, X^{56}, y^{56}, Z^{56}, X^{34}, y^{34} and Z^{34}. In the CC-TDSCF calculation, we first choose only x^H and z^H as the system coordinates and the other nine surface modes involved are treated as three bath clusters according to the corresponding Cu groups, i.e., (X^{12}, y^{12}, Z^{12}), (X^{56}, y^{56}, Z^{56}), (X^{34}, y^{34}, Z^{34}). This is because, as we have tested, the couplings between the surface modes for a same group are important and much larger than those between other surface modes, for example, the

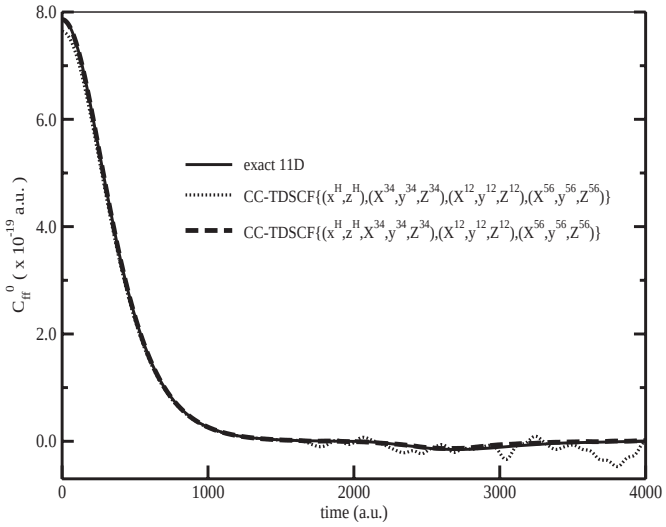

Figure 5.10: The same C^0_{ff} as Fig.5.9 with real time from 0 to 4000 a.u.

couplings between (X^{12}, X^{34}, X^{56}). Noted that we use the same form to denote this partition, $\{(x^H,\ z^H),\ (X^{12},\ y^{12},\ Z^{12}),\ (X^{56},\ y^{56},\ Z^{56}),\ (X^{34},\ y^{34},\ Z^{34})\}$, as that for H+$CH_4$ reaction. Under this partition, one needs to solve one two-dimensional equation for the system, and three five-dimensional equations for the bath clusters.

Fig.5.9 shows C_{ff} as a function of real time propagation, t, for the ground transition state by using both exact transition state wave packet method and CC-TDSCF method. The exact C^0_{ff} exhibits a typical behavior for the flux-flux autocorrelation function with recrossing: it decays quickly as time increase, goes through zero at $t \sim 1800a.u.$, then becomes a bit negative, and keep oscillating around zero but with amplitude decreasing as time, and finally get stabilized near zero at $t \sim 18000a.u.$ Hence for the temperature considered here, the recrossing in flux-flux autocorrelation does occur, which is observed as before [16]. This is because when the hydrogen falls from the saddle point to the binding site (R or P), the hydrogen could not be trapped in the binding site and its translation energy is only partly transferred to the surface motions. However, for longer times, the Cu modes absorb the activation energy of the H atom and suppress recrossing of the transition state surface, resulting in convergence of the autocorrelation function and the hopping rate. From Fig.5.9, we can see that the agreement between the exact C^0_{ff} and the CC-TDSCF ones is quite good. At time $t = 0$, the CC-TDSCF C^0_{ff} under the $\{(x^H, z^H), (X^{34}, y^{34}, Z^{34}), (X^{12}, y^{12}, Z^{12}), (X^{56}, y^{56}, Z^{56})\}$ partition is about 3% smaller than the exact, and then decays similar to the exact C^0_{ff}, however, when reaching the zero (at $t \sim 1600a.u$),

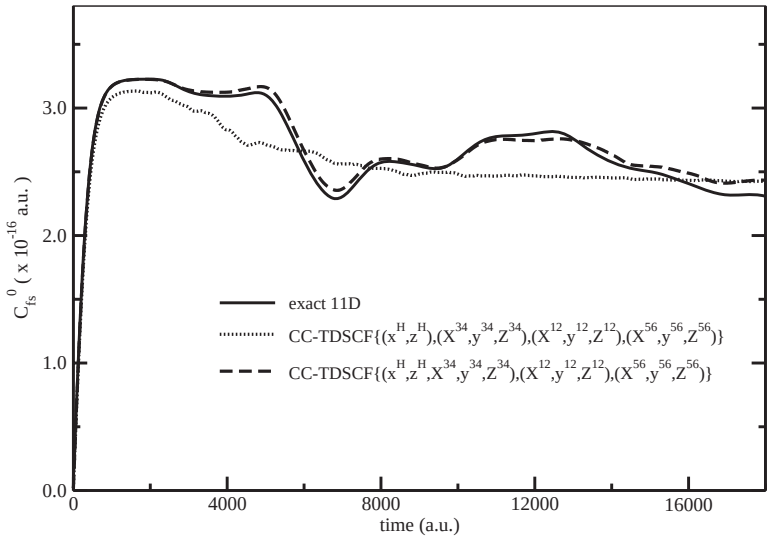

Figure 5.11: C_{fs}^{0} as a function of real time t for the ground transition state by using both the exact transition state wave packet method and CC-TDSCF method with the hydrogen motions only on x and z direction, and the nine surface modes (X^{12}, y^{12}, Z^{12}, X^{56}, y^{56}, Z^{56}, X^{34}, y^{34}, Z^{34}) included in calculations.

it begins to oscillate faster and more complex than the exact one.

Similar to the CC-TDSCF C_{ff} for the H+CH_4 reaction, some difference between CC-TDSCF and exact C_{ff} is at $t = 0$, right after the imaginary time propagation, because neglecting of correlations between bath clusters prevent the whole system from relaxing as in the exact treatment during the imaginary time propagation, making the CC-TDSCF C_{ff} at $t = 0$ smaller than the exact one. However, after $t \sim 1600 a.u.$, a large and complex recrossing happens, which is much different from the small recrossing for the H+CH_4 reaction. Firstly, because the reaction models for these two systems are different: the $H + CH_4 \rightarrow H_2 + CH_3$ is a direct reaction with two channels (reactant and product channel) which could be simulated with absorption potential to avoid boundary reflection, while the diffusion of H is limited in the two units and the simulation is carried out in $x \in [-a, a]$ without any absorbing potential. Thus the recrossing in this system should be large compared to that for H+CH_4 reaction. Secondly, the neglecting of the correlations between different bath clusters in CC-TDSCF prevents the energy of the system from being transferred among all the bath modes as in the exact one, and therefore recrossing becomes easier due to the delocalized energy in the system modes. Another possible reason is the neglecting of the phase of the TD wave packets for the bath clusters (modes). In CC-TDSCF method, the

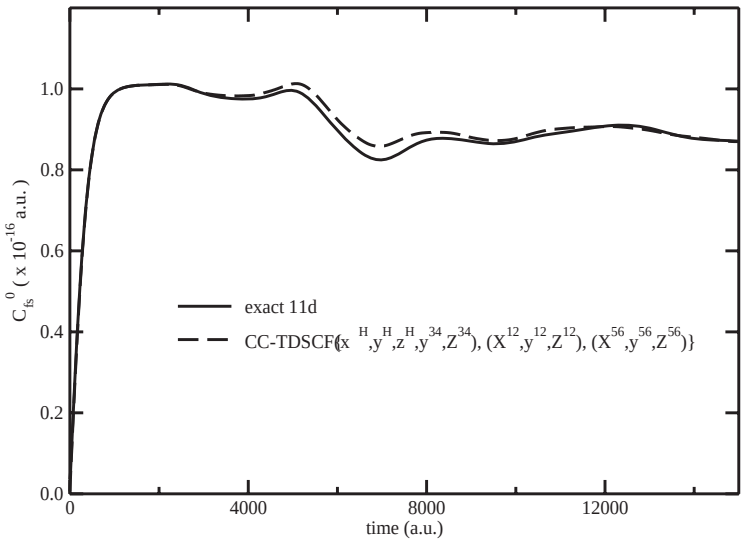

Figure 5.12: C_{fs}^0 as a function of real time t for the ground transition state by using both the exact transition state wave packet method and CC-TDSCF method with the hydrogen motions only on x, y, z direction, and the eight surface modes (X^{12}, y^{12}, Z^{12}, X^{56}, y^{56}, Z^{56}, y^{34}, Z^{34}) included in calculations.

mean field coupling from the bath clusters is used to form the Hamiltonian acting on the system modes and then the phases for the bath groups are neglected, which may result in this complex oscillation compared to the exact C_{ff}^0.

Fig.5.11 shows the exact and CC-TDSCF C_{fs} as a function of time by integrating the C_{ff} function shown in Fig.5.9. The curves looks very similar at the beginning, but some different (after $t \sim 1800a.u$) with time propagation: At $t \sim 1600a.u$, when they reach their maximum values, the CC-TDSCF C_{fs} is about 3% smaller than the exact one; after $t \sim 1800a.u$, they begin to oscillate and the exact one shows large oscillation curve due to its smooth recrossing in C_{ff}(Fig.5.9) while the CC-TDSCF C_{fs} gives a slow decreasing at time propagation due to its fast oscillation in C_{ff}; when $t \sim 18000a.u$, they becomes stabilized and the CC-TDSCF one is about 4.4% larger than the exact one. The slow decreasing of the CC-TDSCF C_{fs} as to the exact one is, as discussed before, due to the neglecting of the correlation among bath clusters making the relaxing of the system modes in CC-TDSCF longer. However, it is very exciting to see the good agreement between the stabilized CC-TDSCT C_{fs} and the exact one. Since only this stabilized value is used to predict the rate constant and the hopping rate, we could finally use CC-TDSCF to calculate the hopping rate as well as the exact method. And due to the advantage of CC-TDSCF in constructing basis, much more important surface modes could be included in

this method to study hydrogen diffusion within current computer memory.

Under the $\{(x^H, z^H), (X^{34}, y^{34}, Z^{34}), (X^{12}, y^{12}, Z^{12}), (X^{56}, y^{56}, Z^{56})\}$ partition, we have neglected the correlations between the bath clusters. However, we noted that the modes for the (3,4) Cu group have substantial correlation with those for the (1,2) or (5,6) Cu group. Therefore we carried another partition $\{(x^H, z^H, X^{34}, y^{34}, Z^{34}), (X^{12}, y^{12}, Z^{12}), (X^{56}, y^{56}, Z^{56})\}$ and treated the modes for the (3,4) Cu group as system modes. In this partition, we only neglect the correlation between the modes for the (1,2) Cu group and those for the (5,6) Cu group compared to the exact calculation and this correlation is verified to be very small in our test calculations. So the C_{ff} and C_{fs}, as predicted, shows a perfect agreement with the exact one (shown in Fig.5.9 and Fig.5.11). However, under this partition, one needs to solve one five-dimensional equation for the system and two eight-dimensional equations for the bath clusters and therefore it will bring much computational cost.

Even though the motion of the H adatom is only on the xz plane, the degree of freedom in y direction is also important in the quantum dynamics calculations. We then calculated the autocorrelation function based on the three dimensions for H and the eight important surface modes, x^H, z^H, X^{12}, y^{12}, Z^{12}, X^{56}, y^{56}, Z^{56}, y^{34} and Z^{34}. Fig.5.12 shows the C_{fs} as a function of real time propagation, t, for the ground transition state by using the exact quantum method and CC-TDSCF method with eleven modes included. We first make a comparison between the exact C_{fs} in Fig.5.11 and that in Fig.5.12. The exact C_{fs} in Fig.5.11 includes the mode of X^{34} while the C_{fs} in Fig.5.12 includes the mode of y^H. These two C_{fs} shows a similar curve, even though their absolute values are different due to the zero point energy for the mode y^H or X^{34} considered in our calculations. However, the later C_{fs} with y^H considered shows smaller recrossing and is easily stabilized as time propagation, which infers that the mode of y^H could stabilize the diffusion of the hydrogen from the saddle point to the binding sites. To compare the calculations using the exact quantum method and the CC-TDSCF method, we only carried one partition, $\{(x^H, y^H, z^H, y^{34}, Z^{34}), (X^{12}, y^{12}, Z^{12}), (X^{56}, y^{56}, Z^{56})\}$ and treated the three motions of hydrogen and the two mode of the (3,4) Cu group as system modes, and the other modes are grouped into two clusters. Under this partition, one needs to calculate one five-dimensional equation for the system and two eight-dimensional equations for the bath clusters. As expected, the calculated C_{fs}, like that in Fig.5.11, shows almost the same result with the exact one. However, the CC-TDSCF calculations require much less scale for basis functions (eight-dimensional equation) if compared to the exact 11D one, which thus clearly shows the applications of CC-TDSCF to this 11D model, but also to the models with more

surface modes considered although these eight surface modes discussed above are sufficient to damp the recrossing.

5.4.4 Conclusions

We calculated the flux-flux autocorrelation functions to study hydrogen diffusion on Cu(100) surface by using both the exact quantum dynamics method and CC-TDSCF method on a general potential energy surface as used by Wonchoba and Truhlar [142].

For CC-TDSCF approach, we mainly considered two kinds of partition of those important modes: one is to treat the hydrogen motions as system mode and the resting Cu surface modes grouped into three bath clusters according to the corresponding Cu groups; the other is to treat both the hydrogen motions and the two important motions of Cu(3,4) group as the system part and the resting Cu surface modes for Cu(1,2) and (5,6) grouped into two separated bath clusters. These two CC-TDSCF C_{ff} and C_{fs} both show good agreement with the exact ones, especially for the later case, i.e., the motions for Cu(3,4) are considered as system part. This infers that there is some correlation between the Cu(3,4) motions and Cu(1,2) or Cu(5,6) motions, and the correlation between the motions for Cu(1,2) and for Cu(5,6) can be neglected. It is significant to note that the CC-TDSCF results for the first partition gave a finally stabilized C_{fs} after a long real time propagation, only 3% different from the exact stabilized one. This shows that the CC-TDSCF could give an accurate rate constant value with the first partition, which requires only to solve one three-dimensional equation for the system and three six-dimensional equations for the bath clusters and therefore could save much computational cost and make it possible to consider higher dimensions.

This test calculation for hydrogen diffusion on Cu(100) surface showed that the CC-TDSCF method could be applied to this larger system and also a very powerful approximation quantum dynamics method since it allows us to partition a big problem into several smaller ones. In addition, it should be pointed out that in order to compare the computational results of exact TSWP or CC-TDSCF approach to experimental data, an accurate potential energy surface, such as, based on *ab initio* calculations, may be needed.

5.5 Application to a Double Well Coupled to a Dissipative Bath

To further test the efficiency of the CC-TDSCF approach, we consider a calculation of the thermal rate constant for an important model system, i.e., a one-dimensional double well linearly coupled to a harmonic bath. This model system is known to provide a realistic description of common condensed phase environments on the observable dynamics of the microscopic system of interest[17, 132, 133]. It has been studied extensively in recent years to test new quantum dynamics methodologies, in particular for those semiclassical theory based methodologies[144, 145].

5.5.1 System Model and Numerical Details

The Hamiltonian, written in the mass-weighted coordinates, is

$$H = H_s(\hat{p}_s, s) + \sum_{i=1}^{N_b} \left[\frac{1}{2}\hat{P}_i^2 + \frac{1}{2}\omega_i^2 (Q_i - \frac{c_i}{\omega_i^2} s)^2 \right] \tag{5.27}$$

where

$$H_s(\hat{p}_s, s) = \frac{1}{2}\hat{p}_s^2 - \frac{1}{2}\omega_b^2 s^2 + \frac{\omega_b^4}{16 V_0^{\ddagger}} s^4 \tag{5.28}$$

ω_b is the imaginary frequency at the top of the barrier, and $V_0^{\ddagger}$ is the barrier height with respect to the bottom of the well. The essential property of the harmonic bath is its spectral density,

$$J(\omega) = \frac{\pi}{2} \sum_j \frac{c_j^2}{m_j \omega_j} \delta(\omega - \omega_j) \tag{5.29}$$

which is chosen in the Ohmic form with an exponential cutoff,

$$J_o(\omega) = \eta \omega e^{-\omega/\omega_c} \tag{5.30}$$

The specific parameters we have chosen correspond to the model DW1 studied by Topaler and Makri using path integral methods[17], i.e., $\omega_b = 500 cm^{-1}$, $V_0^{\ddagger} = 2085 cm^{-1}$, and $\omega_c = 500 cm^{-1}$. The continuous bath spectral density of Eq.(5.30) is discretized to the form of Eq.(5.29) via the relation

$$c_j^2 = \frac{2}{\pi} \omega_j \frac{J_o(\omega_j)}{\rho(\omega_j)} \tag{5.31}$$

where $\rho(\omega)$ is a density of frequency satisfying

$$\int_0^{\omega_j} d\omega \rho(\omega) = j, \quad j = 1, \cdots, N_b \tag{5.32}$$

As noted in Ref.([147]), the precise functional form of $\rho(\omega)$ does not affect the final answer if enough bath modes are included, but it does affect the efficiency of solving the problem. Here, we simply choose $\rho(\omega) = \frac{N_b}{\omega_m}$, i.e., the frequency for the jth mode, ω_j is simply taken as $\omega_j = \frac{j}{N_b}\omega_m$ and the maximum cut-off frequency $\omega_m = 5\omega_c = 2500cm^{-1}$.

The starting point for the calculation of the rate constant is still the flux-flux correlation function,

$$k(T) = \frac{1}{2\pi Q_r(T)} \sum_i C^i_{fs}(T, t_p) = \frac{1}{2\pi Q_r(T)} \sum_i \int_0^\infty C^i_{ff}(T, t) dt \tag{5.33}$$

where $Q_r(T)$ is the reactant partition function and t_p is the plateau time for C_{ff}. We choose $s = 0$ to be the dividing surface and on this surface we construct the transition state wave packets and measure the flux correlation functions. Noted that all the bath modes on this surface are harmonic and the transition state wave packet can be constructed as the direct products of the eigenstates for these harmonic bath modes and the flux operator eigenstates on s. In the calculations, for small coupling parameter, for example $\eta/\omega_b = 0.1$, we could consider only 10 from the total 30 equally distributed bath modes to achieve converged results and around six potential-optimized discrete variable representation (PO-DVR) points are sufficient for the bath mode with the lowest frequency and only two PO-DVR points are for the bath mode with the highest frequency. Thus for this case, due to the small number of these basis functions, we employed the exact transition state wave packet to calculate the flux-flux correlation function. However, for large coupling parameter, more bath modes and more PO-DVR points for each mode are required to achieve the converged results, which therefore leads to exponential increase of the required computational resources. In this case we resort to approximations using CC-TDSCF method to simplify the computation.

The results presented here are for $T = 300K$ and 30 steps are used to propagate a transition state wave packet by $\beta/2$. For the real time propagation, we use $\Delta t = 10a.u.$ for exact transition state wave packet study and $\Delta t = 3a.u.$ for CC-TDSCF study.

5.5.2 Results and Discussions

As mentioned before, at small coupling parameter, converged results could be achieved with up to 10 dimensional bath modes considered and less than six basis functions were used to describe each bath mode. This small scale is because of the small coupling parameters, which make some bath modes behavior like harmonic function, and this also provides us a chance to carry out quantum dynamics calculations with exact TSWP approach. Here we first show in Fig. 5.13 the converged $C^n_{fs}(t)$, i.e., the time integral of the flux-flux autocorrelation function $C^n_{ff}(t)$, for

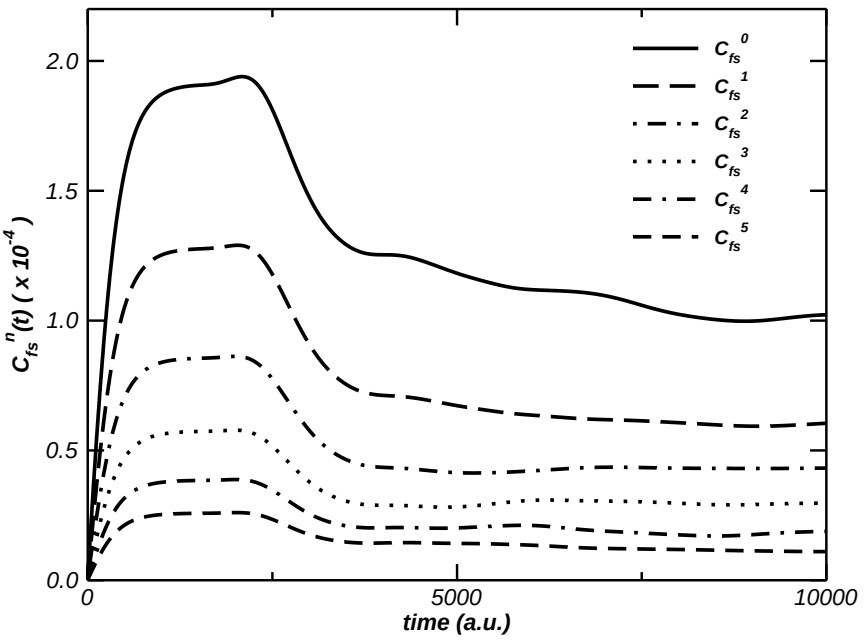

Figure 5.13: C_{fs}^{i} as a function of real time propagation for the ground transition state and one quantum of excitation on each bath mode for $\eta/\omega_b = 0.1$ from 10D exact quantum calculations.

the coupling parameter η/ω_b of 0.1 from 10D exact TSWP calculations. The C_{fs}^{0} denotes for the ground state on the dividing surface and $C_{fs}^{n}(n = 1, ...)$ for the state with one quantum of excitation included in the nth bath modes. It is clear to see that all the $C_{fs}^{n}(n = 0, 1, ...)$ approach their plateau values in steps. The first step corresponds to a maximum of C_{fs}^{n} and the subsequent stepwise change is due to quantum recrossing of the dividing surface. A similar downward step structure of the reactive flux has been observed by Makri. However, comparison between C_{fs}^{0} and $C_{fs}^{n}(n = 1, 2, ...)$ shows that, except a Boltzmann factor difference, C_{fs}^{0} reaches its plateau slower than other C_{fs}^{i}, which infers that recrossing could easily happens for those wave packets with high energies. Therefore, in order to better approximate the value for $C_{fs}(t) = \sum_i C_{fs}^{i}$, which is the sum for all possible transition state wave packets on the dividing surface, we take into consideration C_{fs}^{0} for the ground state as well as $C_{fs}^{n}(n = 1, ...)$ for the state with one quantum of excitation in the nth bath modes and assumed that C_{fs}^{i} with several quantum of excitation

on a bath mode could be obtained by a Boltzmann factor from C_{fs}^{n} with only one quantum of excitation on the same bath mode. Based on the obtained $C_{fs}(t)$, the rate constant is calculated with Eq.(5.33) and the results are always reported in terms of the time-dependent transmission coefficient defined as the ratio of the rate constant divided by the classical transition state theory (TST) value,

$$k_{TST} = \frac{1}{2\pi\hbar}\frac{k_B T}{Q} e^{-\beta E_b} \approx \frac{\omega_0}{2\pi} e^{-\beta E_b} \tag{5.34}$$

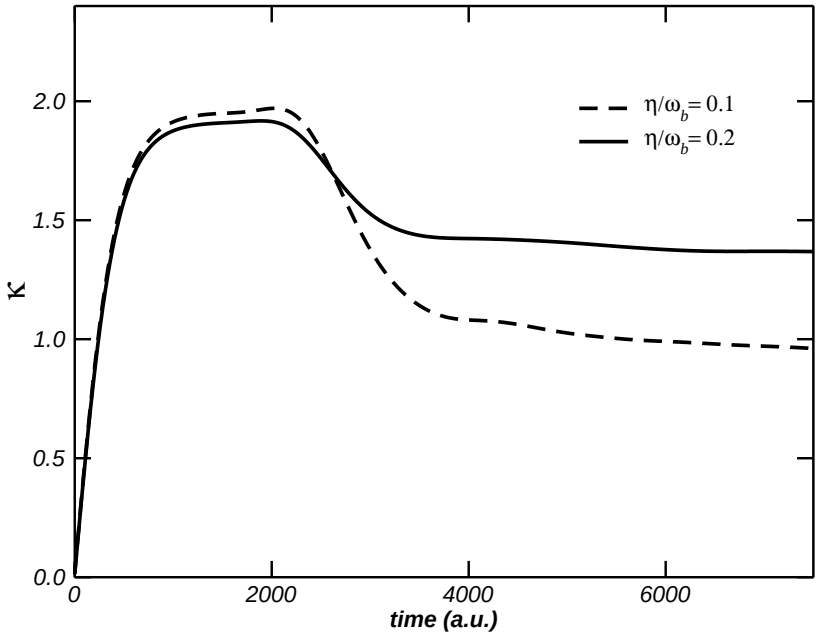

Figure 5.14: The transmission coefficient at $T = 300K$ for the coupling parameter $\eta/\omega_b = 0.1$ and 0.2.

Fig.5.14 shows the transmission coefficient $\kappa(t)$ at $T = 300K$ for the coupling parameter $\eta/\omega_b = 0.1$. It clearly shows the step structure, i.e., it reaches a maximum which is very close to the value of the transmission coefficient given by the centroid-based QTST and then reduces to a plateau of 0.94 due to quantum recrossing of the dividing surface.

For a comparison with C_{fs} for $\eta/\omega_b = 0.1$, Fig.5.14 also includes the transmission coefficient C_{fs} for the coupling parameter $\eta/\omega_b = 0.2$, which also shows the step structure. However, its maximum value on the first step is smaller than that for $\eta/\omega_b = 0.1$, while its final stabilized C_{fs}

on the second plateau is larger. This infers that for smaller coupling parameter, the wave packets could easily take direct barrier crossing on the dividing surface, but it would be difficult to be trapped in the double wells. In other words, for very weak coupling strength, recrossing dynamics become more profound and a longer time is thus required for the flux correlation function to reach its plateau.

For large coupling parameter, there should be more bath modes strongly coupled to the system mode and much more basis functions needed to describe these bath modes, which bring a large computational scale and makes it difficult to use the exact wave packet method to calculate the flux-flux correlation function. Therefore we resort to CC-TDSCF approximation method which assumes the wave function could be written as a product of single mode functions and thus considers the averaged effects of other bath modes on one bath mode. This approach, as we discussed in the previous two applications, has great advantages with its simplified scale for basis functions, however, since the correlations between the bath modes in different clusters are neglected, it may cause some difference from the exact TSWP results. Therefore, in this work, we first compared the results of these two approaches for a same case: a system mode coupled to eight dimensional bath modes at the coupling parameter of 1.0, where the eight bath modes are chosen with lower frequencies from the total 30 equally distributed bath modes from 0 to 2500cm^{-1}.

Fig. 5.15 gives the exact 8D result compared with three kinds of CC-TDSCF results with different partition (using the same denotation as before): {(s),(1)(2)(3)...(8)} with each bath mode grouped into its separate cluster; {(s,4),(1,2,3)(5,6,7,8)} with the fourth bath mode considered in system cluster and the other seven bath modes grouped into two clusters; {(s,4,5),(1,2,3)(6,7,8)} with two bath modes considered in system cluster and the other six bath modes grouped into two clusters. These kinds of partition are based on our test calculations that the couplings between two bath modes with frequencies close to each other are stronger than other kinds of coupling among bath modes. Comparison shows that both the exact C_{fs}^0 and the three CC-TDSCF C_{fs}^0 at first reach a same maximum value at $t = 1600 a.u.$, however, after $t = 1700 a.u.$, a significant difference happens. The exact C_{fs}^0 shows no recrossing. However the CC-TDSCF C_{fs}^0 for the partition of {(s),(1)(2)(3)...(8)} takes especially unstable recrossing. The C_{fs}^0 for the partition of {(s,4),(1,2,3)(5,6,7,8)} gives a stepwise recrossing to reach another lower plateau, i.e., this CC-TDSCF C_{fs}^0 is 7% smaller than the exact result. The C_{fs}^0 for the partition of {(s,4,5),(1,2,3)(6,7,8)} gives a smaller stepwise recrossing to reach a plateau and therefore it is

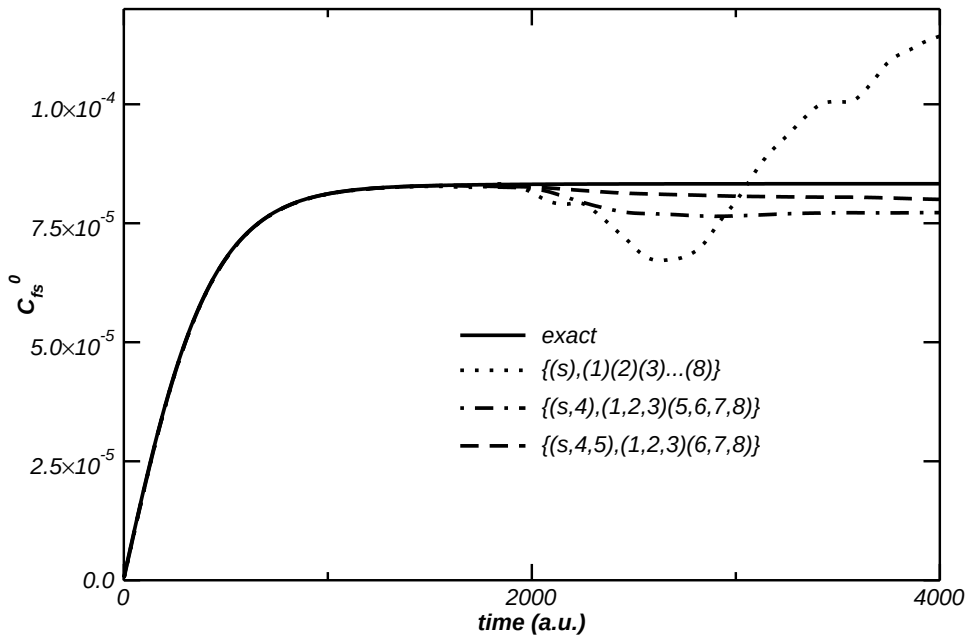

Figure 5.15: C_{fs}^0 for the ground transition state at the coupling parameter $\eta/\omega_b = 1.0$ obtained from the exact 8D TSWP calculations and 8D CC-TDSCF calculations with different partitions.

only 3% smaller than the exact result. This infers that in the CC-TDSCF approximation calculations, the less the couplings between the two separated bath clusters are neglected, the stronger the quenching of the recrossing is for the system mode, and then the closer the results are compared to the exact calculations. However, it is important to note that all these CC-TDSCF results give C_{fs}^0 a same maximum value, which is used in the exact calculation to obtain the rate constant due to no recrossing happening at the coupling parameter of 1.0. Therefore, we could get the correct C_{fs}^0 from all these CC-TDSCF calculations, i.e., the C_{fs}^0 value at the first plateau, assuming that the late recrossing is mainly due to the neglecting of the correlation between bath modes in different clusters.

Based on this assumption, we carried out higher dimensional CC-TDSCF calculations in order to get a converged C_{fs}^0 result for the coupling parameter of 1.0. Fig.5.16 shows the exact 8D result and the CC-TDSCF 30D results, i.e., all the 30 bath modes with frequencies equally

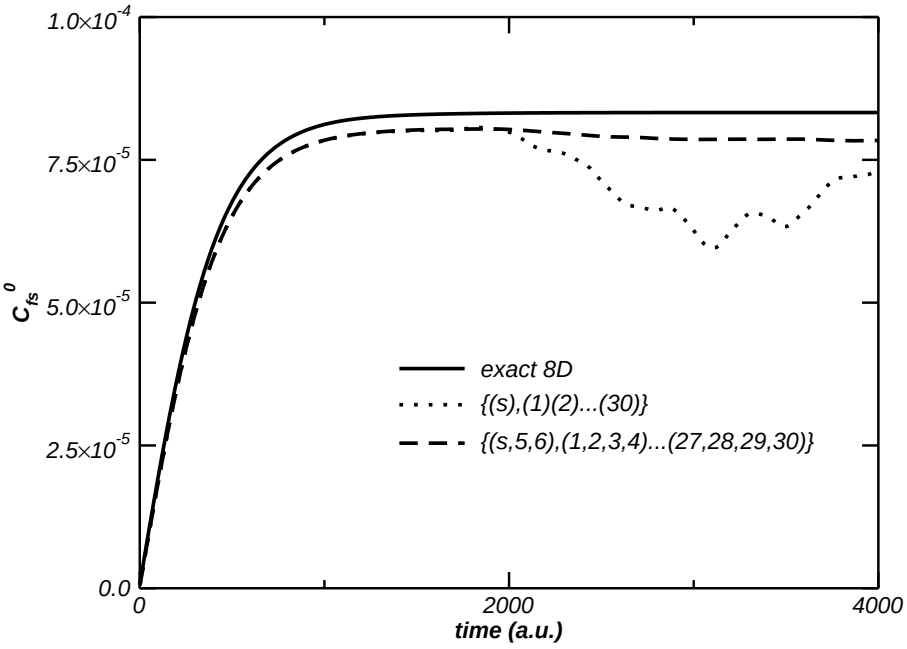

Figure 5.16: C^0_{fs} for the ground transition state at the coupling parameter $\eta/\omega_b = 1.0$ obtained from the exact 8D TSWP calcualtions and 30D CC-TDSCF calculations with different paritions.

distributed from 0 to 2500cm^{-1} are considered as well as the system mode in calculations. Two kinds of partition are taken in CC-TDSCF calculations: {(s),(1)(2)(3)...(30)} with each mode grouped into its own cluster and {(s,5,6),(1,2,3,4)...(27,28,29,30)} with two bath modes grouped into system cluster and the rest bath modes grouped into seven separate clusters. Here it is clear to see that consideration of only eight bath modes is unable to give a converged result if compared to the 30D results. In addition, two kinds of CC-TDSCF results give a same C^0_{fs} at the first plateau, which was used to calculate the rate constant as discussed before. It is interesting to see that the CC-TDSCF result for the partition of {(s,5,6),(1,2,3,4)...(27,28,29,30)} gives less recrossing compared to that for {(s,4,5),(1,2,3)(6,7,8)}. These two partitions both consider two bath modes in system cluster, however, for {(s,5,6),(1,2,3,4)...(27,28,29,30)}, with more bath modes considered, the system modes could be easily stabilized and thus less recrossing happens. Finally, similar to the coupling parameter of $\eta/\omega_b = 0.1$, we calculated CC-TDSCF C^n_{fs} with one

quantum excitation state on each bath mode, and then employed the Boltzmann factor to get $C_{fs} = \sum_i C_{fs}^i$, and then the rate constant and the transmission coefficient.

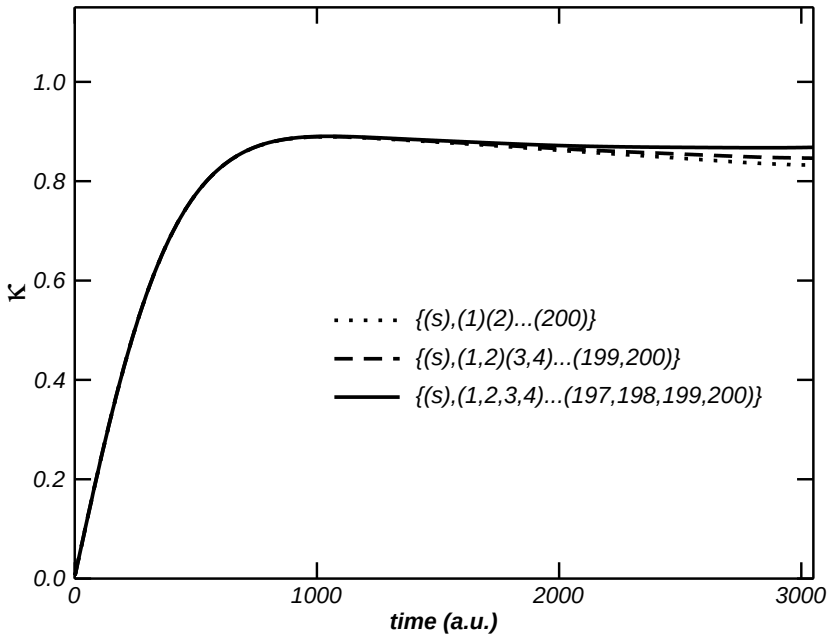

Figure 5.17: The time-dependent transmission coefficient for the coupling parameter $\eta/\omega_b = 3.0$ from CC-TDSCF calculations.

For larger coupling parameter, which requires more than 13 basis functions to describe each bath mode, the CC-TDSCF calculations can be easily done to obtain the flux-flux correlation function. Fig.5.17 shows the time-dependent transmission coefficient $\kappa(t)$ for the coupling parameter of $\eta/\omega_b = 3.0$ converged with 200 bath modes equally distributed from [0, 2500cm^{-1}]. Three ways of grouping the bath modes have been tested and the $\kappa(t)$ reach a same maximum value at around $t = 1000a.u.$ and then different recrossing happens: among these three ways, the largest recrossing flux happens with the 200 bath modes grouped one by one to 200 clusters, and the smallest recrossing flux happens for the 200 bath modes grouped into 50 clusters. It is reasonable because the more the coupling between bath modes is considered, the more stable the wave function is to be trapped in the double wells, and thus the less the recrossing happens. It is interesting to see that the recrossing in CC-TDSCF results is very small. We could imagine

that if there is a possibility to consider all the couplings among the bath modes, i.e., the exact calculations, there should be no recrossing and C_{fs} would keep on a plateau when it reaches the maximum value. Thus the CC-TDSCF could give a result only 3% smaller than the exact one.

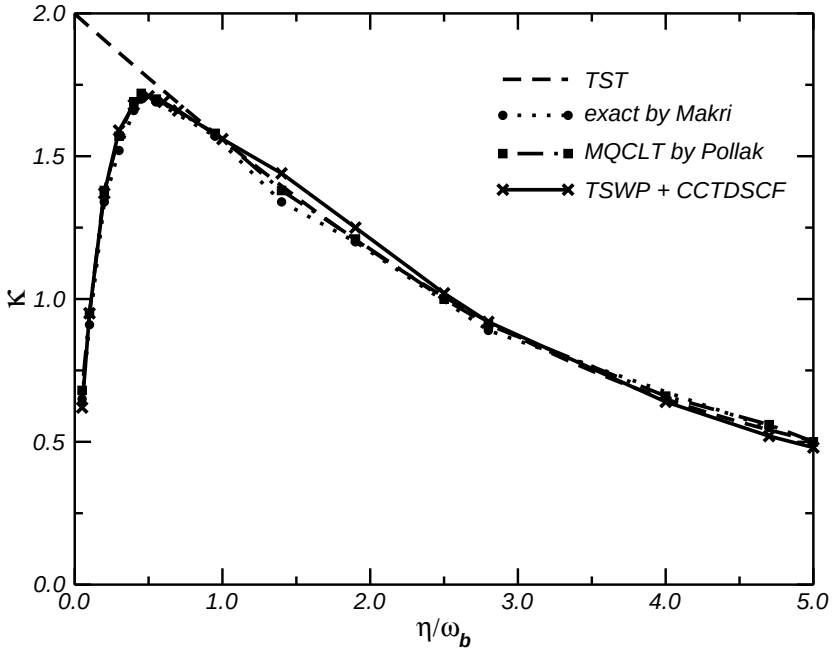

Figure 5.18: The transmission coefficient as a function the coupling parameter η/ω_b.

Therefore, the transmission coefficients for the coupling parameter less than 1.0 are calculated based on the exact TSWP approach, and those for the coupling parameter larger than 1.0 are based on the CC-TDSCF approximation calculations. The obtained transmission coefficients are plotted as a function of the dimensionless coupling parameter η/ω_b in Fig.5.18. Comparison with previous results shows that it can reproduce quite accurately the quantum turnover behavior of the rate constants from the energy diffusion to spatial-diffusion-limited region. And this study also shows the applicability of the CC-TDSCF for dealing with complex systems.

5.5.3 Conclusions

We calculated the transmission coefficient for the coupling parameter from 0.1 to 4.0 with the exact transition state wave packet(TSWP) and continuous configuration time-dependent self-consistent field(CC-TDSCF) approaches on the DW1 model for a double well coupled to a dissipative bath[17]. When the coupling parameter is less than 1.0, only eight bath modes coupled to the system mode are important to give a converged flux-flux correlation function and thus the exact TSWP approach is applied to this kind of case due to the small basis functions needed in calculations. However, when the coupling parameter is larger than 1.0, not only eight bath modes are not sufficient, but also the basis functions required to describe each bath mode increased to give a converged flux-flux correlation function. The basis function scale for this kind of case is beyond the exact TSWP calculations and we resorted to the CC-TDSCF approach. It is important to see that the CC-TDSCF results agree well with the exact TSWP ones for the first time step to reach a same maximum value. After that, no recrossing happens for the exact results, while some small recrossing does happen for the CC-TDSCF results due to the neglecting of some couplings between bath clusters. However the same CC-TDSCF maximum values as the exact ones provide the possibility of CC-TDSCF approach to give an accurate stabilized correlation function. Except that the flux-flux correlation function for ground state on the dividing surface is calculated, the C_{ff}^{i} for the states with one quantum of excitation in the ith bath mode are also included to calculate the rate constants based on an assumption that the C_{ff}^{n} with several quantum of exaction on a bath mode could be obtained by a Boltzmann factor from the one with only one quantum of excitation on the same bath mode. The final results obtained for the transmission coefficient as a function of the coupling parameters show good agreements with previous results, which infers the possibility and efficiency to apply CC-TDSCF to large complex system with some correlations between bath modes neglected.

Chapter 6

Conclusions

Calculation of quantum reaction probabilities and rate constants of chemical reactions remains one of the central problems in theoretical chemistry. In recent years, increase in computer power, progress in time dependent wave packet methods, and development of the famous operator formulations for cumulative reaction probabilities $N(E)$, flux-flux correlation functions C_{ff}, and the quantum thermal rate constants, have stimulated the applications of the transition state time dependent wave packet method (TSWP) to some quantum dynamics problems for small systems.

In this work, we first reported transition state quantum wave packet dynamics calculations for the unimolecular dissociation of formaldehyde (H_2CO) on a global potential energy surface for its S_0 ground state and with the nonreacting CO bond length fixed at its value for global minimum structure. The total cumulative reaction probabilities ($J = 0$) were calculated on two separate dividing surfaces (S_2 and S_3), which are respectively located at the asymptotic regions to two kinds of products, molecular products (H_2+CO) and radical products (H+HCO). The comparison of these two $N(E)$s suggests three reaction pathways involved as the total energy up to 4.60eV. At first with total energy much lower than 4.56eV, formaldehyde dissociates only through the molecular channel to H_2+CO; when the total energy increases to just near 4.56eV, the roaming atom channel opens up; while total energy is above 4.57eV, the threshold for the radical channel, formaldehyde also dissociates to radical products of H+HCO. Both the molecular channel and the roaming atom one produce H_2+CO, however, they show different dynamics information. The results about detailed H_2 rotational, H_2 vibrational, CO rotational state distributions given at six total energies, obtained by the projection of the flux at S_2 dividing surface on to the internal states for H_2 and CO, clearly show that the former pathway is to produce modest vibrational H_2

and hot rotational CO with large translational energy released, while the latter one is to produce highly vibrational H_2 and cold rotational CO with small translational energy released. These results not only give the state correlations for these two kinds of products, but also confirms that at energies just near and above the threshold of the radical channel(4.57eV), the second pathway, i.e., the roaming atom channel, opens up, which have shown good agreement with quasiclassical trajectory calculations and experiments, especially the opening of the second kind of products at excitation energy just near and above the threshold to radical channel. The investigation of time-dependent wave packet propagations also suggested two different reaction mechanisms corresponding to these reaction pathways. The former one is through the well-established skewed transition state and the latter one is through a pathway far away from the saddle point, which also confirms the roaming atom mechanism presented by Bowman *et al* [50]. It could be seen that the TSWP approach is very efficient and powerful to calculate $N(E)$ and product state distributions in this work, and the corresponding time-dependent dynamics information provides an alternative way to study reaction mechanism as the classical trajectory study. However, noted that there are some small unphysical negative distributions appearing at the total energy just near the threshold to radical channel. This may be due to the fitting region of two *ab initio* methods on the potential energy surface, where the initial transition state wavepackets were constructed. So this infers a need of a potential energy surface accurate and smooth enough for quantum dynamics calculations. In addition, the quantum calculation for this reduced five-dimensional reaction is still extremely time-consuming due to the dense open states on the first dividing surface within the energy region lower than the threshold of 4.57eV. There is a need to study this system with an alternative set of coordinates, which could provide a dividing surface with low density-of-states in the transition state region and also be transformed to Jacobi coordinates for further propagation, and thus a substantial computational cost can be reduced.

Secondly, seven- and eight- dimensional transition state wave packet dynamics calculations were done to study the $H+CH_4 \rightarrow H_2+CH_3$ reaction on the JG-PES. We employed the reduced-dimensional model for the $X+YCZ_3$ type of reaction, originally proposed by Palma and Clary[13], by restricting the CH_3 group under C_{3V} symmetry. In the seven dimensional calculations, the CH bond length in the CH_3 group is fixed at its equilibrium value of 2.067a.u. The remaining seven degrees of freedom were included in this study exactly. In the eight dimensional calculations, all the eight modes were included exactly. For both of these two models, we calculated the cumulative reaction probability at J=0 for the ground state and some vibrationally excited transition states on the dividing surface across the saddle point. Based on the obtained total cumulative reaction

probabilities for J=0, the rate constants were calculated for temperature values between 200 and 500 K employing the J-shifting approximation. The 7D and 8D results agree perfect with each other, suggesting the additional mode for the symmetry stretching in CH_3 group does not change in reaction within the temperature range considered here. The results also show quite good agreement with the previous 7D ISSWP rates and the 5D-SVRT rates, which suggests that it is possible to obtain the thermal rate constant from the state selected rate constant during the low temperature range considered here. However, the present results are much smaller than the full-dimensional MCTDH results by one to two orders of magnitude. Since both sets of results are obtained with the J-shifting approximation based on a high dimensional cumulative reaction probability for $J = 0$, the huge difference shows its special importance, which may be due to the different feature of the dynamics approaches as discussed by Varandas *et al*: MCTDH, as a kind of local dynamics approach, may ignore the implications of the PES topography away from the transition state region and therefore it gives different results from other kind of approaches called global dynamics approaches such as the one used in this study.

Although significant progress has been made in the development of time dependent wave packet method, the full quantum reaction dynamics for large systems remains unfeasible because of the exponential scaling of numerical effort with the size of the system. Therefore, there is a great interest in developing approximate yet accurate ways to treat reactive scattering. In this work, we focused on a new and efficient scheme for time-dependent self-consistent field (TDSCF) method, namely, continuous-configuration time-dependent self-consistent field (CC-TDSCF) method. The basic idea is to use discrete variable representation (DVR) for the system and then to each DVR point of the system a configuration of wave function in terms of direct product wave functions is associated for different clusters of the bath modes. In this way, the correlations between the system and bath modes, as well as the correlations between bath modes in each individual cluster can be described properly, while the correlations between bath modes in different clusters are neglected.

In this work, test applications of the CC-TDSCF approach were done to calculate the flux-flux autocorrelation functions or thermal rate constants on three large systems: H+CH_4, hydrogen diffusion on Cu(100) surface, and the double well coupled to a dissipative bath. The exact quantum dynamics calculations with TSWP approach were also included for comparison. In a simple CC-TDSCF calculation, the important modes for dynamics reactions, for example, the normal modes of Q_1 and Q_9 in H+CH_4 reaction, the diffusion motion of hydrogen on x, y and z directions, and the system mode s along the double well potential, are always treated

as the system modes, while the rest modes are individually treated in their own bath clusters. Under this partition, one needs to solve one n_s-dimensional equation for the system and n_b (n_s+1)-dimensional equations for bath modes, where n_s and n_b are respectively the number for system modes and bath modes. Thus CC-TDSCF approach allows us to partition a big problem into several smaller ones and compared to the exact calculation, the number of basis used is substantially reduced from $\prod_{i=1}^{n_s} m_{s,i} \prod_{j=1}^{n_b} m_{b,j}$ to $\prod_{i=1}^{n_s} m_{s,i} (\sum_{j=1}^{n_b} m_{b,j})$, where $m_{s,i}$ and $m_{b,j}$ are respectively the basis number for system mode(i) and bath mode (j). It is clear to see that this reduced size of basis functions provides potential applications of CC-TDSCF approach to large or complex systems.

Comparison of the flux-flux autocorrelation functions or rate constants for the three complex systems obtained by using the exact dynamics and the CC-TDSCF approach revealed that the CC-TDSCF approach is capable of producing very accurate results. Even though the difference between the exact one and the above simple CC-TDSCF partition may be very large, one can systematically improve accuracy of the result by grouping modes with strong correlations together as a cluster. And by choosing the system and bath clusters carefully, one can always keep the number of dimensions in CC-TDSCF within the computational power one has available. Therefore all the test calculations in this work clearly showed that the CC-TDSCF method is a very powerful approximation quantum dynamics approach and it can also be applied to other complex systems, especially those having small correlations between some bath modes.

Bibliography

[1] M. C. Chuang, M. F. Foltz, and C. B. Moore. *J. Chem. Phys.*, 87:3855, 1987.

[2] X. Zhang, S. Zou, L. B. Harding, and J. M. Bowman. *J. Phys. Chem. A*, 108:8980, 2004.

[3] N. Makri. *Annu. Rev. Phys. Chem.*, 50:167, 1999.

[4] M. Thoss and H. Wang. *Annu. Rev. Phys. Chem.*, 55:299, 2004.

[5] R. E. Wyatt and J. Z. H. Zhang ed. *Dynamics of molecules and chemical reactions*. Marcel Dekker, New York, 1996.

[6] W. H. Miller. in *Dynamics of molecules and chemical reactions,* edited by R. E. Wyatt and J. Z. H. Zhang. Marcel Dekker, New York, 1996.

[7] W. H. Miller, S. D. Schwartz, and J. W. Tromp. *J. Chem. Phys.*, 79:4889, 1983.

[8] D. H. Zhang and J. C. Light. *J. Chem. Phys.*, 104:6184, 1996.

[9] D. H. Zhang and J. C. Light. *J. Chem. Phys.*, 106:551, 1997.

[10] D. H. Zhang, J. C. Light, and S. Y. Lee. *J. Chem. Phys.*, 109:79, 1998.

[11] R. D. van Zee, M. F. Flotz, and C. B. Moore. *J. Chem. Phys.*, 99:1664, 1993.

[12] H. M. Yin, S. H. Kable, X. Zhang, and J. M. Bowman. *Science*, 311:1443, 2006.

[13] J. Palma and D. C. Clary. *J. Chem. Phys.*, 112:1859, 2000.

[14] H.-D. Meyer, U. Manthe, and L. S. Cederbaum. *Chem. Phys. Lett.*, 165:73, 1990.

[15] T. Wu, H.-J. Werner, and U. Manthe. *Science*, 306:2227, 2004.

[16] D. H. Zhang, J. C. Light, and S. Y. Lee. *J. Chem. Phys.*, 111:5741, 1999.

[17] M. Topaler and N. Makri. *J. Chem. Phys.*, 101:7500, 1994.

[18] John Z. H. Zhang. *Theory and Application of Quantum Molecular Dynamics*. World Scientific, Singapore, 1998.

[19] J. Ischtwan and M. A. Collins. *J. Chem. Phys.*, 100:8080, 1994.

[20] M. J. T. Jordan, K. C. Thompson, and M. A. Collins. *J. Chem. Phys.*, 102:5647, 1995.

[21] K. C. Thompson and M. A. Collins. *J. Chem. Soc. Faraday Trans.*, 93:871, 1997.

[22] K. C. Thompson, M. J. T. Jordan, and M. A. Collins. *J. Chem. Phys.*, 108:564, 1998.

[23] K. C. Thompson, M. J. T. Jordan, and M. A. Collins. *J. Chem. Phys.*, 108:8302, 1998.

[24] R. P. A. Bettens and M. A. Collins. *J. Chem. Phys.*, 111:816, 1999.

[25] D. H. Zhang, M. A. Collins, and S.-Y. Lee. *Science*, 290:961, 2000.

[26] M. A. Collins and D. H. Zhang. *J. Chem. Phys.*, 111:9924, 1999.

[27] R. P. Bettens, M. A. Collins, M. J. T. Jordan, and D. H. Zhang. *J. Chem. Phys.*, 112:10162, 2000.

[28] M. A. Collins. *Theor. Chem. Acc.*, 108:313, 2002.

[29] G. E. Moyano and M. A. Collins. *J. Chem. Phys.*, 121:9769, 2004.

[30] J. A. Fleck, Jr, J. R. Morris, and M. D. Feit. *Appl. Phys*, 10:129, 1976.

[31] M. D. Feit, J. A. Fleck, Jr, and a. Steiger. *J. Comput. Phys.*, 47:412, 1982.

[32] H. Tal-Ezer and D. Kosloff. *J. Chem. Phys.*, 81:3967, 1984.

[33] C. Lanczos. *J. Res. Natl. Bur. Stand.*, 45:255, 1950.

[34] T. J. Park and J. C. Light. *J. Chem. Phys.*, 85:5870, 1986.

[35] C. Leforestier, R. Bisseling, C. Cerjan, M. D. Feit, R. Friesner, A. Guldberg, A. Hammerich, G. Jolicard, W. Karrlein, H. D. Meyer, N. Lipkin, O. Roncero, and R. Kosloff. *J. Comput. Phys.*, 94:59, 1991.

[36] S. K. Gray. *J. Chem. Phys.*, 96:6543, 1992.

[37] Z. Bačić and J. C. Light. *Annu. Rev. Phys. Chem.*, 40:469, 1989.

[38] J. Echave and D. C. Clary. *Chem. Phys. Lett.*, 190:225, 1992.

[39] P. Ho, D. J Bamford, R. J. Buss, Y. T. Lee, and C. B. Moore. *J. Chem. Phys.*, 76:3630, 1982.

[40] C. B. Moore and J. C. Weisshaar. *Annu. Rev. Phys. Chem.*, 34:525, 1983.

[41] D. J. Bamford, S. V. Filseth, M. F. Foltz, J. W. Hepburn, and C. B. Moore. *J. Chem. Phys.*, 82:3032, 1985.

[42] D. Debarre, M. Lefebvre, M. Pelear, J.-P. E. Taran, D. J. Bamford, and C. B. Moore. *J. Chem. Phys.*, 83:4476, 1985.

[43] D. R. Guyer, W. F. Polik, and C. B. Moore. *J. Chem. Phys.*, 84:6519, 1986.

[44] T. J. Butenhoff, K. L. Carleton, and C. B. Moore. *J. Chem. Phys.*, 92:377, 1990.

[45] W. F. Polik, D. R. Guyer, and C. B. Moore. *J. Chem. Phys.*, 92:3453, 1990.

[46] K. L. Carleton, T. J. Butenhoff, and C. B. Moore. *J. Chem. Phys.*, 93:3907, 1990.

[47] T. J. Butenhoff, K. L. Carleton, R. D. van Zee, and C. B. Moore. *J. Chem. Phys.*, 94:1947, 1990.

[48] R. D. van Zee, C. D. Pibel, T. J. Butenhoff, and C. B. Moore. *J. Chem. Phys.*, 97:3235, 1992.

[49] W. H. Green Jr, C. B. Moore, and W. F. Polik. *Annu. Rev. Phys. Chem.*, 43:591, 1992.

[50] D. Townsend, S. A. Lahankar, S. K. Lee, S. D. Chambreau, A. G. Suits, X. Zhang, J. Rheinecker, L. B. Harding, and J. M. Bowman. *Science*, 306:1158, 2004.

[51] X. Zhang, J. L. Rheinecker, and J. M. Bowman. *J. Chem. Phys.*, 122:114313, 2005.

[52] J. L. Rheinecker, X. Zhang, and J. M. Bowman. *Molecular Physics*, 103:1067, 2005.

[53] J. M. Bowman and X. Zhang. *Phys. Chem. Chem. Phys.*, 8:321, 2006.

[54] S. D. Chambreau, S. A. Lahankar, and A. G. Suits. *J. Chem. Phys.*, 125:044302, 2006.

[55] S. A. Lahankar, S. D. Chambreau, D. Townsend, F. Suits, J. Farnum, X. Zhang, J. M. Bowman, and A. G. Suits. *J. Chem. Phys.*, 125:044303, 2006.

[56] S. D. Chambreau, D. Townsend, S. A. Lahankar, S. K. Lee, and A. G. Suits. *Physica Scripta*, 73:c89, 2006.

[57] A. C. Terentis and S. H. Kable. *Chem. Phys. Lett.*, 258:626, 1996.

[58] A. C. Terentis, S. E. Waugh, G. F. Metha, and S. H. Kable. *J. Chem. Phys.*, 108:3187, 1998.

[59] H. M. Yin, K. Nauta, and S. H. Kable. *J. Chem. Phys.*, 122:194312, 2005.

[60] M. J. Dulligan adn M. F. Tuchler, J. Zhang, A. Kolessov, and C. Wittig. *Chem. Phys. Lett.*, 276:84, 1997.

[61] L. R. Valachovic, M. F. Tuchler, M. Dulligan, Th. Droz-Georget, M. Zyrianov, A. Kolessov, H. Reisler, and C. Wittig. *J. Chem. Phys.*, 112:2752, 2000.

[62] G. D. Smith, L. T. Molina, and M. J. Molina. *J. Phys. Chem. A*, 106:1233, 2002.

[63] T. Yonehara and S. Kato. *J. Chem. Phys.*, 117:11131, 2002.

[64] T. Yonehara, T. Yamamoto, and S. Kato. *Chem. Phys. Lett.*, 393:98, 2004.

[65] T. Yonehara and S. Kato. *J. Chem. Phys.*, 125:084307, 2006.

[66] P. Ho and A. V. Smith. *Chem. Phys. Lett.*, 90:407, 1982.

[67] B. A. Waite, S. K. Gray, and W. H. Miller. *J. Chem. Phys.*, 78:259, 1983.

[68] W. F. Polik, C. B. Moore, and W. H. Miller. *J. Chem. Phys.*, 89:3584, 1988.

[69] W. H. Miller, R. Hernandez, C. B. Moore, and W. F. Polik. *J. Chem. Phys.*, 93:5657, 1990.

[70] Y. T. Chang, C. Minichino, and W. H. Miller. *J. Chem. Phys.*, 96:4341, 1992.

[71] W. Chen, W. L. Hase, and H. B. Schlegel. *Chem. Phys. Lett.*, 228:436, 1994.

[72] X. Li, J. M. Millam, and H. B. Schlegel. *J. Chem. Phys.*, 113:10062, 2000.

[73] S. Anand and H. B. Schlegel. *J. Phys. Chem. A*, 106:11623, 2002.

[74] D. Feller, M. Dupuis, and B. C. Garrett. *J. Chem. Phys.*, 113:218, 2000.

[75] J. Troe. *J. Chem. Phys.*, 109:8320, 2005.

[76] J. D. Goddard, Y. Yamaguchi, and H. F. Schaefer III. *J. Chem. Phys.*, 75:3459, 1981.

[77] D. H. Zhang, D. Xie, M. Yang, and S.-Y. Lee. *Phys. Rev. Lett.*, 89:283203, 2002.

[78] D. H. Zhang and J. Z. H. Zhang. *J. Chem. Phys.*, 101:1146, 1994.

[79] D. H. Zhang and J. C. Light. *J. Chem. Phys.*, 104:4544, 1996.

[80] D. H. Zhang and S. Y. Lee. *J. Chem. Phys.*, 110:4435, 1999.

[81] M. Yang, D. H. Zhang, M. A. Collins, and S.-Y. Lee. *J. Chem. Phys.*, 114:4759, 2001.

[82] D. H. Zhang, M. Yang, and S.-Y. Lee. *J. Chem. Phys.*, 117:10067, 2002.

[83] D. H. Zhang and J. Z. H. Zhang. *J. Chem. Phys.*, 103:6512, 1995.

[84] J. C. Light and D. H. Zhang. *Faraday Discuss.*, 110:105, 1998.

[85] J. Troe. *J. Phys. Chem. A*, 111:3862, 2007.

[86] J. Troe. *J. Phys. Chem. A*, 111:3868, 2007.

[87] J. D. Farnum, X. Zhang, and J. M. Bowman. *J. Chem. Phys.*, 126:13405, 2007.

[88] S. A. Lahankar, S. D. Chambreau, X. Zhang, J. M Bowman, and A. G. Suits. *J. Chem. Phys.*, 126:044314, 2007.

[89] R. N. Zare. *Science*, 311:1383, 2006.

[90] F. H-Larranaga and U. Manthe. *J. Chem. Phys.*, 113:5115, 2000.

[91] J. M. Bowman, D. Wang, X. Huang, F. H-Larranaga, and U. Manthe. *J. Chem. Phys.*, 114:9683, 2001.

[92] D. Wang. *J. Chem. Phys.*, 124:201105, 2006.

[93] D. C. Clary. *J. Phys. Chem.*, 98:10678, 1994.

[94] G. Nyman and D. C. Clary. *J. Chem. Phys.*, 101:5756, 1994.

[95] H. G. Yu, G. Nyman, and R. B. Walker. *J. Chem. Phys.*, 109:5896, 1998.

[96] H. G. Yu and G. Nyman. *J. Chem. Phys.*, 110:7233, 1999.

[97] H. G. Yu and G. Nyman. *J. Chem. Phys.*, 111:3508, 1999.

[98] D. H. Zhang and J. Z. H. Zhang. *J. Chem. Phys.*, 112:585, 2000.

[99] M. L. Wang and J. Z. H. Zhang. *J. Chem. Phys.*, 114:7013, 2001.

[100] M. L. Wang, Y. Li, J. Z. H. Zhang, and D. H. Zhang. *J. Chem. Phys.*, 113:1802, 2000.

[101] M. L. Wang and J. Z. H. Zhang. *J. Chem. Phys.*, 117:3081, 2002.

[102] Q. Cui, M. L. Wang, and J. Z. H. Zhang. *Chem. Phys. Lett.*, 410:115, 2005.

[103] M. H. Beck, A. Jackle, G. A. Worth, and H.-D. Meyer. *Phys. Rep.*, 324:1, 2000.

[104] D. H. Zhang, W. Bao, and S. Y. Lee. *J. Chem. Phys.*, 122:091101, 2005.

[105] L. L. Zhang, S. Y. Lee, and D. H. Zhang. *J. Phys. Chem. A*, 110:5513, 2006.

[106] M. J. Kurlyo, G. A. Hollinden, and R. B. Timmons. *J. Chem. Phys.*, 52:1773, 1970.

[107] D. L. Bauch, C. J. Cobos, R. A. Cox, E. P. Frank, T. Just, J. A. Kerr, M. J. Pilling, J. Troe, R. W. Walker, and J. Warnatz. *J. Phys. Chem. Ref. Data*, 21:411, 1992.

[108] T. Takayanagi. *J. Chem. Phys.*, 104:2237, 1996.

[109] D. Y. Wang and J. M. Bowman. *J. Chem. Phys.*, 115:2055, 2001.

[110] D. H. Zhang M. Yang and S.-Y. Lee. *J. Chem. Phys.*, 117:9539, 2002.

[111] F. H-Larranaga and U. Manthe. *J. Phys. Chem.*, 105:2522, 2001.

[112] T. Wu, H.-J. Werner, and U. Manthe. *J. Chem. Phys.*, 124:164307, 2006.

[113] J. M. Bowman. *J. Phys. Chem.*, 95:4960, 1991.

[114] M. J. T. Jordan and R. G. Gilbert. *J. Chem. Phys.*, 102:5669, 1995.

[115] A. J. C. Varandas, J. Z. H. Zhang, Q. Cui, and K. L. Han. *J. Chem. Phys.*, 125:064312, 2006.

[116] D. H. Zhang M. Yang and S.-Y. Lee. *J. Chem. Phys.*, 126:064303, 2007.

[117] J. C. Light, I. P. Hamilton, and J. V. Lill. *J. Chem. Phys.*, 82:1400, 1985.

[118] R. Kosloff. *J. Phys. Chem.*, 92:2087, 1988.

[119] D. H. Zhang, M. Yang, and S.-Y. Lee. *Phys. Rev. Lett.*, 89:103201, 2002.

[120] S. C. Althrope and D. C. Clary. *Annu. Rev. Phys. Chem.*, 54:493, 2003.

[121] E. J. Heller. *J. Chem. Phys.*, 64:63, 1975.

[122] R. Harris. *J. Chem. Phys.*, 72:1776, 1980.

[123] R. B. Gerber, V. Buch, and M. A. Ratner. *J. Chem. Phys.*, 77:3022, 1982.

[124] R. B. Gerber and M. A. Ratner. *Adv. Chem. Phys.*, 70:97, 1988.

[125] M. Messina and R. D. Coalson. *J. Phys. Chem.*, 90:4015, 1989.

[126] P. Jungwirth and R. B. Gerber. *Chem. Rev.*, 99:1583, 1999.

[127] R. Kosloff, A. D. Hammerich, and M. A. Ratner. *Large finite systems, Proceedings of the Twentieth Jerusalem Symposium of Quantum Chemistry and Biochemistry,* edited by J. Jortner. Reidel, Dordrecht, 1987.

[128] N. Makri and W. H. Miller. *J. Chem. Phys.*, 87:5781, 1987.

[129] Z. Kotler, A. Nitzan, and R. Kosloff. *Chem. Phys. Lett.*, 153:483, 1988.

[130] A. D. Hammerich, R. Kosloff, and M. A. Ratner. *Chem. Phys. Lett.*, 171:97, 1990.

[131] L. Wang and A. B. McCoy. *J. Chem. Phys.*, 113:10605, 2000.

[132] R. Zwanzig. *J. Stat. Phys.*, 9:215, 1973.

[133] A. O. Caldeira and A. J. Leggett. *Ann. Phys. (N.Y.)*, 149:374, 1983.

[134] L. J. Lauhon and W. Ho. *Phys. Rev. Lett.*, 85:4566, 2000.

[135] W. H. Miller. *J. Chem. Phys.*, 61:1823, 1974.

[136] J. G. Lauderdale and D. G. Truhlar. *J. Chem. Phys.*, 84:1843, 1986.

[137] T. N. Truong and D. G. Truhlar. *J. Chem. Phys.*, 88:6611, 1988.

[138] S. E. Wonchoba and D. G. Truhlar. *J. Chem. Phys.*, 99:9637, 1993.

[139] K. Haug, G. Wahnström, and H. Metiu. *J. Chem. Phys.*, 92:2083, 1990.

[140] S. E. Wonchoba, W-P. Hu, and D. G. Truhlar. *Theoretical and Computational Approaches to Interfaces Phenomena;* H. L. Sellers, J. T. Golab, Eds. Plenum, New York, 1994.

[141] I. Nikitin, W. Dong, H. F. Busnengo, and A. Salin. *Surf. Sci.*, 547:149, 2003.

[142] S. E. Wonchoba, W-P. Hu, and D. G. Truhlar. 51:51, 1995.

[143] J. Frenkel. *Wave Mechanics*. Clarendon Press, Oxford, 1934.

[144] H. Wang, M. Thoss, and W. H. Miller. *J. Chem. Phys.*, 112:47, 2000.

[145] T. Yamamoto, H. Wang, and W. H. Miller. *J. Chem. Phys.*, 116:7335, 2002.

[146] U. Manthe, T. Seideman, and W. H. Miller. *J. Chem. Phys.*, 101:4759, 1994.

[147] H. Wang, X. Song, D. Chandler, and W. H. Miller. *J. Chem. Phys.*, 110:4828, 1999.

TRANSITION STATE WAVE PACKET STUDY OF QUANTUM MOLECULAR DYNAMICS IN COMPLEX SYSTEMS

ZHANG LILING

NATIONAL UNIVERSITY OF SINGAPORE

2007